Erasmus Mundus Joint Master Degree in NUCLEAR PHYSICS

NucPhys 2021-2023

Angular distribution studies for the $^{16}O(p,\gamma)^{17}F$ reaction at the LUNA400 accelerator

SABIHA TASNEEM

Dipartimento di Fisica e Astronomia

Università di Padova

Italy

Supervisor: Prof. Antonio Caciolli

Co-Supervisor: Dr. Denise Piatti

Submission Date: December 2023

Abstract

The $^{16}O(p,\gamma)^{17}F$ reaction plays a crucial role during the hot bottom burning in asymptotic giant branch stars. This reaction determines, indeed, the $^{16}O/^{17}O$ ratio which is observable and a useful tool to trace mixing processes and galactic chemical evolution.

Despite its importance the $^{16}O(p,\gamma)^{17}F$ reaction cross section is poorly constrained at energies of interest and present stellar models have to rely on extrapolation. Moreover a missing piece of information is the angular distribution, crucial parameter to get cross section from experimental quantities.

A study of the $^{16}O(p,\gamma)^{17}F$ reaction cross section and angular distribution of emitted γ-ray during the reaction has been carried out at LUNA400 facility, down to low energies. The measurement was done by bombarding solid Ta_2O_5 target with proton beam of 370 keV and 398 kev energy in laboratory frame. The emitted γ-ray due to the direct radiative capture of protons by ^{16}O has been measured using two $CeBr_3$ scintillators and one HPGe detector placed at different angle with respect to the beam direction.

In the present work the data acquisition and analysis for the angular distribution investigation is presented.

Contents

Introduction

The night sky, filled with stars and ancient myths, has always captivated our imagination and led us to explore the vast universe beyond Earth. Astronomy and astrophysics are driven by human need to explore and understand the universe. Astronomy began with the early observation of stars and celestial object together with the first model of the universe. At the beginning the geocentric view of the early Greeks, where the sun, moon, and planets revolved around the earth within a rotating sphere of fixed stars was the accepted model. The heliocentric view, dating back to Copernicus, put the planetary system on a more nearly correct basis and brought to rest the sphere of the stars. The idea that stars are other suns has evolved over the centuries, with the Milky Way now standing out as a majestically rotating spiral structure in the foreground of the vast celestial scene. The discoveries of the past twenty years have radically changed our concepts of the origin and evolution of stars, galaxies, and the universe itself. On the other hand, Astrophysics, the union of astronomy and physics, applies physical laws to the laboratory of space. The law of gravitation by Newton inaugurated a dynamical interpretation of the motion in the solar system, representing a key to the understanding of many features of the entire universe. In macro-scale, astrophysics seeks to understand the vast space in the cosmos, while in micro-scale, it studies atoms, nuclei, and elementary particles, the building blocks of matter. Investigations during the last fifty years have shown that we are connected to distant space and time not only by our imagination but also through a common cosmic heritage: the chemical elements that make up our bodies. These elements were created in the hot interiors of remote and long-vanished stars over many billions of years. As a result, each living creature on Earth embodies atoms from distant corners of our Galaxy and from a past thousands of times more remote than the beginning of human evolution.

To achieve this goal Astrophysics first started from the long standing puzzle of the energy fueling stars. Only in 1920 sir Eddington proposed, indeed, for the first time the concept of stars generating most of their energy through thermonuclear reactions [RR88]. Since then more and more observational data were collected. The first evidence of stellar nucleosynthesis was observed: the discovery of lines from the unstable technetium isotope in stellar spectra in 1952 [Mer52]. Finally the Gamow's work on quantum tunnelling effect, probing that charged particle induced reactions are possible also in stellar core condition was crucial. In 1957, Burbidge, Burbidge, Fowler, Hoyle, and Cameron integrated all new ideas and information on element formation into a coherent picture, referred to as the theory of nucleosynthesis of the elements and their isotopes [BBFH57]. The present picture is that all elements from carbon to uranium were produced entirely within stars.

Laboratory nuclear astrophysics aims to investigate stellar nucleosynthesis pro-

cesses and particularly to determine their cross section. This is often frustrating given the small cross section. Over its 30 year long story LUNA (Laboratory for Underground Nuclear Astrophysics) achieved incredible results thanks to the high performance of the setup and the ultra low background locations [ABDG22].

The reaction cross section knowledge allows the calculation of the reaction rate to be included in stellar model, whose predictions can be compared with observational data to get deep insights on evolution of stars, the generation of energy in stars, the synthesis of elements in stars up to the chemical evolution of galaxies and the whole Universe.

The present thesis describes the study of one of the processes occurring in stars and it is divided into six chapters. The first three chapters provide an overview of the present knowledge of the $^{16}O(p,\gamma)^{17}F$ reaction along with the necessary theoretical framework. The experimental equipment and techniques used in the laboratory are then introduced. Chapter 5 describe the analysis process aiming to derive the $^{16}O(p,\gamma)^{17}F$ angular distribution. And then the last chapter summarises the work done here.

1 Stellar Evolution

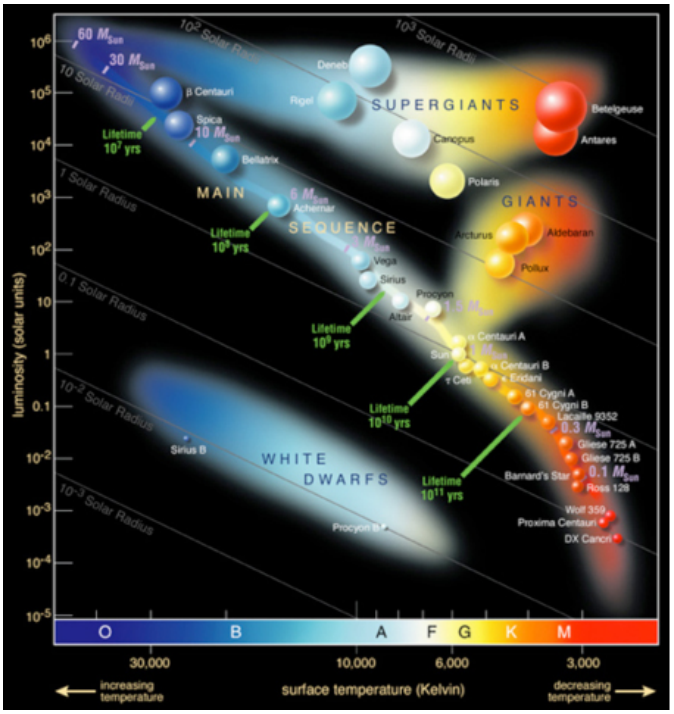

Figure 1.1. The Hertzsprung-Russell diagram [Obs17]

The evolutionary sequences for stars are commonly described by their position on a graph called the Hertzsprung-Russell (H-R) diagram, see Figure 1.1. The Hertzsprung-Russell diagram, or H-R diagram, shows the luminosity (absolute magnitude or brightness) of stars plotted against their temperature (stellar classification). Since both luminosity and temperature depend on the mass and chemical composition of a star; the luminosity, spectral type, color, temperature, mass, chemical composition, age, and evolutionary history can be inferred from the location of a star on the graph – so the H-R diagram is considered as the visual plot of stellar evolution.

The energy emitted by stars is attributed to nuclear reactions, which are initiated by the energy generated by the gravitational contraction that occurs during stellar evolution. The birth of a star takes place with a gas mass contracting and achieving the density and temperature conditions to ignite H, main sequence phase.

The major determinant of a star evolution is its mass upon reaching the main sequence, as presented in Fig. 1.2. The evolution of a low-mass star and a high-mass star, as following from the exhaustion of the H fuel is briefly summarised

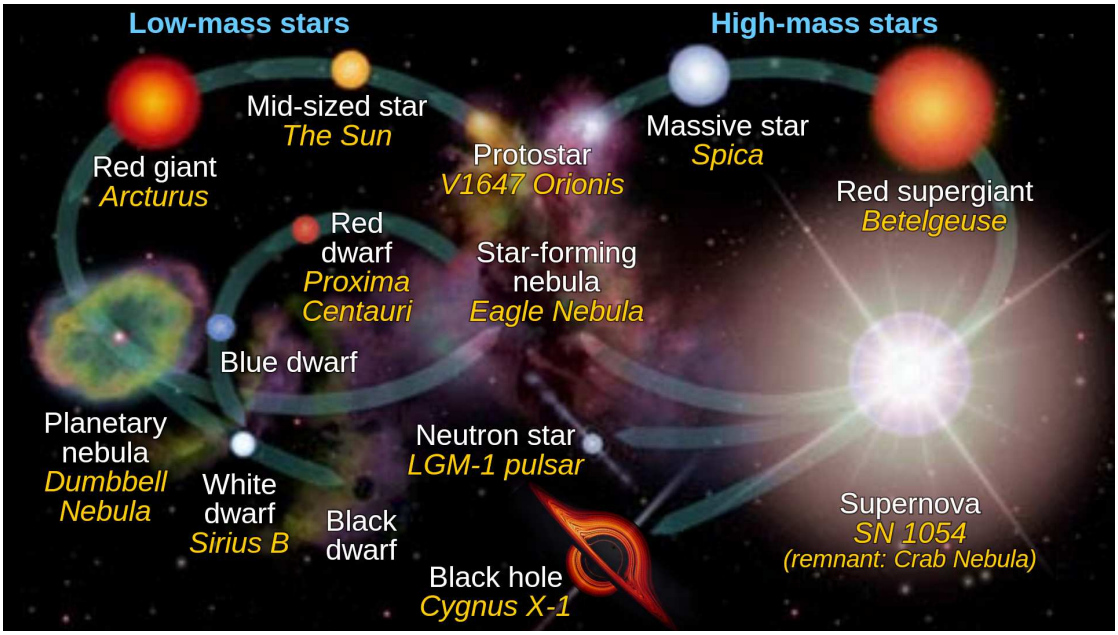

Figure 1.2. Stellar evolution of low-mass (left cycle) and high-mass (right cycle) stars, with examples in italics. [Cen14]

here [COS]. After the complete conversion of hydrogen in the core into helium, the process of energy generation, indeed, ceases and the core initiates contraction while the H leftover moves to the external layer, this is the so called hydrogen-burning shell. Simultaneously, the helium core undergoes contraction and experiences a rise in temperature. As a result, the star external layers undergoes a significant expansion and experiences a substantial increase in brightness, transforming into a red giant. Ultimately, the core attains temperatures of sufficient magnitude to undergo helium fusion, resulting in the production of carbon and oxygen. If the stellar mass is below around 2.2 solar masses, the core undergoes a quick ignition event known as a helium core flash. If the star has a greater mass, the ignition of the core occurs in a stable way. The star undergoes a significantly shorter duration of helium burning in its core compared to the duration of hydrogen burning. After the complete conversion of helium, the carbon core starts to contract and experience a rise in temperature while the combustion of helium moves to a shell located just above the core.

The subsequent events are contingent upon the stellar mass.

Low-mass stars with $M < 8M_{\odot}$ The carbon core remains inert and undergoes contraction, although it never attains the temperatures necessary to ignite. Nevertheless, the presence of two burning shells results in a thermally unstable state

where hydrogen and helium combustion take place in an alternating manner, this is the so called Asymptotic Giant Branch phase, which is also characterized by pretty intense mass depletion. The carbon core undergoes further contraction up to electron degeneracy. The contraction process has reached its limit as the core is now sustained by electron pressure rather than gas pressure, resulting in the formation of a white dwarf. Concurrently the star outer layers are injected into the interstellar medium resulting in the creation of a planetary nebula.

High-mass stars with $M > 8M_{\odot}$ The contracting core will attain the temperature necessary for carbon ignition and initiate the fusion process, transitioning into neon burning. The process of core burning, followed by core contraction and shell burning, is iterated through a sequence of nuclear events that generate progressively more massive elements until iron is synthesised in the core. The process of burning iron does not result in the formation of heavier elements since it is an endothermic reaction that requires an input of energy rather than releasing energy. Consequently, the star has ultimately depleted its fuel and succumbs to gravitational collapse. The subsequent events are determined by the mass of the stellar core. If the mass of the core is below approximately three solar masses, the collapse of the core can be stopped by the neutron pressure, which is a more extreme condition than the electron pressure that sustains white dwarfs. Under these circumstances, the core transforms into a neutron star. The abrupt stopping of the core's contraction generates a shock wave that spreads outward through the star's outer layers, causing it to disintegrate in a core-collapse supernova detonation. If the core exceeds a mass of around 3 solar masses, even the force exerted by neutrons is unable to counteract gravity, resulting in further collapse into a stellar black hole. The expelled gas expands into the interstellar medium, enriching it with all the elements produced throughout the star's lifespan and in the detonation itself. Supernova remnants serve as the primary hubs for the spread of chemicals across the Universe.

1.1 Stellar Nucleosynthesis

Stellar nucleosynthesis is the process by which the elements have been formed and are still being synthesized in the interiors of evolving stars. As described above the ash produced by one series of nuclear events serves as the energy source for the subsequent series. For example helium, which is the product of hydrogen combustion, eventually ignites producing carbon and oxygen which will ignite in subsequent evolutionary phases.

According to the theory of stellar nucleosynthesis, a wide range of mechanisms have enabled the elements to evolve and continue to do so. The schematic

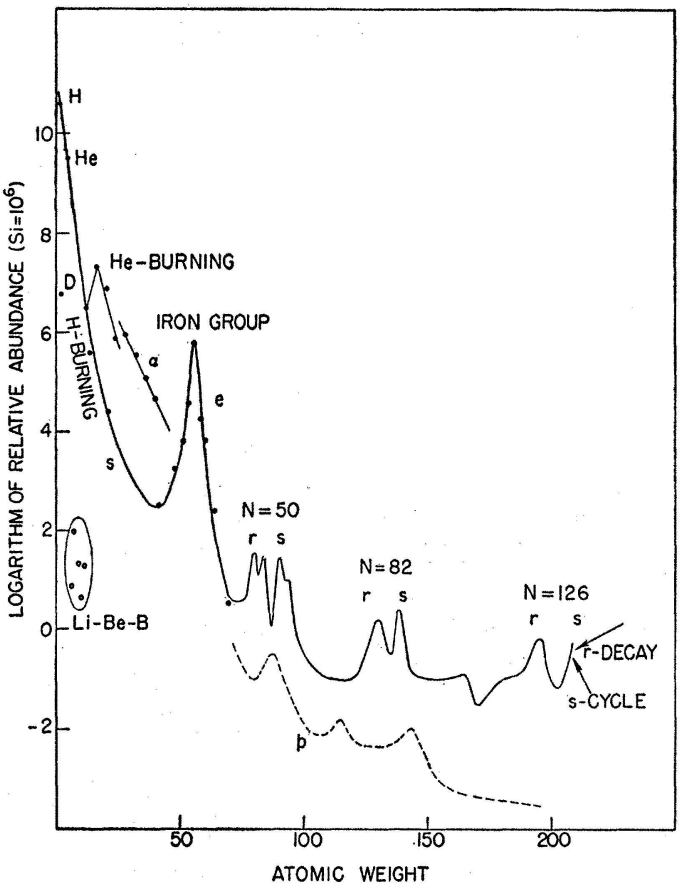

Figure 1.3. Schematic curve of atomic abundances as a function of atomic weight based on the data of Suess and Urey. [SU56]

abundance curve, shown in Figure 1.3, indicates the presence of many processes, including H burning and following core and shell burning phases as well as s, r and p-processes. The s- and r- processes, different from the thermonuclear reactions described so far, involves neutron capture and enable the production of isotopes heavier than iron [BBFH57]. On the other hand the so called p-nuclei are produced mainly via photodisintegration [BBFH57].

Behind each observed abundance many reactions are at play as well as many complex stellar processes. The key for a proper understanding is the interplay between nuclear physics inputs for the thermonuclear reactions, as the cross section, the stellar models and their predictions and the many different observations available. Nuclear astrophysics aims to precisely determine the reaction cross section. In the next section a minimal framework is provided to introduce the theoretical

tool to achieve this goal.

2 Theoretical Framework

The stellar nucleosynthesis is the process that creates new atomic nuclei. The protons and neutrons were formed after the Big Bang, these make H and He. These nuclei are combined during the stellar evolutionary process to form more complex atoms via nuclear reactions that transform one element into another. The key parameter of these processes is the cross section and in the following an overview on the formalism and tools to treat nuclear reactions and cross section is given.

2.1 Nuclear Reaction

The most basic form of nuclear reaction can be represented symbolically as

$$x + A \rightarrow y + B$$

which in nuclear physics is mostly expressed as A(x, y)B. The symbol x represents the projectile, while A represents the target nucleus. These two components form the entrance channel. On the other hand, y represents the ejectile, and B represents the residual nucleus. Together, they make the exit channel.

A fundamental quantity dealing with thermonuclear reactions is the energy produced, the so called Q-value of a nuclear reaction, which is determined by the mass difference between the initial species and the final atoms. If the nuclei in the entrance channel have nuclear masses M_x and M_A, while the nuclei in the exit channel have nuclear masses M_y and M_B, the law of energy conservation defines the Q-value of the nuclear reaction.

$$Q_{value} = (M_x + M_A - M_y - M_B)c^2 \tag{2.1}$$

If the Q-value is positive, it indicates that there is an excess of energy being produced in the process, therefore classifying the reaction as exothermic. On the other hand, if the Q-value is negative, the process requires a minimum energy equal to Q in order to proceed, and the reaction is categorised as endothermic.

The cross section for reaction is defined as:

$$\sigma = \frac{\mathrm{N}}{(\mathrm{N}_t)(\mathrm{N}_b)} \tag{2.2}$$

where N is the number of reactions, N_t is the number of target nuclei and N_b is the number of the incident particles. The unit of nuclear cross section is barn (b) [1 b = 10^{-24} cm^2]. The cross section is a key quantity to derive the stellar reaction rate, the main ingredient entering in stellar model and thus in isotopic abundance calculation. Let us consider a stellar gas containing N_x particles of type X and N_y

particles of type Y per cubic centimetre, with relative velocities v. Nuclear cross sections typically vary with energy or, equivalently, with velocity. Therefore, the cross section σ is a function of the relative velocity v between the projectile and the target nucleus. The rate of nuclear reactions, denoted by r, can be calculated by multiplying the numbers N_x, N_y, v, and $\sigma(v)$:

$$r = N_x N_y v\sigma(v) \tag{2.3}$$

Similar to other gases, the velocity of the particles in a stellar gas changes over a large range of values, as indicated by the probability function $\phi(v)$, where

$$\int_0^\infty \phi(v)dv = 1 \tag{2.4}$$

In order to obtain the average value $\langle\sigma v\rangle$, the product $v\sigma(v)$ in equation 2.3 needs to be convoluted with the velocity distribution $\phi(v)$. Here, $\phi(v)dv$ represents the probability that the relative velocity v between the participants of a nuclear reaction falls within the range of v and $v + dv$.

$$\langle\sigma v\rangle = \int_0^\infty \phi(v)v\sigma(v)dv \tag{2.5}$$

The quantity $\langle\sigma v\rangle$ is commonly known as the reaction rate per particle pair. For exothermic processes (where $Q > 0$), the integral is calculated from $v = 0$ to $v = \infty$. On the other hand, for endothermic reactions (where $Q < 0$), the integral begins at the threshold velocity $v_T \propto Q^{1/2}$. The overall reaction rate, r, then can be calculated as:

$$r = N_x N_y \langle\sigma v\rangle \tag{2.6}$$

The product $N_x N_y$ represents the total count of distinct pairings of nuclei X and Y. This product, and consequently the overall reaction rate for nonidentical particles, reaches its highest value when $N_x = N_y$. In the case of identical particles, the number product must be halved to avoid double counting of each pair. The problem is addressed by incorporating the Kronecker symbol δ_{xy} into formula 2.6, resulting in the expression

$$r = N_x N_y \langle\sigma v\rangle (1 + \delta_{xy})^{-1} \tag{2.7}$$

The experimentalist and theorist have been trying to determine the quantity $\langle\sigma v\rangle$ at the appropriate star velocities. Direct measurements at these velocities are sometimes impractical, demanding the use of theoretical extrapolations.

Indeed, the stellar gas nuclei velocities can be described by a Maxwell-Boltzmann velocity distribution,

$$\phi(v) = 4\pi v^2 \left(\frac{m}{2\pi kT}\right)^{3/2} \exp\left(-\frac{mv^2}{2kT}\right) \tag{2.8}$$

where T refers to the temperature of the gas and m to the mass of the nucleus. The numerator in the exponential term can be expressed in terms of the kinetic energy of the nucleus, $E = \frac{1}{2}mv^2$. Then the function $\phi(v)$ can be rewritten in terms of this energy as

$$\phi(E) \propto E \exp(-E/kT) \tag{2.9}$$

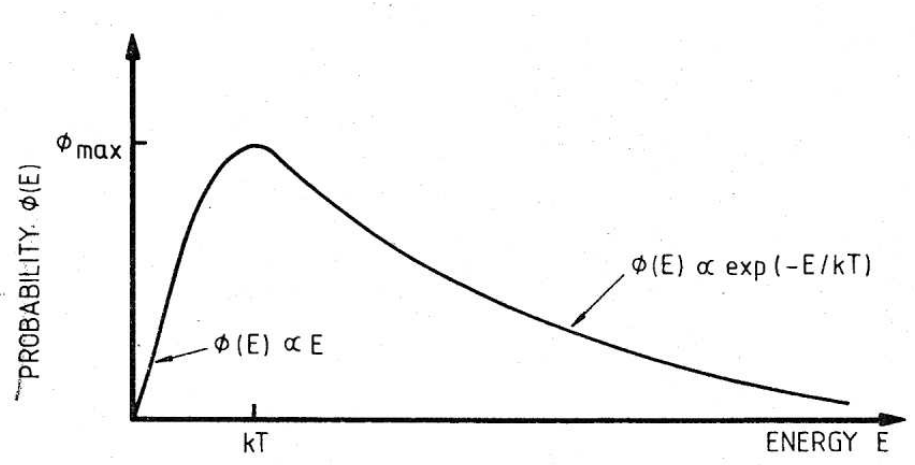

Figure 2.1. the Maxwell-Boltzmann energy distribution of a gas characterized by the temperature T. [RR88]

Equation 2.9 shows that, at low energies, $E \ll kT$, $\phi(E)$ increases linearly with E and reaches a maximum value at $E = kT$. On contrary, at higher energies, $E \gg kT$, the function $\phi(E)$ decreases exponentially, and asymptotically approaches zero at very high energies (Fig. 2.1).
For example, at the solar interior ($T_6 = 15$) $kT = 1.3$keV and in supernova events ($T_6 = 5000$) $kT = 431$keV.

The rate $\langle \sigma v \rangle$ given in Eq. 2.5 can be written in terms of the Maxwell-Boltzmann velocity distribution as

$$\langle \sigma v \rangle = 4\pi \left(\frac{\mu}{2\pi kT}\right)^{3/2} \int_0^\infty v^3 \sigma(v) \exp\left(-\frac{\mu v^2}{2kT}\right) dv \tag{2.10}$$

Replacing with the center-of-mass energy $E = \frac{1}{2}\mu v^2$, the reaction rate per particle pair can be expressed in the form

$$\langle \sigma v \rangle = \left(\frac{8}{\pi\mu}\right)^{1/2} \frac{1}{(kT)^{3/2}} \int_0^\infty \sigma(E) E \exp\left(-\frac{E}{kT}\right) dE \tag{2.11}$$

Eq. 2.11 characterizes the reaction rate at a given stellar temperature T. For charged-particle-induced reactions the nuclei repel each other due their positive charge. The Coulomb barrier hinders nuclear reaction to take place. Classically, in stellar temperature, the energy is insufficient to overcome the Coulomb barrier. Nevertheless, in the view of Quantum Mechanics, there is a little but finite probability for the particles with energy below the Coulomb barrier to penetrate the barrier [Gam28] [CG29]. This phenomenon of barrier penetration is called tunnel effect.

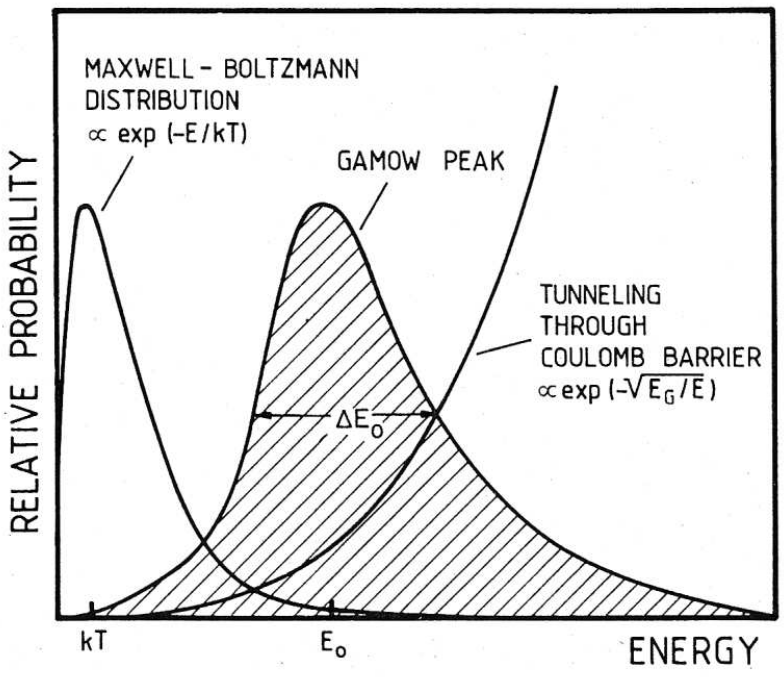

Figure 2.2. Gamow Peak [RR88]

The tunneling probability approaches unity at energies near the Coulomb barrier, but right below the barrier the probability drops exponentially. This can be expressed mathematically as (for an incoming s-wave):

$$P = \exp(-2\pi\eta) \tag{2.12}$$

where the quantity η is called the Sommerfeld parameter and is equal to

$$\eta = \frac{Z_1 Z_2 e^2}{\hbar v} \tag{2.13}$$

and the exponent can be expressed numerically as:

$$2\pi\eta = 31.29 Z_1 Z_2 \left(\frac{\mu}{E}\right)^{1/2}$$

where the center-of-mass energy E is given in units of keV and μ is in amu. This approximate expression for the tunneling probability is called the Gamow factor. This exponential behavior of the probability for tunneling shows that the cross section for charged-particle-induced nuclear reactions drops rapidly for energies below the Coulomb barrier:

$$\sigma(E) \propto \exp(-2\pi\eta)$$

However, the cross section is also inversely proportional to the energy:

$$\sigma(E) \propto \pi\hbar^2 \propto \frac{1}{E}.$$

Combining both relations, the cross section can be expressed as

$$\sigma(E) = \frac{1}{E}\exp(-2\pi\eta)S(E) \tag{2.14}$$

where the function $S(E)$ is referred to as the astrophysical S-factor. If equation 2.14 is inserted in equation 2.11 for reaction rate per particle pair $\langle\sigma v\rangle$, we obtain

$$\langle\sigma v\rangle = \left(\frac{8}{\pi\mu}\right)^{1/2} \frac{1}{(kT)^{3/2}} \int_0^\infty S(E) \exp\left[-\frac{E}{kT} - \frac{b}{E^{1/2}}\right] dE \tag{2.15}$$

where the quantity b is given by

$$b = (2\mu)^{1/2}\pi e^2 Z_1 Z_2/\hbar = 0.989 Z_1 Z_2 \mu^{1/2}(\text{MeV})^{1/2}.$$

As also shown in Fig. 2.2, combining the Maxwell-Boltzman distribution and the penetrability of the Coulomb barrier a peak is formed. This peak is called Gamow peak and it represents the window of energies where nuclear reaction occurs in the stellar environment at a given temperature. By maximizing the argument of the exponential term in equation 2.15 it is possible to determine the maximum of this peak as:

$$E_o = 1.22(Z_1^2 Z_2^2 \mu T^2)^{1/3}(\text{keV}).$$

where $T = T_6$, temperature in 10^6 Kelvin unit.

Since in charged- particle-induced reactions the cross section drops exponentially at low energies due to the effect of the Coulomb barrier, it is more difficult to measure the relevant cross sections σ. Even with improved experimental techniques, it is difficult to achieve the relevant stellar energy regions for quiescent stellar burning. Hence direct measurements of $\sigma(E)$ for charged-particle-induced reactions is not achieved in many different stellar scenarios. The observed $\sigma(E)$ is hence extrapolated into the stellar energy region. Experimental data are required at very low energies in order to improve the extrapolation.

2.2 Direct Capture

The direct capture mechanism represents a single-step process where the incident projectile enters a shell-model orbit of the target nucleus by emitting a photon. This is a nonresonant process because it does not require the creation of a compound state. They are therefore referred to as direct capture (single-step) reactions.

Fig. 2.3 illustrates the A(x,γ)B reaction, where the entrance channel A+x goes directly to the states in the final compound nucleus B, emitting γ radiation. This process can occur at all projectile energies E. Here a projectile x (usually a proton or an α-particle) with energy E is incident on target nuclei A. It leads to γ-ray emission and a residual nucleus B, whose mass is the combination of A and x. The reaction is called a direct process because it goes through a direct transition from the initial state to the final state. Since proton capture is an electromagnetic process, the reaction is usually studied by detecting the emitted γ-rays.

An illustration of the transition scheme of ^{16}O(p,γ)^{17}F reaction, where the direct-capture process from a plane wave ($^{16}O + p$) to final $2s$ and $1d$ orbits (^{17}F) occurs, is shown in Fig. 2.4 [Rol73]. Here only the lowest multipoles E1, M1 and E2 of the transition have been considered.

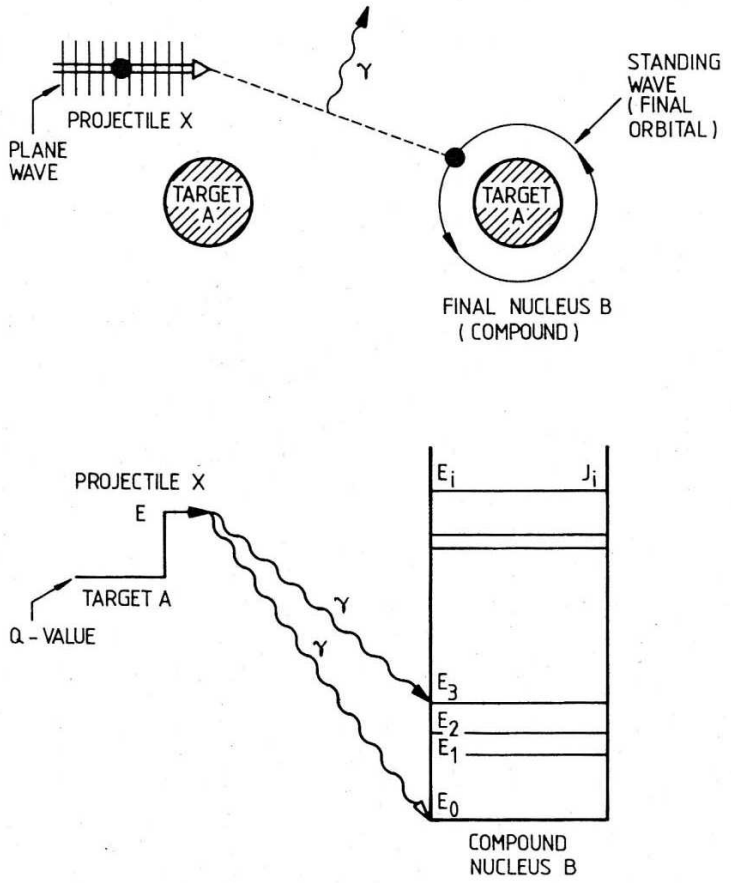

Figure 2.3. Illustration of a Direct Capture Reaction A(x,γ)B with emitted photon energy $E_\gamma = E + Q_value - E_i$ [RR88]

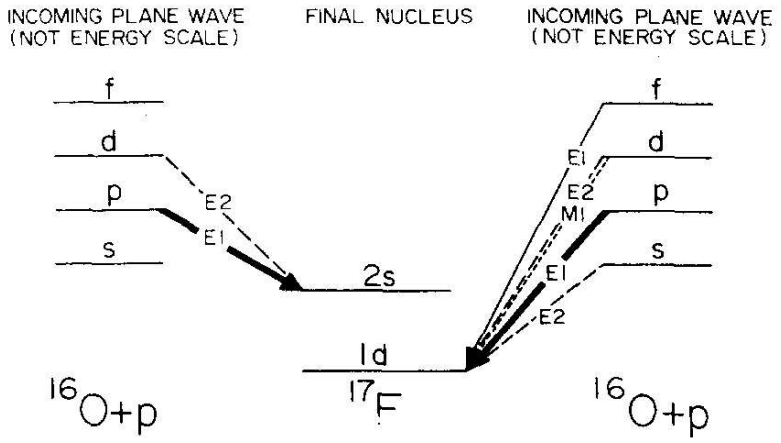

Figure 2.4. Schematic transition scheme for the direct-capture process from a plane wave ($^{16}O + p$) to final $2s$ and $1d$ orbits (^{17}F), considering only the lowest multipoles E1, M1 and E2. [Rol73]

2.3 Angular Distribution

2.3.1 ANGULAR DISTRIBUTIONS FOR DIRECT CAPTURE TRANSITIONS

The theoretical considerations for the angular distribution for direct capture transitions are presented in this section [Rol73]. For a γ-ray (unpolarized) transition of multipole (L, M) between a state $|J_1 M_1\rangle$ and a state $|J_2 M_2\rangle$, the angular distribution is given by [Fer65] [RB67])

$$W(\vartheta_1) = \sum_{M_1 M_2 P} \left| \sum_M \langle J_2 M_2 | T_{LM} | J_1 M_1 \rangle D^{(L)*}_{MP}(\vartheta_1, \varphi_1, 0) \right|^2$$
$$= \sum_{M_1 M_2 P} \left| \sum_M Q_{M_1 M M_2 P} \right|^2$$

where T_{LM} is the interaction multipole operator, and P is the circular polarization of the γ radiation ($P = \pm 1$). For electric transitions, the interaction multipole operator, T_{LM}, is proportional to the spherical harmonics $(-i)^L Y_L^M(\vartheta, \varphi)^*$, $D^{(L)}_{MP}(\vartheta_1, \varphi_1, 0)$, which are elements of the rotation matrices. The summation over the transition matrix elements is incoherent and one index can be dropped since $M = M_1 - M_2$:

$$W(\vartheta_1) = \sum_{M_1 M_2 P} |Q_{M_1 M_2 P}|^2$$

Unique orbital angular momenta. Let us consider that both the initial and final states have single-valued orbital angular momenta. The angular part of the wave functions of these states are given by

$$|J_1 M_1\rangle \propto \sum_{S_1} \mathfrak{l}_1 \mathscr{Y}^O_{l_1}(\vartheta, \varphi) \chi^{M_1}_{S_1},$$
$$|J_2 M_2\rangle \propto \sum_{S_2 \beta} a_{S_2} (l_2 M_2 - \beta S_2 \beta \mid J_2 M_2) \mathscr{Y}^{M_2 - \beta}_{l_2}(\vartheta, \varphi) \chi^{\beta}_{S_2},$$

Using above two expressions, the transition matrix element becomes

$$Q_{M_1 M_2 P} \propto \sum_{S_1 S_2 \beta} a^*_{S_2} \hat{l}_1 (l_2 M_2 - \beta S_2 \beta \mid J_2 M_2) \left\langle \chi^{\beta}_{S_2} \mid \chi^{M_1}_{S_1} \right\rangle$$
$$\times \int \mathscr{Y}^{M_2 - \beta}_{l_2}(\vartheta, \varphi)^* \mathscr{Y}^M_L(\vartheta, \varphi)^* \mathscr{Y}^0_{l_1}(\vartheta, \varphi) \mathrm{d}\Omega D^{(L)*}_{MP}(\vartheta_1, \varphi_1, 0)$$

To reduce the result, the following relations can be used:

$$\left\langle \chi_{S_2}^{\beta} \mid \chi_{S_1}^{M_1} \right\rangle = \delta_{S_2 S_1} \delta_{\beta M_1}; (S_1 = S_2 = S)$$

$$\int \mathscr{Y}_{l_2}^{M_2-\beta *}(\vartheta,\varphi) \mathscr{Y}_{L}^{M *}(\vartheta,\varphi) \mathscr{Y}_{l_1}^{0}(\vartheta,\varphi) \mathrm{d}\Omega = \frac{1}{\sqrt{4\pi}} \hat{L} l_1 \hat{l}_2^{-1} \left(l_1 0 L 0 \mid l_2 0\right) \left(l_1 0 L M \mid l_2 M\right)$$

Then the transition matrix element becomes

$$Q_{M_1 M_2 P} \propto \sum_S a_S^* \hat{L} \hat{l}_1^2 \hat{l}_2^{-1} \left(l_2 M_2 - M_1 S M_1 \mid J_2 M_2\right) \left(l_1 0 L 0 \mid l_2 0\right) \times \left(l_1 0 L M \mid l_2 M\right) D_{MP}^{(L)*} \left(\vartheta_1, \varphi_1, 0\right)$$

With the help of the reduction formula for a product of rotation matrices [RB67], the square of this expression can be evaluated:

$$D_{MP}^{(L)*} D_{MP}^{(L)} = (-)^{M+1} \sum_k (LPL - P \mid k0)(LML - M \mid k0) P_k \left(\vartheta_1\right)$$

An incoherent summing over the channel spin S [Fer65] [RB67] is applied afterwards. Now the angular distribution becomes

$$W\left(\vartheta_1\right) \propto \sum_{SkM_1M_2} \left|a_S\right|^2 \hat{L}^2 \hat{l}_1^4 \hat{l}_2^{-2} \left(l_2 M_2 - M_1 S M_1 \mid J_2 M_2\right)^2 (-)^{M+1} \times \left(l_1 0 L 0 \mid l_2 0\right)^2 \left(l_1 0 L M \mid l_2 M\right)^2 (L1L - 1 \mid k0)(LML - M \mid k0) P_k \left(\vartheta_1\right).$$

The orthogonality relations for CG coefficients and the formula for products of CG coefficients in terms of Racah coefficients are applied and thus the angular distribution becomes:

$$W\left(\vartheta_1\right) \propto \sum_k (-)^{1+k+l_2} l_1^4 \hat{L}^2 \hat{l}_2^{-2} J_2^2 \left(l_1 0 L 0 \mid l_2 0\right)^2 \left(l_1 0 l_1 0 \mid k0\right) \times (L1L - 1 \mid k0) W\left(L l_1 L l_1; l_2 k\right) P_k \left(\vartheta_1\right)$$

Using the following definition [Fer65]

$$\bar{Z}_1\left(l_1 L l_1 L; l_2 k\right) = (-)^{k+1} \hat{L}^2 \hat{l}_1^2 (L1L - 1 \mid k0) W\left(L l_1 L l_1; l_2 k\right)$$

the following Angular Distribution formula is obtained :

$$W\left(\vartheta_1\right) = \sum_k \left(l_1 0 l_1 0 \mid k0\right) \bar{Z}_1\left(l_1 L l_1 L; l_2 k\right) P_k\left(\vartheta_1\right)$$

Mixed orbital angular momenta. For the final state containing contributions from more than one angular momentum l_2, its wave function including the radial dependence is given by

$$|J_2 M_2\rangle = \sum_{l_2 S_2 \beta} a_{S_2} \frac{u_{l_2}(k_2 r)}{r} (l_2 M_2 - \beta S_2 \beta \mid J_2 M_2) \mathscr{Y}_{l_2}^{M_2-\beta}(\vartheta, \varphi) \chi_{S_2}^{\beta}$$

As derived for the single-valued orbital momenta in the previous paragraph, the transition matrix element is given here by

$$Q_{M_1 M_2 P} \propto \sum_{S l_2} a_S^* (l_2 M_2 - M_1 S M_1 \mid J_2 M_2) (l_1 0 L 0 \mid l_2 0) (l_1 0 L M \mid l_2 M) R_{l_1 L l_2} D_{MP}^{(L)*}$$

where $R_{l_1 L l_2}$ is the radial integral for the initial and final states. A double sum for the final orbital angular momenta has to be considered for the angular distribution :

$$W(\vartheta_1) \propto \sum_{M_1 M_2 S l_2 l_2^* P} |Q_{M_1 M_2 P}(l_2 l_2^*)|^2$$

Applying

$$\sum_{M_1} (l_2 M S M_1 \mid J_2 M + M_1) (l_2^* M S M_1 \mid J_2 M + M_1) \propto \delta_{l_2 l_2 *}$$

the angular distribution $W_{l_2}(\vartheta_1)$ becomes

$$W(\vartheta_1) = \sum_{l_2} z(l_2) W_{l_2}(\vartheta_1)$$

Experiments allow to extract the weighting factors $z(l_2)$.

In the final angular distributions the interference terms have to be considered if the direct-capture transition to a final state with unique orbital angular momentum l_2 can proceed from several initial partial waves l_1 via the emission of different orders of electric multipole transitions (LM). For the initial state the wave function including the radial dependence is given by:

$$|J_1 M_1\rangle \propto \sum_{S_1 l_1} l_1 i^{l_1} \exp(i\varphi_{l_1}) \frac{u_{l_1}(k_1 r)}{k_1 r} \mathscr{Y}_{l_1}^{0}(\vartheta, \varphi) \chi_{S_1}^{M_1}$$

with

$$\varphi_{l_1} = \sigma_{l_1} - \sigma_0 + \delta_{l_1}$$

As in the previous paragraph, the transition matrix element is given here by

$$Q_{M_1M_2P} \propto \sum_{Sl_1} i^{l_1} \exp\left(i\varphi_{l_1}\right) a_S^* \hat{L} l_1^2 \hat{l}_2^{-1} \left(l_2 M_2 - M_1 S M_1 \mid J_2 M_2\right) \times \left(l_1 0 L 0 \mid l_2 0\right) \left(l_1 0 L M \mid l_2 M\right) R_{l_1 L l_2} D_{MP}^{(L)*}$$

where $R_{l_1 L l_2}$ is the radial integral for the initial and final states. Then the sum of the individual angular distributions and the interference terms give the resultant angular distribution :

$$W\left(\vartheta_1\right) = \sum_{l_1 L} W_{l_1 L l_2}\left(\vartheta_1\right)$$

Generally, the interference term is given by twice the real part of the squared transition matrix element:

$$W_{l_1 L l_2 l_1^* L^* l_2}\left(\vartheta_1\right) = 2\cos\left(\varphi_{l_1} - \varphi_{l^*}\right)(-)^{l_1^* + L_1^* + l_2} \times \sum_k \left(l_1 0 l_1^* 0 \mid k 0\right) \bar{Z}_1\left(l_1 L l_1^* L^*; l_2 k\right) P_k\left(\vartheta_1\right)$$

The contributions of the individual components to $W\left(\vartheta_1\right)$ depend on the radial matrix element, i.e. on the relative cross sections.

The interference that occurs most commonly is that between E1 transitions from two initial partial waves l_1 and $(l_1 + 2)$ to a final orbit l_2. For this scenario, only a $k = 2$ interference term occurs. E1/E2 or E1/M1 types of interference can also become prominant under certain conditions.

2.3.2 ANGULAR DISTRIBUTIONS FOR SECONDARY TRANSITIONS

For a secondary γ-ray transition $(L_2\mu_2)$ in the $\gamma - \gamma$ cascade between the states $|J_1 M_1\rangle \rightarrow |J_2 M_2\rangle \rightarrow |J_3 M_3\rangle$ with the primary γ-ray transition $(L_1\mu_1)$ unobserved, the angular distribution is given by [RB67]

$$W\left(\vartheta_2\right) \propto \int \mathrm{d}\Omega_1 \sum_{M_1 M_3 P_1 P_2} \mid \sum_{\mu_1\mu_2 M_2} \left\langle J_2 M_2 \left| T_{L_1\mu_1} \right| J_1 M_1 \right\rangle D_{\mu_1 P_1}^{(L_1)*}\left(\vartheta_1, \varphi_1, 0\right) \times \left\langle J_3 M_3 \left| T_{L_2\mu_2} \right| J_2 M_2 \right\rangle D_{\mu_2 P_2}^{(L_2)*}\left(\vartheta_2, \varphi_2, 0\right)\Big|^2$$

doing the integration which becomes [RB67]

$$W\left(\vartheta_2\right) \propto \sum_{M_1 M_2 M_3 \mu_1 \mu_2 P_2} \left|\left\langle J_2 M_2 \left| T_{L_1\mu_1} \right| J_1 M_1 \right\rangle \left\langle J_3 M_3 \left| T_{L_2\mu_2} \right| J_2 M_2 \right\rangle D_{\mu_2 P_2}^{(L_2)*}\left(\vartheta_2, \varphi_2, 0\right)\right|^2$$

Here the primary transition arises from the direct-capture process and the wave functions of the first two states are given by the model [Rol73], thus the first matrix element can be obtained:

$$\langle J_2 M_2 \left| T_{L_1 \mu_1} \right| J_1 M_1 \rangle \propto \left(l_2 \mu_1 S M_1 \mid J_2 M_2 \right) \left(l_1 0 L_1 0 \mid l_2 0 \right) \left(l_1 0 L_1 \mu_1 \mid l_2 \mu_1 \right)$$

Using the Wigner-Eckart theorem, the second matrix element becomes

$$\langle J_3 M_3 \left| T_{L_2 \mu_2} \right| J_2 M_2 \rangle = \left(J_2 M_2 L_2 \mu_2 \mid J_3 M_3 \right) \langle J_3 || T_{L_2} || J_2 \rangle$$

The angular distribution can therefore be written as

$$\begin{aligned} W\left(\vartheta_2\right) \propto & \sum_{M_1 M_2 M_3 \mu_1 \mu_2} \left(l_2 \mu_1 S M_1 \mid J_2 M_2 \right)^2 \left(l_1 0 L_1 0 \mid l_2 0 \right)^2 \left(l_1 0 L_1 \mu_1 \mid l_2 \mu_1 \right)^2 \\ & \times \left(J_2 M_2 L_2 \mu_2 \mid J_3 M_3 \right)^2 \left(L_2 1 L_2 - 1 \mid k 0 \right) \left(L_2 \mu_2 L_2 - \mu_2 \mid k 0 \right) P_k\left(\vartheta_2\right) \end{aligned}$$

Using the CG and Racah coefficients relations, the summation over the magnetic indices results in

$$\begin{aligned} W\left(\vartheta_2\right) = \sum_k & \left(l_1 0 l_1 0 \mid k 0 \right) W\left(l_1 \; l_2 l_1 l_2; L_1 k \right) \\ & \times W\left(J_2 l_2 J_2 l_2; S k \right) \bar{Z}_1\left(L_2 J_2 L_2 J_2; J_3 k \right) P_k\left(\vartheta_2\right) \end{aligned}$$

In the case of the direct-capture transition (unobserved primary) from several partial waves l_1 to several orbits l_2 in the intermediate state, the final angular distribution for the secondary transition is given by an incoherent sum over the individual components:

$$W\left(\vartheta_2\right) = \sum_{l_1 l_2} \sigma_{l_1 l_2} W_{l_1 l_2}\left(\vartheta_2\right)$$

where the weighting factors $\sigma_{l_1 l_2}$ can be obtained from the primary transitions. Direct-capture model calculations can also be used to find $\sigma_{l_1 l_2}$.

Using above equations, the γ-ray angular distribution for the nth secondary transition can be calculated as:

$$\begin{aligned} W\left(\vartheta_n\right) \propto & \sum_k \left(l_1 0 l_1 0 \mid k 0 \right) W\left(l_1 l_2 l_1 l_2; L_1 k \right) \\ & \times W\left(J_2 l_2 J_2 l_2; S k \right) W\left(J_2 J_3 J_2 J_3; L_2 k \right) \ldots W\left(J_{n-1} J_n J_{n-1} J_n; L_{n-1} k \right) \\ & \times \bar{Z}_1\left(L_n J_n L_n J_n; J_{n+1} k \right) P_k\left(\vartheta_n\right) \end{aligned}$$

If the m th intermediate (unobserved) transition is composed of two multipoles $(L_m L_m^*)$, then the angular distribution will be

$$W\left(J_m J_{m+1} J_m J_{m+1}; L_m k\right) + \delta^2 W\left(J_m J_{m+1} J_m J_{m+1}; L_m^* k\right)$$

where δ is the multipole mixing ratio. In this case, the appropriate Racah coefficient has been used [RB67]

2.4 γ-ray Angular Distribution of ^{16}O(p,γ)^{17}F reaction

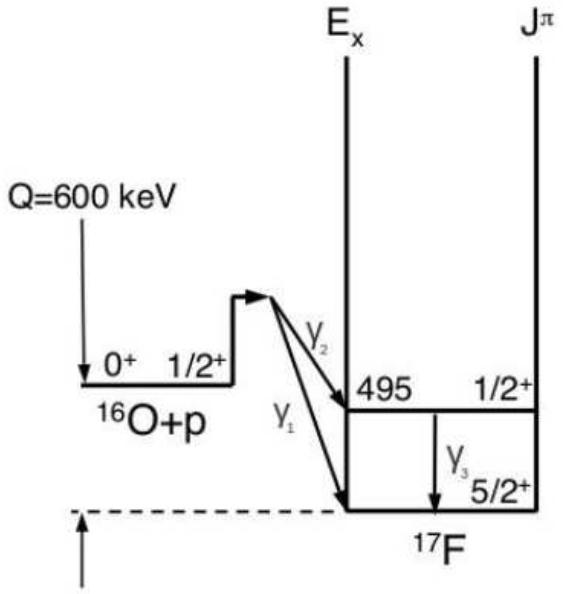

Figure 2.5. Nuclear energy level diagram for the reaction ^{16}O(p,γ)^{17}F [Ili08]

The radiative proton capture on ^{16}O, with Q_{value} = 600.27±0.25 keV, can proceed either to the ground state ($J^\pi = 5/2^+$) or to the first excited state (E_x = 495.33±0.10 keV; $J^\pi = 1/2^+$) of ^{17}F [Ili08]. The transition to the ground state for the ^{16}O(p, γ)^{17}F reaction proceeds predominantly via E1 radiation and angular momenta of $\ell_i = 1, 3\,(J_i = 3/2^-, 5/2^-, 7/2^-) \rightarrow \ell_f = 2\,(J_f = 5/2^+)$ (DC $\rightarrow$ 0), while the transition to the first excited state at E_x = 495 keV proceeds via E1 radiation and angular momenta of $\ell_i = 1\,(J_i = 1/2^-, 3/2^-) \rightarrow \ell_f = 0\,(J_f = 1/2^+)$ (DC $\rightarrow$ 495). The M1 or E2 transitions are negligible for the direct proton capture on ^{16}O [Ili08].

The nuclear level diagram is shown in Fig. 2.5.

The theoretical angular distributions provided by the study of the direct capture process in the reaction ^{16}O(p, γ)^{17}F are [Rol73]:

$$\begin{array}{ll} \text{E1(p} \to \text{s)} & W(\vartheta) = 1 - P_2(\vartheta) = \sin^2\vartheta \\ \text{E1(p} \to \text{d)} & W(\vartheta) = 1 - \frac{1}{10}P_2(\vartheta) = 1 + \frac{1}{6}\sin^2\vartheta \\ \text{E1(f} \to \text{d)} & W(\vartheta) = 1 - \frac{2}{5}P_2(\vartheta) = 1 + \sin^2\vartheta \end{array}$$

In fig. 2.6 the solid lines represent model predictions [Rol73].

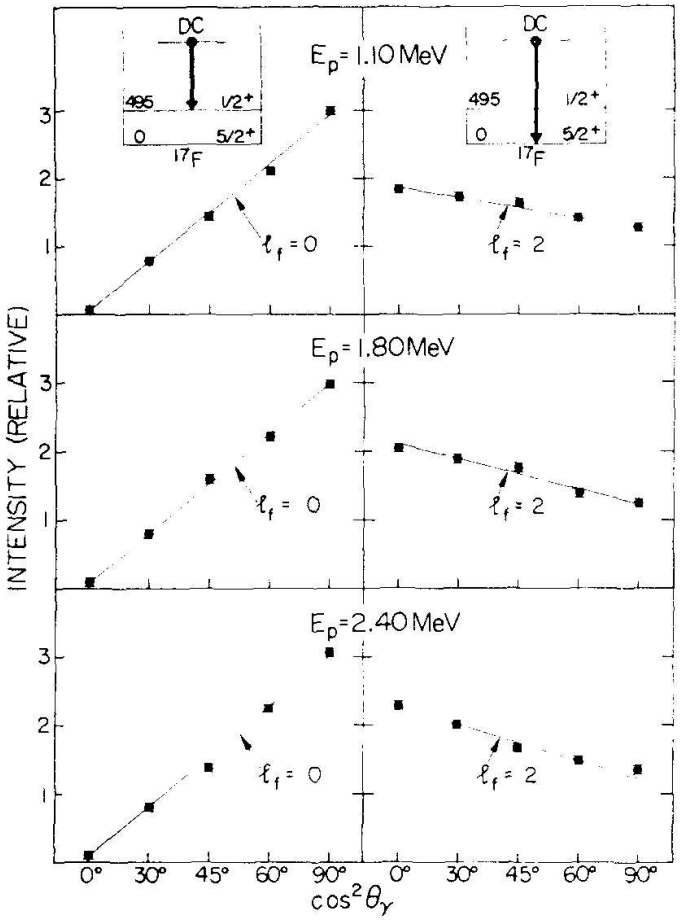

Figure 2.6. Angular distributions for the DC $\to$ 0 and DC $\to$ 0.50 MeV γ-ray transitions as observed in the reaction ^{16}O(p,γ)^{17}F at E_p = 1.10, 1.80 and 2.40 MeV [Rol73]

The angular distribution for the direct capture γ-ray transition is given by:

$$W(\vartheta) = \sum_k (l_\mathrm{i} 0 l_\mathrm{i} 0 \mid k0)\, Z_1\,(L l_\mathrm{i} L l_\mathrm{i}; l_\mathrm{f} k)\, Q_k P_k(\vartheta) \tag{2.16}$$

Eq. 2.16 depends only on the orbital angular momenta l_i and l_f of the initial and final state, respectively and on the multipole order, L, of the γ-ray transition.

Eq. 2.16 is not only independent of the total spin J of the final state but also of the channel spin $\boldsymbol{S} = \boldsymbol{j}_\mathrm{p} + \boldsymbol{j}_\mathrm{t}$ (i.e. the intrinsic spins of the target nucleus j_t and projectile j_p).

In previous studies of the ^{16}O(p,γ)^{17}F reaction, observation of large anisotropies attributed to $W(\vartheta) = \sin^2\vartheta$ have lead to the identification of E1(p $\rightarrow$ s) direct capture transitions. In these cases targets with spin $j_\mathrm{t} = 0$ or $\frac{1}{2}$ were used. Nevertheless, the large observed anisotropies could also have been due to the tails of distant resonances [Rol73].

The γ-ray angular distribution for E1 transitions, which proceed from two initial partial waves l_i and $l_\mathrm{i}^* = l_\mathrm{i} + 2$, includes an interference term $W^{i\ \mathrm{int}}_{l_1,l_\mathrm{i}^*}(\vartheta)$ between the two E1 transitions:

$$W(\vartheta) = \frac{1}{1+y}\left[W_{l_\mathrm{i}}(\vartheta) + yW_{l_\mathrm{i}} * (\vartheta) + 2\sqrt{y}\cos\varepsilon W^{\mathrm{int}}_{l_\mathrm{i}\mathbf{i}_\mathrm{i}}(\vartheta)\right] \tag{2.17}$$

where y is the ratio of the cross sections, $y = \sigma\left(l_\mathrm{i}^* \rightarrow l_\mathrm{f}\right)/\sigma\left(l_\mathrm{i} \rightarrow l_\mathrm{f}\right)$, and ε is given by the usual Coulomb (φ_{l_1}) and nuclear phase shifts (δ_{l_1}) : $\varepsilon = \varphi_{l_1{}^*} - \varphi_{l_\mathrm{l}} + \delta_{l_l{}^*} - \delta_{l_1}$. Hence, ε is a phase factor. The ratio y can be estimated from the direct capture model calculations. The φ_{li} can be measured from the Coulomb phases [Fer65] [RB67]. The δ_{l_i} can be obtained from a phase shift analysis of elastic scattering data. Consequently, $E1(p \rightarrow d)$ and $E1(f \rightarrow d)$, the interference term is

$$W^{\mathrm{int}}_{\mathrm{pf}}(\vartheta) = \frac{3}{5}\sqrt{\frac{3}{2}}P_2(\vartheta)$$

and hence

$$W(\vartheta) = 1 + \frac{-0.10 + 1.47\sqrt{y}\cos\varepsilon - 0.40y}{1+y}P_2(\vartheta)$$

The direct capture model determines all parameters. An experiment to do the measurement of the angular distribution of the above type at several beam energies is crucial to validate the model.
In the case of the final state which is described by two orbital angular momenta, l_f and $l_\mathrm{f}^* = l_\mathrm{f} + 2$, the γ-ray angular distribution can be expressed, as an incoherent sum of the individual γ-ray angular distributions:

$$W(\vartheta) = \frac{1}{1+z}\left[W\left(\vartheta, l_\mathrm{i} \rightarrow l_\mathrm{f}\right) + zW\left(\vartheta, l_\mathrm{i} \rightarrow l_\mathrm{f}^*\right)\right] \tag{2.18}$$

where the expression is weighted by the ratio of the cross sections $z = \sigma\left(l_\mathrm{i} \rightarrow l_\mathrm{f}^*\right)/\sigma\left(l_\mathrm{i} \rightarrow l_\mathrm{f}\right)$. Experiment gives the ratio z give insight on the two components l_f and l_f^* in the final-state wave functions. No further parameters are required in the analysis of the more complicated case of orbital mixing in the initial as well as final state,

since the orbital mixing in the initial state is determined entirely by the direct capture model.
The γ-ray angular distribution for subsequent secondary γ-radiation following the direct capture transition is given by:

$$W(\vartheta) = \sum_{kL_2L_2{}^*} (l_\mathrm{i}0l_\mathrm{i}0 \mid k0)\, W\left(l_\mathrm{i}l_\mathrm{f}l_\mathrm{i}l_\mathrm{f}; L_1k\right) \times W\left(J_\mathrm{f}l_\mathrm{f}J_\mathrm{f}l_\mathrm{f}; Sk\right) \delta^r \bar{Z}_1\left(L_2J_\mathrm{f}L_2^*J_\mathrm{f}; J_\mathrm{e}k\right) Q_k P_k(\vartheta) \tag{2.19}$$

where L_1 and (L_2, L_2^*) are the multipoles of the primary and secondary γ-ray transitions, respectively, δ^r is the multipole mixing ratio of the secondary transition [Fer65], S is the channel spin $\left(\boldsymbol{S} = \boldsymbol{j}_\mathrm{t} + \boldsymbol{j}_\mathrm{p}\right)$ and J_f and J_c are the total spins of the states involved in the secondary transition ($J_\mathrm{f} \rightarrow J_\mathrm{e}$). The first Racah coefficient $W\left(l_\mathrm{i}l_\mathrm{f}l_\mathrm{i}l_\mathrm{f}; L_1k\right)$ corresponds to the "unobserved" primary transition and the second Racah coefficient represents the transformation from the orbital angular momenta representation to the total spin representation [Rol73].

In ^{16}O(p,γ)^{17}F reaction, the direct capture process for target spins $j_t \neq 0$ concerns the angular distribution of the secondary transitions where $l_\mathrm{f} = 0$. Here the direct capture primary has a large anisotropy corresponding to $W(\vartheta) = \sin^2\vartheta$ and the secondary transition is isotropic (independent of J_f).

In the case of mixed orbital angular momenta, l_f and $l_\mathrm{f} + 2$, in the final-state wave function, the angular distribution of the secondary transitions is given by the incoherent sum of the two components from eq. 2.19 weighted by the ratio z (eq. 2.18.

The secondary γ-ray angular distributions provide information of the j_f value of the final orbit $\left(j_\mathrm{f} = l_\mathrm{f} - \frac{1}{2}\right.$ and/or $\left.j_\mathrm{f} = l_\mathrm{f} + \frac{1}{2}\right.$ for direct proton capture). It is important for direct capture by target nuclei with $j_\mathrm{t} \neq 0$. If S_1 and S_2 are the two possible channel spins with $W_{S_\mathrm{i}}(\vartheta)$ given by eq. 2.19, the observed angular distribution becomes

$$W(\vartheta) = \frac{1}{1+t}\left[W_{s_1}(\vartheta) + tW_{s_2}(\vartheta)\right] \tag{2.20}$$

where t is the channel spin intensity ratio, defined by $t = I\left(S_2\right)/I\left(S_1\right)$ and can be deduced experimentally.

3 The $^{16}O(p,\gamma)^{17}F$ reaction

The present LUNA-400kV activity is mainly focused on investigating the fundamental nuclear processes occurring during H-burning at different stages of stellar evolution. H-burning can occur through distinct proton captures and beta decays sequences, depending on the core temperature. The CNO cycle dominates over the pp-chain for temperatures above 20 MK and is the main source of energy in the cores of main sequence stars with a mass of more than 1.5 solar masses. The $^{16}O(p,\gamma)^{17}F$ reaction is part of the CNO cycles involved in hydrogen burning. This reaction has an important effect in main-sequence stars as well as in more evolved objects like red-giant and asymptotic-giant stars. It can also occur during nova outbursts that are fueled by explosive hydrogen burning. In this chapter, the astrophysical motivation, the state of art and the outline of the experimental approach of the $^{16}O(p,\gamma)^{17}F$ reaction will be presented.

3.1 Astrophysical motivation

The reactions going on during the CNO cycle inside the H-burning zone of the stars are illustrated in Figure 3.1. The $^{16}O(p,\gamma)^{17}F$ reaction is involved in the so called CNO-II cycle and subsequent. Specifically, its reaction rate directly influences the relative abundances of ^{16}O and ^{17}O in the H-burning zone. The $^{16}O/^{17}O$ abundance ratio is commonly measured in the atmospheres of red-giant, asymptotic-giant, and red supergiant stars by observing the infrared lines (IR) of CO molecules. Moreover, Oxygen isotopes are observed in presolar grains that are buried in pristine meteorites. Presolar grains are believed to originate in the colder atmospheres of giant stars during mass depletion phases, crucial for the chemical enrichment of the interstellar medium and ultimately of the galactic chemical evolution. For these reasons the $^{16}O/^{17}O$ abundance ratio is a useful tool to trace mixing processes occurring in giant stars and the chemical evolution of the Galaxy.

In a recent sensitivity study the $^{16}O/^{17}O$ observed ratios, as reported in [LSH+15] for intermediate mass RGB stars of galactic open clusters, have been compared with theoretical predictions of stellar models assuming different rates for the $^{16}O(p,\gamma)^{17}F$ reaction, see Figure 3.2. An increase in the presently accepted rate may reduce theory-observation discrepancy.

In AGB stars the $^{16}O(p,\gamma)^{17}F$ reaction is not only crucial for stellar nucleosynthesis. Figure 3.3 displays a comparison of the positions of the H-burning shell in a 6 $M_\odot$ AGB star, which represents the spots where the nuclear energy production rate reaches its maximum, assuming two different $^{16}O(p,\gamma)^{17}F$ rates. Saw-tooths in Figure 3.3 mark the recursive penetrations of the H-rich envelope into the He-rich

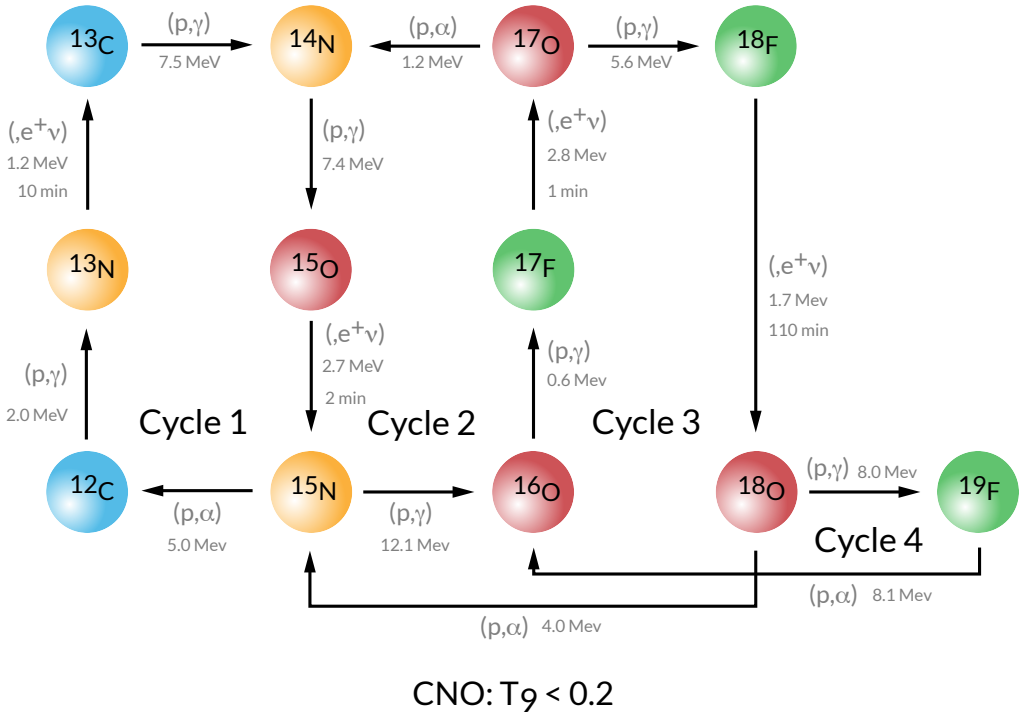

Figure 3.1. CNO cycles I, II, III, and IV [Coc23]

mantle, which shows that the reaction rate impacts the mixing process efficiency.

In a nutshell, the ^{16}O(p,γ)^{17}F reaction rate plays a crucial role in modelling red and asymptotic giant stars, impacting the theoretical predictions of several physical and chemical properties.

3.2 State of the art

The ^{16}O(p,γ)^{17}F reaction (Q = 600.27 keV) occurs via direct capture to the ground state or to the first excited state of ^{17}F at E_x = 495.33 keV. The ^{17}F is a radioactive isotope (half-life = 64.49 s) that undergoes β^+ decay (emitting a positron) to form ^{17}O . The cross section for the reaction ^{16}O(p,γ)^{17}F has been previously determined using two methods: the activation technique, which involves counting the number of ^{17}F decays after exposing the sample to a beam, and the detection of prompt gamma radiation. Activation experiments solely quantify the overall cross section, whereas prompt-gamma experiments may analyse the individual contributions of direct capture to the ground state and first excited state of ^{17}F.

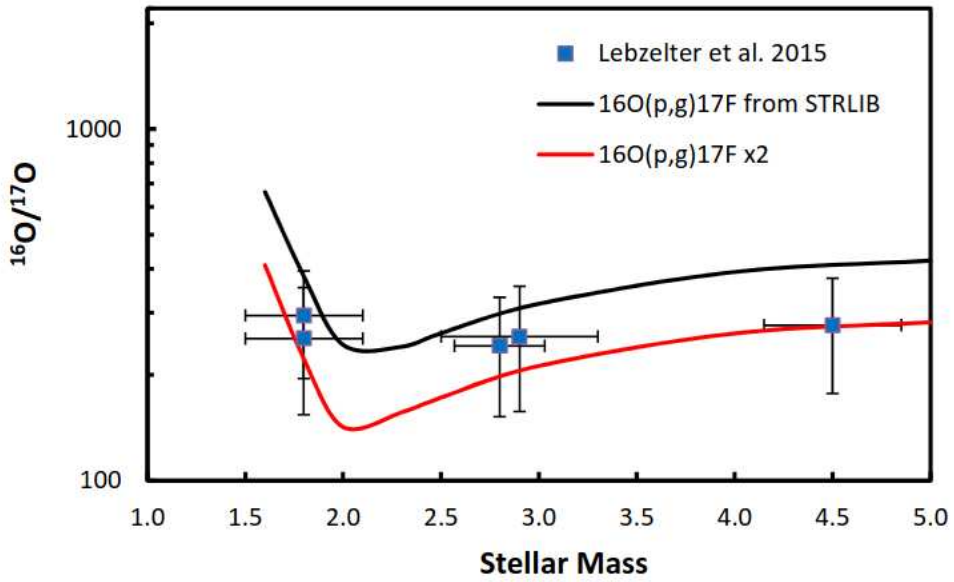

Figure 3.2. The $^{16}O/^{17}O$ abundance ratios observed in open cluster red giant stars of different masses (squares) compared against theoretical predictions (lines).

Figure 3.4 presents a concise overview of the data available in literature for the $^{16}O(p,\gamma)^{17}F$ reaction S-factor. The region of interest of the Gamow peak is indicated by the orange band, and it goes from 20 up to 120 keV depending on the astrophysical scenario. It is clear from the plot that none of the datasets directly populate the Gamow window. Consequently, to assess the thermonuclear reaction rate, extrapolations must be employed. In 2008, Iliadis et al. [Ili08] conducted a comprehensive review of all applicable datasets. The authors discovered that all the published data required adjustments to account for systematic uncertainties that were not addressed in the original articles. These adjustments included accounting for the impacts of coincidence summing and incorporating updated stopping powers. As an illustration, Hester et al. [HPL58] adjusted their data by considering updated stopping power values, which resulted in a reduction of the cross sections by a factor of 2% - 8% (depending on the energy). The data of Tanner et al. [Tan59] should undergo the same modification, however, this was not easy to implement because the paper lacks experimental yield information. Consequently, Iliadis et al. dismissed the data set. The data from Rolfs [Rol73] were also excluded from consideration since the cross section was normalised to Tanner et al. In the study conducted by Chow et al. [CGH75], it was found that the uncertainties were initially overestimated. As a result, the error bars were adjusted to a minimum of 5%, increasing from the original 3%. The data provided by Molrock

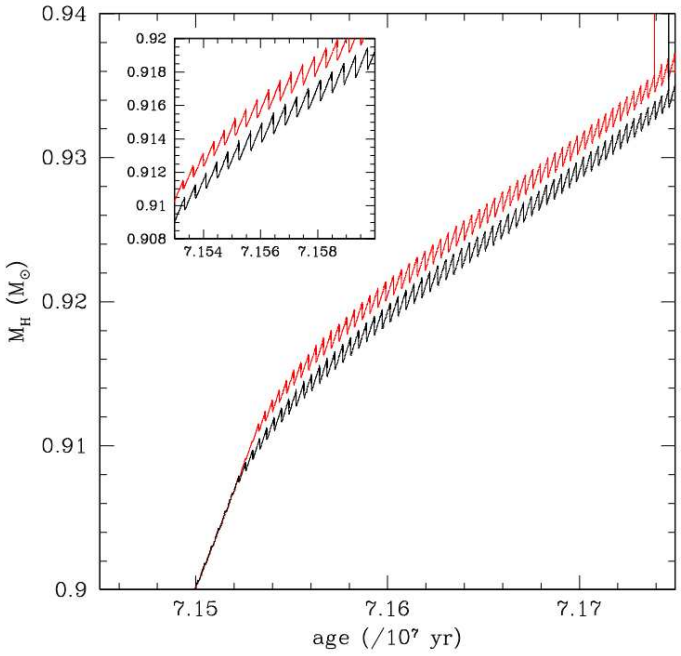

Figure 3.3. The two lines show the evolution during the AGB phase of the position (in mass coordinates) of the H-burning shell, for two models of 6 $M_\odot$ stars.

et al. [Mor97] were adjusted to compensate for the coincidence summation effect in the γ detector. The modification resulted in a decrease of approximately 10% in the low energy cross section. Furthermore, a 10% uncertainty was incorporated into the data, as indicated by Morlock's PhD thesis.

Following the application of all necessary modifications, the data were analysed using two distinct approaches: a potential model and the R-matrix theory. The results obtained were merged to assess a proposed S(E) factor and its corresponding reaction rate. The uncertainty for the reaction rate is less than 7%. Mohr and Iliadis [MI12] recently evaluated a new recommended absolute cross-section for the $^{16}O(p,\gamma)^{17}F$ reaction in the proton energy range from 500 to 2500 keV, aiming to use it as a benchmark for ion beam analysis. Cross sections for the ground state and first excited state capture have been provided by them. An uncertainty of 5% has been applied to the evaluation of both cross sections.

The above discussion emphasizes the necessity for new experimental data, accompanied by a thorough assessment of all potential systematic influences.

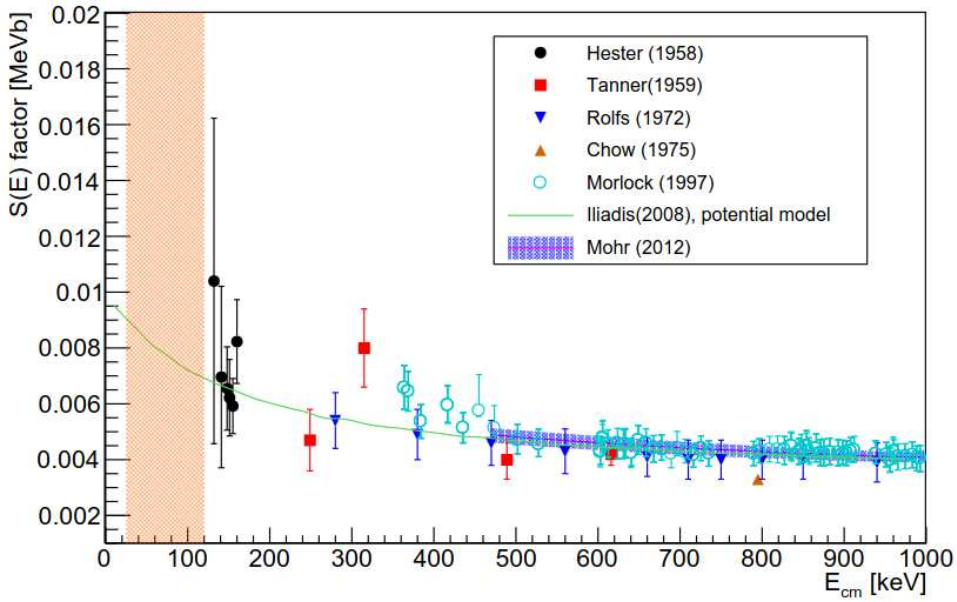

Figure 3.4. Data for the ^{16}O(p,γ)^{17}F cross section up to 1 MeV.

3.3 Objective of Angular Distribution Measurement

The state of the art described in previous section is focused on the ^{16}O(p,γ)^{17}F reaction cross-section. A significant issue in determining the cross-sections σ_0 and σ_1, corresponding to the cross section for the transition to the ground state (g.s. $5/2^+$) and the first excited state (495 keV, $1/2^+$), respectively, is the angular distribution of the emitted γ-rays. The transition to the first excited state is mostly influenced by the E1 transition from the incoming p-wave to the bound $1/2^+$ s-wave state. The contribution from the E2 transition originating from the incoming d-wave has no significant impact on the angular distribution, $W_1(\theta) \sim sin^2\theta$. The experimental confirmation of the form of $W_1(\theta)$ is documented in references [Rol73], [CGH75]. The most accurate measurement of the cross-section σ_1 can be obtained when θ is set to 90°. The angular distribution $W_1(\theta)$ of this transition reaches its peak at this point, and the theoretical value of $W_1(\theta)$ can be used in the analysis along with the solid angle of the gamma-ray detector with minimal errors.

Nevertheless, the angular distribution for the transition to the ground state exhibits a noticeably distinct behaviour. The contributions from E1 and E2 transitions from the incoming $s-$, $d-$, and $f-$waves to the dominant E1 $p-$wave capture have a relatively small impact on the angular distribution $W_0(\theta)$. This results in an additional uncertainty of approximately 10% for σ_0 [MI12]. This

uncertainty arises because the calculation relies on either interpolating between the experimental data, as done by [Rol73] and [CGH75], or using theoretical estimates for $W_1(\theta)$. Given that the cross-section σ_0 is consistently smaller than σ_1 across the entire range of energies being examined, it is generally satisfactory to determine the oxygen abundance by solely using the dominant σ_1 cross-section. Consequently, the aforementioned uncertainty in $W_1(\theta)$ does not pose a significant limitation for the practical use of the ^{16}O(p,γ)^{17}F reaction in stellar model applications. In the work done by P. Mohr and C. Iliadis in 2012, Table-1 [MI12] comprises the recommended cross-sections σ_0 and σ_1 of the ^{16}O(p,γ)^{17}F reaction with the ratio $R = \sigma_1/\sigma_0$. However, to obtain an accurate measurement of the σ_0 cross-section, it is necessary to estimate the angular distribution $W_1(\theta)$.

3.4 Experimental approach

The objective of the measurement conducted at LUNA is to obtain accurate data at proton energies below 400 keV. These measurements aim to bridge the gap between the data-sets provided by Morlock et al. [Mor97] and Hester et al. [HPL58], while also minimising the current uncertainties associated with cross section extrapolation to astrophysical energies. Two distinct experimental methodologies have been employed: prompt-gamma detection and activation method. The prompt-gamma experiment enables us to precisely evaluate the separate contributions of the transitions to the ground state and the 495.33 keV excited state of ^{17}F, as well as accurately measure the angular distribution of emitted gamma rays. In contrast, the activation measurement yields the overall cross section without being influenced by angular distribution effects or environmental background. Consequently, the Angular Distribution of the ^{16}O(p,γ)^{17}F reaction has been studied in this thesis using the prompt-gamma detection method. The measurement has been carried out by impinging a proton beam onto solid Ta_2O_5 targets. The targets are manufactured by anodic oxidation of tantalum backings that are 0.2 mm thick [Cac12]. This particular type of targets has been extensively utilised at LUNA in previous investigations involving the collision of ^{17}O+p and ^{18}O+p particles [Bru16] [Bru19]. The fabrication procedure for these targets is firmly established at LNGS.

3.4.1 Prompt-gamma measurement

For the prompt-gamma experiment, one HPGe detector and two $CeBr_3$ detectors have been used. The HPGe detector is positioned in close geometry to the target at an angle of 55° with respect to the beam line. On the other hand, the two $CeBr_3$ detectors have been positioned at angles 0° and 90° around the target. $CeBr_3$ scintillator detectors exhibit excellent energy resolution (4% at 662 keV), which

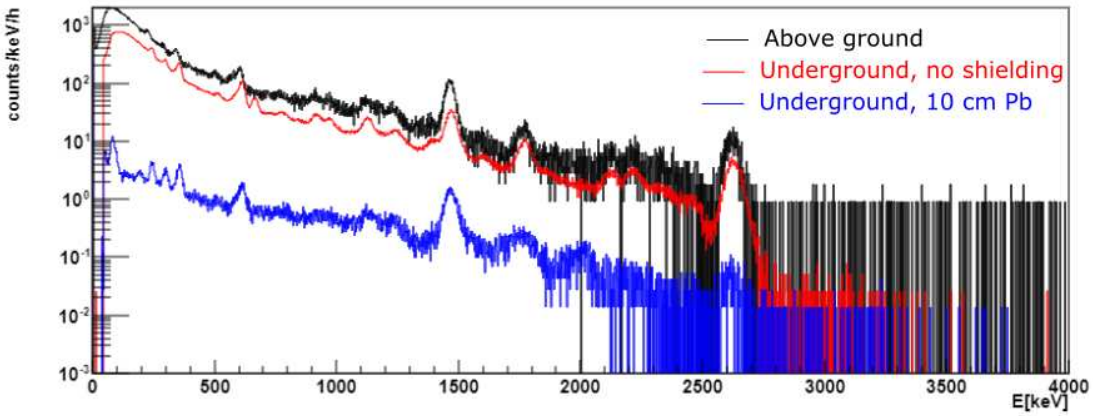

Figure 3.5. Environmental background measured with a 2"x2" CeBr3 detector.

is nearly twice as good as NaI detectors. Additionally, $CeBr_3$ detectors have a greater density of 5.23 g/cm^3 compared to NaI density of 3.67 g/cm^3. Furthermore, $CeBr_3$ detectors have a low intrinsic background. The background level in $CeBr_3$ detectors has been assessed in underground situations, specifically in the regions of interest for the $^{16}O(p,\gamma)^{17}F$ reaction. This assessment was conducted using a 10 cm thick lead shielding, reducing the background radiation as depicted in Figure 3.5. Due to the low Q value of the $^{16}O(p,\gamma)^{17}F$ reaction, the γ-rays of interest cover, indeed, an energy range where the environmental background is mostly influenced by naturally-occurring radioactive isotopes. That is why, a 10-cm thick layer of lead shielding has been placed around all detectors. This ensures a reduction in background noise by a factor of 100.

4 Experimental Setup

In this chapter, the experimental setup will be described in details. The arrangement of detectors and the targets characteristics will be discussed.

4.1 Experimental equipment

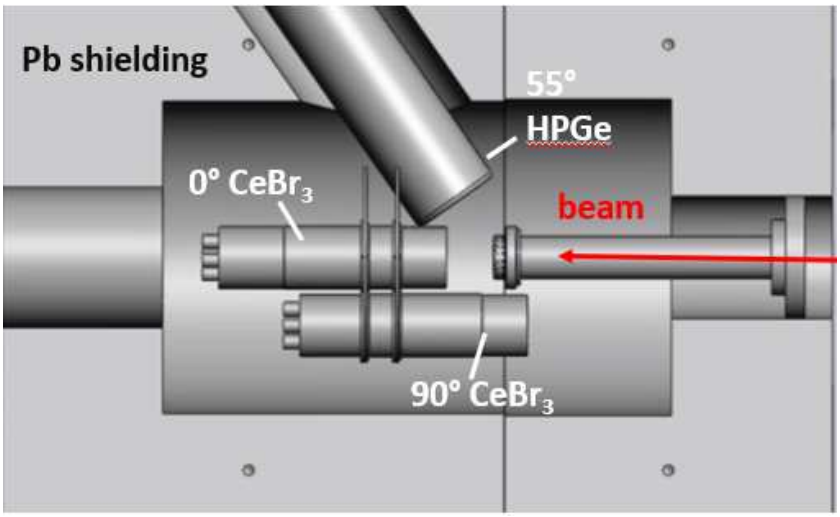

Figure 4.1. Schematic diagram of the setup for studying the γ-ray Angular Distribution of ^{16}O(p,γ)^{17}F reaction

Proton capture on ^{16}O is part of the CNO cycle of hydrogen burning and it proceeds through ^{16}O(p,γ)^{17}F reaction. The ^{16}O(p,γ)^{17}F reaction affects the isotopic abundances of $^{17,18}O$. The $^{16}O/^{17}O$ ratio influence the HBB (Hot Bottom Burning) stage of AGB (Asymptotic Giant Branch) stars and contribute to TDU (Third Dredge Up) process. The ^{16}O(p,γ)^{17}F reaction has been studied by many groups, and in order to explain the angular distribution of the emitted γ-ray at the Gamow window, an improved set of the experimental data is required, minimizing the existent systematic as well as measurement uncertainties. At astrophysical energies, the ^{16}O(p,γ)^{17}F cross section depends on the direct capture component. The direct-capture cross section have been studied at LUNA combining prompt gamma-ray spectroscopy and the activation technique [Axn22]. The prompt gamma-ray spectroscopy allowed us to detect the angular distribution of the emmtted γ radiation. In order to verify the data obtained so far, a measurement of the ^{16}O(p,γ)^{17}F reaction has been performed at the LUNA solid target beam line. At LUNA, the ^{16}O(p,γ)^{17}F reaction has been studied delivering the proton beam to solid Ta_2O_5 targets. The experiment was performed with the

0.25 mm thick solid Ta_2O_5 target, surrounded by two different types of gamma detectors, two $CeBr_3$ detectors and one HPGe detector. Gamma rays from the reaction were detected using a HPGe detector in close geometry at 55°, while the two $CeBr_3$ detectors positioned at 0° and 90° with respect to the beam line (Fig. 4.1). The detectors were surrounded by a 10 cm thick lead shielding [Axe18]. The set-up allows us to infer the angular distribution of gamma ray energies exploiting the high energy resolution of the germanium detector and the high efficiency of the $CeBr_3$ detectors. Despite the close geometry, effects of angular distribution are expected in this configuration. Understanding better those effect will permit to include those corrections in the cross section analysis. The goal of this thesis is to understand the angular distribution correction, while the cross section analysis will be beyond the scope of the present work. Targets of the same composition were used (tantalum oxide with 0.2 ml ^{18}O (80%) + 1.9 ml UPW-Sigma) in order to keep possible systematic effects minimum due to the target composition and thickness. Several long runs were performed with beam energy starting from 370 keV upto 398 keV. The data taking was completed in February 2023 and the analysis is presently ongoing.

4.1.1 Overview: LUNA facility

As briefly mentioned also in previous chapter, the environmental background is generated by cosmic rays and the disintegration of naturally-occurring radioactive isotopes, such as uranium and thorium chains, as well as ^{40}K. To significantly decrease the background caused by radioactive isotopes, one can employ a detector shielded with materials that have high atomic number (Z) and high density, typically lead or copper. On the other hand, cosmic radiation encountered at sea level primarily consists of muons, which are extremely penetrating particles formed in the upper atmosphere. These particles can penetrate most particles on earth and gamma ray detectors and have the ability to induce spallation reactions in the materials of the detector and its surroundings. As a result, this can lead to the production of neutrons and radioactive nuclei. To effectively reduce the environmental background, it is preferable to conduct research in underground laboratories located at considerable depths. Thick layers of rock can greatly reduce the number of cosmic muons that reach a detector. Additionally, thicker linings can be used to shield detectors from low-energy gamma background when they are underground. This is because the emission of radiation from the interaction of cosmic rays within the shielding becomes insignificant [Axe18], [A.16], [LUN10].

The LUNA (Laboratory for Underground Nuclear Astrophysics) project is a groundbreaking endeavour in the field of deep underground Nuclear Astrophysics. LUNA is located at Laboratori Nazionali del Gran Sasso - INFN (LNGS), which

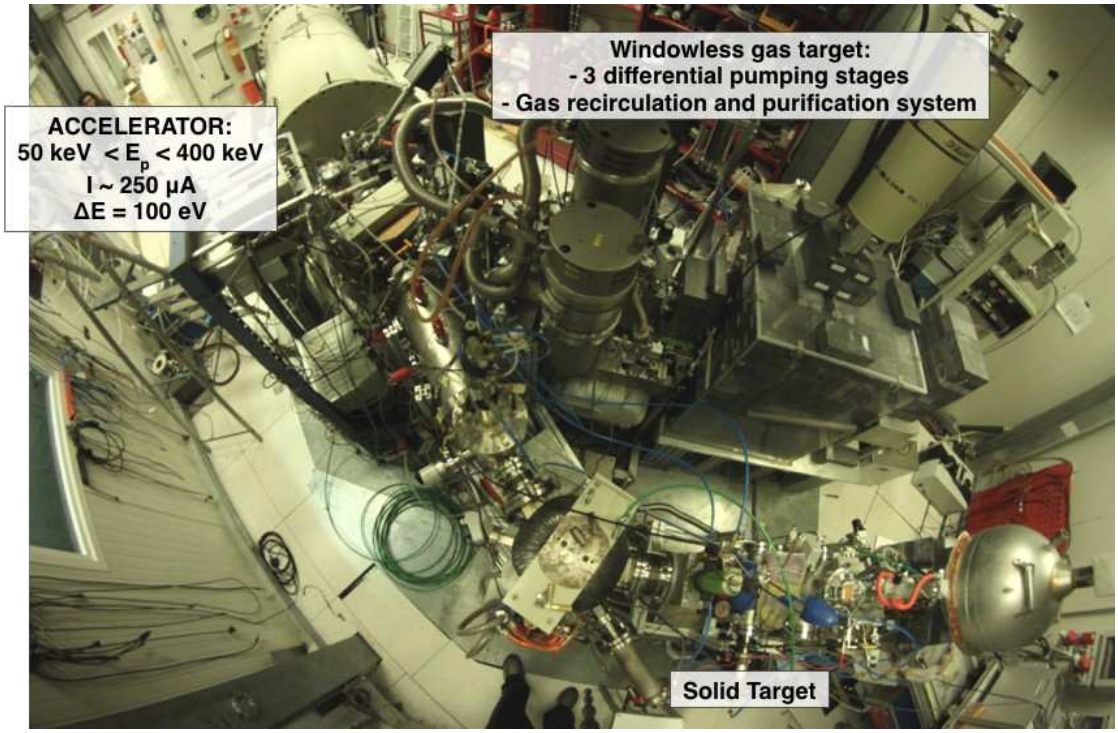

Figure 4.2. Wide angle photo of the LUNA experimental hall.

is established under the mountain Gran Sasso, situated in central Italy. The laboratory is protected by a layer of 1400 metres of mountain rocks, which reduces the cosmic-ray muon flux by approximately a factor of one million compared to the Earth's surface. Figure 4.3 illustrates a comparison between the background spectra of HPGe detector obtained above the ground and at LNGS, using two distinct methods of passive shielding.

The LUNA 400-kV accelerator delivers proton and alpha-particle beams with an intensity of up to 500 μA on the target. Precise control of beam energy stability is crucial in nuclear astrophysics studies, as the fusion cross section below the Coulomb barrier exhibits exponential dependence on the energy. The LUNA proton beam energy is calibrated with an accuracy of 0.3 keV and has a long-term stability of 5 eV per hour. The beam energy spread has been estimated at 100 eV [FIJ$^+$03]. LUNA offers two beam lines: one is fitted with a solid-target arrangement, while the other has a windowless gas target.

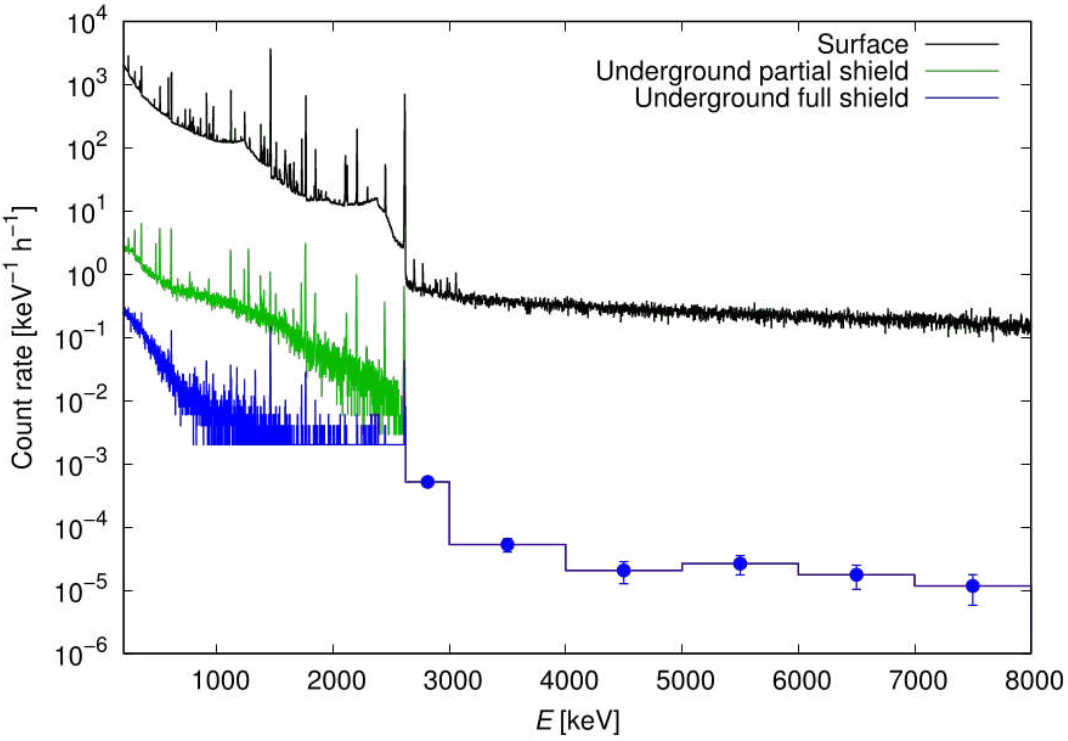

Figure 4.3. Environmental background spectra measured with an HPGe detector positioned at the Earth's surface, at LUNA with full passive shielding (4 cm thick copper, 25 cm thick lead and a radon box [8] and at LUNA with a partial passive shield (4 cm thick copper and 25 cm thick lead) designed to host a second HPGe detector [32]. Above 2600 keV, the backgrounds in the two shielded configurations coincide. [Dep19]

4.1.2 Accelerator: LUNA 400kV

LUNA 400kV is a high-voltage accelerator with a capacity of 400 kilovolts, situated at the Gran Sasso Laboratory (LNGS). This accelerator is referred to as LUNA II, which was commissioned in 2001. LUNA II is designed to determine the cross section, $\sigma(E)$, of nuclear reactions induced by charged particles that are of astrophysical importance (such as hydrogen burning in the sun). These reactions take place at energies significantly lower than the corresponding Coulomb barrier and hence LUNA II is aimed to do measurements at energies potentially near or within the associated Gamow energy E_G. The focus of our experiment is to perform the ^{16}O(p,γ)^{17}F reaction, which serves as the entrance channel for the nitrogen-oxygen (NO) branch of the CNO-cycle.

Fig. 4.2 shows the real-life picture of the LUNA control room. Given the signif-

Figure 4.4. The LUNA 400 kV accelerator tank

icant decrease in $\sigma(E)$ as energy E decreases, it is crucial to have precise knowledge of the absolute incident energy E. For the above reaction, a deviation of 3 keV in the beam energy at 100 keV (equivalent to a 3% uncertainty) results in a huge 40% error in $\sigma(E)$. In order to provide accurate measurements, it is crucial to have a thorough understanding of both the absolute energy spread and the long-term energy stability. In our experiment, the latter is especially significant due to the extended duration of operation, lasting several days, at low energies.

Luna II comprises of a 400 kV electrostatic accelerator (High Voltage Engineering Europe, Netherlands) imbedded in a tank [FIJ+03]. Fig. 4.4 shows the LUNA 400 kV accelerator tank. The tank is filled with a gas mixture N_2/CO_2 at 20 bar. An Inline-Cockcroft-Walton power supply is located inside the tank to generate the high voltage (HV). DC input of the accelerator is provided by a low-ripple power supply rating at maximum 300 V and 10 A. The HV at the ion source, i.e. at the terminal is filtered by a stabilization system consisting of a RC-filter located at the output of the HV power supply and an active feedback loop based on a chain of

resistors which measure the HV at the terminal. The resistors have a temperature coefficient of $\leq 10 ppm/^{\circ}C$ and the accuracy of 0.1%. For frequencies larger than 1 Hz the system reduces the HV-ripple to 30 Vpp; the ripple is monitored with a pick-up plate [FIJ+03]. It is anticipated that the system has a reproducibility and long-term stability of the HV of 20 Vpp at 400 kV over several days, which is consistent with the observations done so far. The ion beams of 1 mA hydrogen (75% H^+) and 500 μA He^+ are provided by the radio-frequency ion source, with good stability over a continuous operating time of about 40 days on the accelerator tube. An electrode, which is part of the accelerator tube, extracts the ions. The voltage of the electrode is thus included in the overall HV at the terminal. The accelerator tube also have an adjustable shortening rod and a magnetic X-ray suppression system. There is 5 mm thick Pb shield around the tank. The shield lowers the radiation level in the control room below $0.5 mSv/h$ for the above ion beams at 400 kV [FIJ+03]. The ion beam is guided and focused accurately to the target station with a 45° magnet (30 cm radius, 3 cm gap, 1.6 MeV amu; 1×10^{-4} stability/h) and a vertical steerer located before the magnet. The proton beam current on target is typically 500 μA with a half-angle divergence of 0.3°, in the energy range of 150–400 keV. At 50 keV the proton current is about 150 μA. A PLC-based computer controls the accelerator, the experimental equipment, and the data acquisition [FIJ+03]. This automated control system enables safe and uninterrupted operation over long periods without the need for a continuous on-site operator.

4.1.3 Shielding (underground+lead)

An effective shielding has been designed for the solid target setup at LUNA to minimise the environmental background substantially during the experiment [Axe18]. This shielding is compatible with both the $CeBr_3$ and HPGe detectors used on this beam line. The $CeBr_3$ detector can be positioned within the shielding, while the HPGe detector can be installed either at a 0° angle (directly facing the source) or at a 55° angle (to minimise the impact of unknown angular distributions, as the Legendre polynomial P_2 becomes zero at this angle) relative to the beam axis. The configuration of the shielding for both detectors is depicted in figure 4.5. The lead shielding has a thickness of 10 cm. An essential aspect of this shielding arrangement is the convenient accessibility to the target, which is accomplished by placing the lead shielding on movable tracks, allowing for effortless separation of the upstream and downstream sections. This is particularly beneficial in solid target experiments where the targets need to be often replaced. The supplementary lead component positioned at an angle of 55° is also mounted on rails and can be retracted from the target, together with the attached detector.

Different background measurements achieved with this shielding are shown in

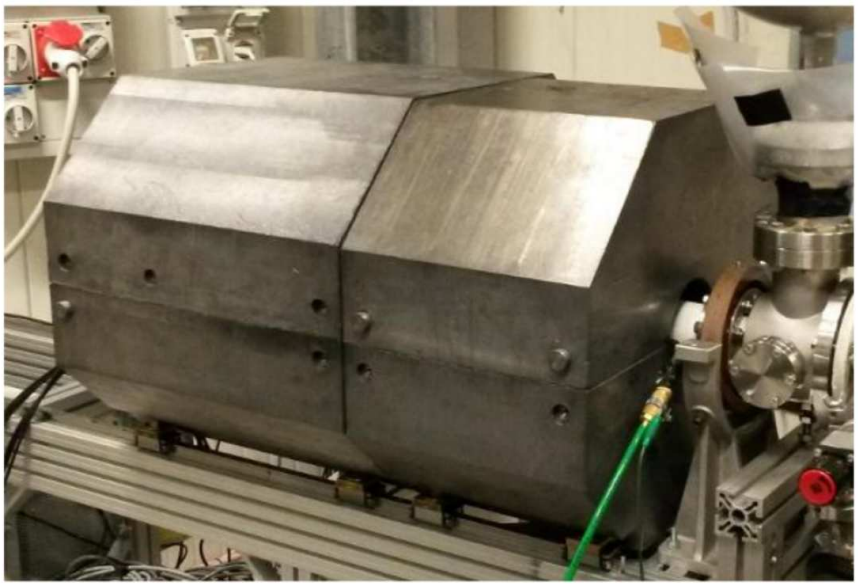

Figure 4.5. The lead shielding around the detectors

figure 4.6. The plot represents a measurement on surface, the unshielded detector underground, and the detector in the new shielding [Axe18]. The background peaks are mostly caused by long-lived radioactive nuclides or their decay chains, as shown in Figure 4.6. A continuous background induced by cosmic radiation can be visible on the surface at energies exceeding the highest gamma ray lines from natural radioactivity, which motivates a detector to be established underground where the cosmic ray background is significantly decreased. Underground data show a three-fold reduction in background from cosmic rays above 3.3 MeV, compared to surface measurements. Environmental gamma ray backgrounds are influenced by radionuclide content in the environment, such as uranium or thorium in rock or radon in air, rather than location depth. These background rates may fluctuate due to environmental variables such air radon concentration, which depends on ventilation. The lead shielding has been proved effective in the reduction of environmental backgrounds.

4.1.4 Detectors

Various gamma-ray detection methods are utilised in experimental nuclear physics, based on the particular requirements of each experiment and the nuclear characteristics being studied. In order to characterise the angular distribution of the $^{16}O(p,\gamma)^{17}F$ reaction at LUNA, two distinct detectors with complimentary characteristics have been employed: a high-resolution HPGe detector with low efficiency,

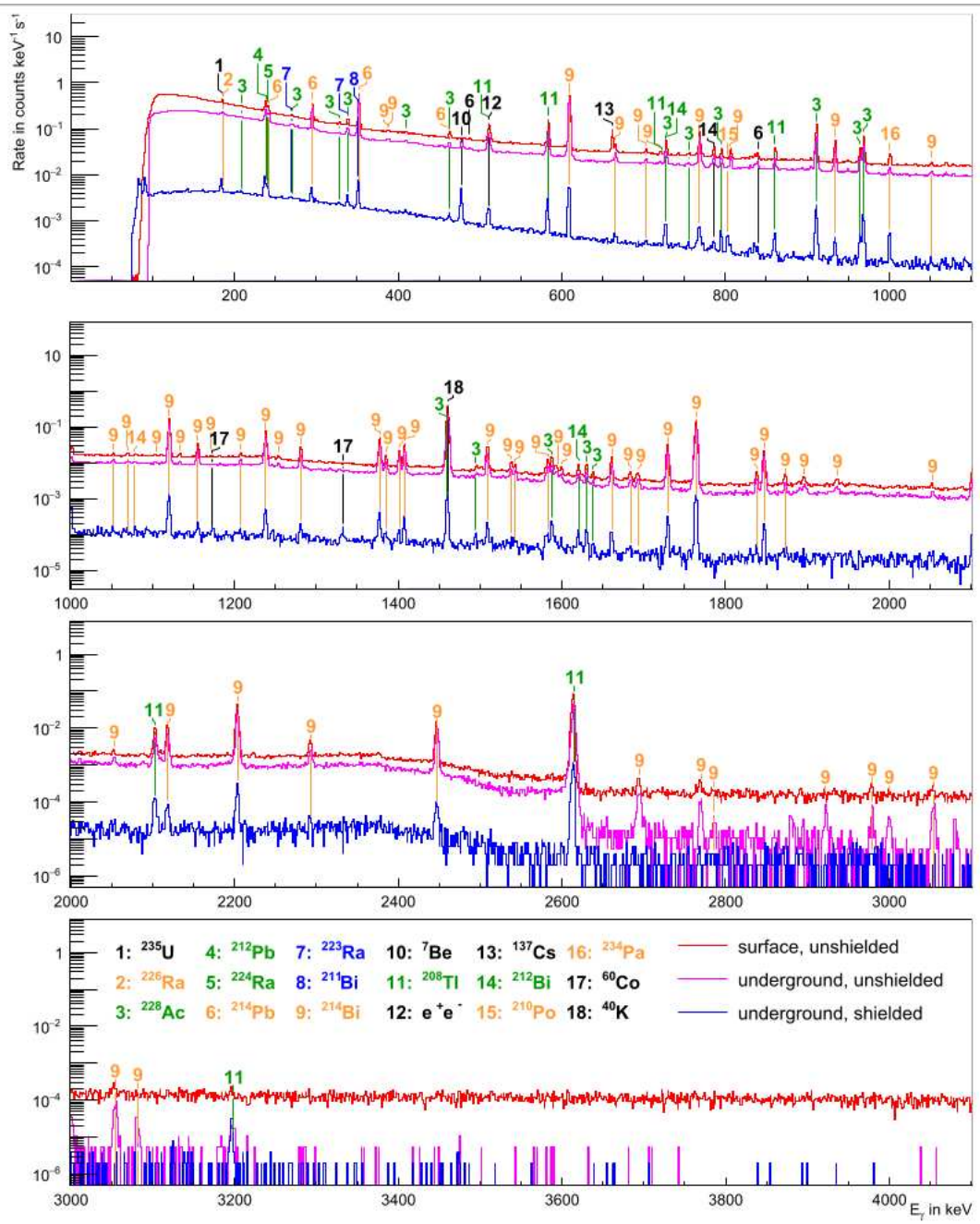

Figure 4.6. Background spectra acquired with the same HPGe detector: unshielded on surface, unshielded underground, and fully shielded underground. The colours of the nuclides correspond to the decay chain they belong to. [Axe18]

and a high-efficiency $CeBr_3$ scintillator with comparatively lower resolution. Below, the two detectors that provide different methods for measuring the gamma radiation signal of the $^{16}O(p,\gamma)^{17}F$ reaction have been summarised.

Cerium Bromide ($CeBr_3$) In nuclear astrophysics scintillation spectrometers are widely used in detection and spectroscopy of X-rays and γ-rays at room temperature. The scintillation crystals are required to possess some specific characteristics such as high light output, high stopping efficiency, fast response, good proportionality, low cost and availability in large volume.

Cerium Bromide ($CeBr_3$) is a new scintillator for γ-ray spectroscopy. It possess exceptional light-yields, fast response, and high-density characteristics. The material's main benefit, in comparison to other high-resolution scintillators, is in its remarkably low intrinsic background noise. $CeBr_3$ exhibits high speed performance without any sluggish components. The scintillators possess hygroscopic properties and can be obtained from BNC in an encapsulated form, with an entrance window that is directly connected to a light sensor, such as a PMT or SiPM. Alternatively, they can be acquired as fully integrated detector assemblies, complete with a light sensor and front-end electronics. Currently, there are available sizes that range from pixel dimensions for arrays to volumes as large as 102 mm (4 in) in diameter and 152 mm (6 in) in length [BNC23]. Two 2" $\times$ 2" $CeBr_3$ detectors have been used in our experiment.

$CeBr_3$ has distinguished property of relatively high-density and exhibit proportional response to gamma rays. The material provides good energy resolution as a scintillator, typically 4% FWHM for 662 keV photons (^{137}Cs source) at room temperature. $CeBr_3$ has fast light pulse rise time. The detector can provide subnanosecond time resolutions. $CeBr_3$ has a background count as low as $<$0.002 c/s/cc in the Ac-227 complex (1500 to 2200 keV) [BNC23]. Thus, the detector presents an exclusive advantage over other high-resolution scintillators which suffer from this or other intrinsic activity. As such, two $CeBr_3$ detectors has been employed to perform the γ-ray angular distribution.

GeBochum (HPGe) HPGe detectors have high energy resolution, such as 2.2 keV at a gamma-ray energy of 1.33 MeV, resulting in a relative energy resolution of less than 0.2% [Axe18]. The size of the germanium crystal and the source's distance from the detector determine an HPGe detector's full energy peak efficiency. It is commonly compared to a 3" $\times$ 3" NaI(Tl) scintillation detector at 1.33 MeV, placed at a distance of 25 cm. This specific setup is considered to have 100% relative efficiency. Due to germanium's small crystal volume and the comparatively low interaction probability of gamma rays, achievable absolute full energy detection efficiencies are typically in the range of a few percent for 1 MeV gamma rays. The

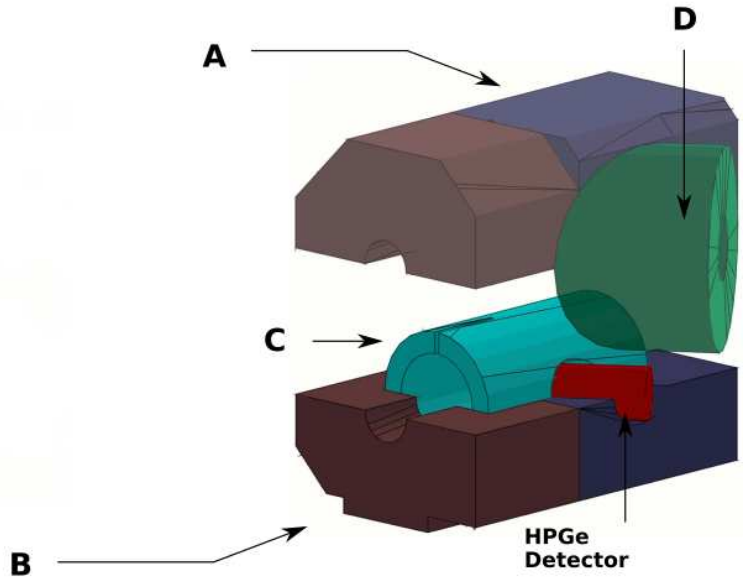

Figure 4.7. 3D diagram of a HPGe Detector [Axe18]

efficiency drops rapidly as the energy of gamma rays increases. HPGe detectors enable the precise determination of specific gamma-ray energies, which can be linked to the nuclear reactions being investigated or to background sources, even with limited prior understanding of possible influences.

We employ a coaxial HPGe detector (ORTEC GEM-120225-P-ST) with a relative efficiency of 120% for our experiment configuration. The Germanium crystal has the diameter of 84.6 mm with the length of 87.8 mm. The End Cap to Crystal is 4 mm . The detector has the absorbing layers of 1.00 mm aluminum with 700 μm of inactive germanium.

Fig. 4.7 shows the modular lead shielding for the HPGe detector at 55°. In the picture the top part is lifted to demonstrate the inner region of the shielding. On the front left sides of the picture, the beam line enters through the openings. Beam line and target are shown here. The detector rests in the downstream part of the shielding, and can be retracted with this part of the shielding (A) to access the target, while the upstream part of the shielding (B) stays in place. An additional cylindrical lead inset (C) and a block of lead (D) around the detector are used in this HPGe detector configuration (shown at 55°) [Axe18].

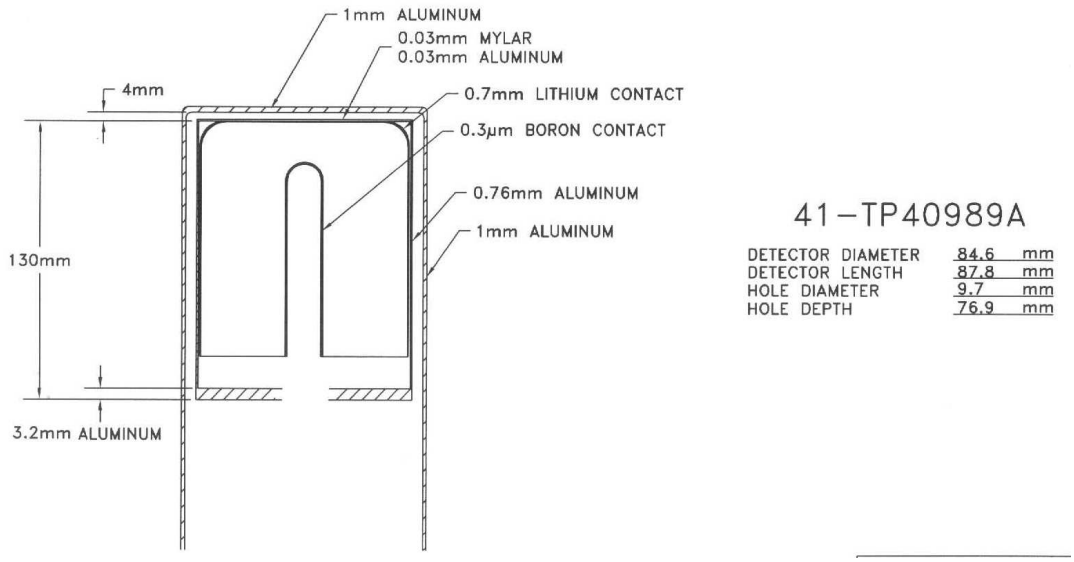

Figure 4.8. Schematic diagram of a HPGe (High-Purity Germanium) Coaxial Detector System [ORT02]

4.1.5 Target: Solid Ta_2O_5

Solid targets of known thickness, isotopic composition, and stoichiometry are a crucial part for nuclear astrophysics studies of proton-induced reactions at astrophysical energies. For the study of the γ-ray angular distribution of the $^{16}O(p,\gamma)^{17}F$ reaction at LUNA II, solid Ta_2O_5 targets that are able to withstand high beam currents for extended periods of time have been used. The targets ensured the following requirements [SBK+87]: Firstly, the target must have suitable and stable thickness, so that it can sustain high beam currents (such as several hundreds of μA) over long duration (from several hours up to a few days); secondly, the stoichiometry of the target must be known and constant in order to allow accurate calculations of beam energy-loss; additionally, the isotopic composition of the target have to be well-known, allowing measurable yields. For measuring reaction yields and thus the cross-section, each of these features of the target must be measured with high accuracy. Since changes in thickness, stoichiometry and/or composition under beam irradiation directly affect the measured absolute cross sections [RR88] [Ili15], the target properties must be monitored with utter caution.

In this section, an overview on the production and characterisation of Ta_2O_5 targets for the study of proton-induced reactions at the LUNA has been presented [Cac12]. The targets were prepared by anodic oxidation of tantalum backings

in distilled water. To reduce the existence of any impurities that might cause undesired background reactions with the beam in the energy region of astrophysical interest, considerable measure was taken. Targets of various thicknesses (1200-5800 Å) and composition were produced following a standard procedure as depicted in fig. 4.9, a technique known to produce targets with highly uniform stoichiometry and homogeneous thicknesses [Phi74].

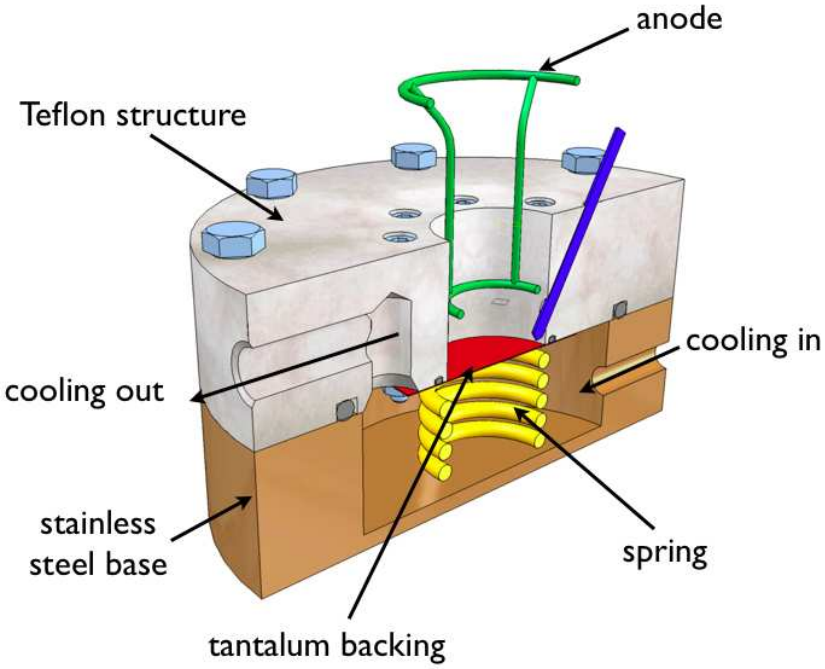

Figure 4.9. Illustration of the anodisation device manufacturing Target Ta_2O_5 [Cac12]

From 0.3 mm thick Ta sheets (99.9% nominal purity) Tantalum disks (40 mm diameter) were obtained. At first the disks were polished by dipping the specimens in a 5:2:2 solution of H_2SO_4 , HNO_3 and HF. Further contamination removal was done by etching the tantalum backings in a bath of 20% citric acid solution in water for 1h at 90° C. Then the tantalum disks were put in the anodising apparatus. The device consists of a cylindrical annulus of teflon (100 mm outer diameter and 25 mm inner diameter with 25 mm height) fixed on a cylindrical base of stainless steel, as shown in fig. 4.9. For good thermal stability and as an effective electrical insulation the teflon was used. The effective volume of the anodising cell where the electrolytic solution will be placed is defined by the cavity in the teflon. At the interface between the teflon and the stainless steel base a tantalum disk is placed. To make Tantalum disk acts as the cathode it was maintained at ground potential through contact with a metallic spring. The electrolyte consisted of a 0.1

mol potassium iodide (KI) salt solution with distilled water. A basket (90% gold and 10% nickel) of 2 cm diameter is inserted in the hole. This gold-nickel "basket" is the anode of the anodisation process. The vertical position of the basket can be appropriately adjusted, maintaining co-axial symmetry with the cathode, to reach the surface of the electrolyte. This helped reduce the formation of bubbles within the electrolyte, resulting in a more homogeneous deposition growths. A stabilised DC power supply was connected to the anode with a ramp so that the DC power supply can move up and down in order to keep the current inside the electrolyte solution constant. There is a cooling system to avoid evaporation of the solution during the anodisation process. A fluid as coolant is kept at constant temperature, circulating inside the device [Cac12].

The target thickness degrades linearly as a function of the total accumulated charge. The degradation was measured using Nuclear Resonant Reaction Analysis (NRRA) and found to occur typically at a rate of 0.2 keV/C. The stoichiometry of the target was investigated by means of Rutherford Backscattering (RBS) technique while the isotopic compositions were examined using Secondary Ion Mass Spectrometry (SIMS) techniques. Any alteration of these properties during beam bombardment has been assessed both in regions of the targets exposed to the beam as well as in regions where beam exposure was negligible. Neither the stoichiometry not the relative isotopic abundances in depth showed any appreciable change throughout the proton-induced reaction measurements carried out at LUNA.

Fig. 4.9 shows the schematic diagram of the anodisation device producing Ta_2O_5 target [Cac12].

5 Data Analysis:

The objective of the master thesis is to study the angular distribution of the emitted γ-ray from $^{16}O(p,\gamma)^{17}F$ reaction. In particular, the aim is to find the proper parameters to fit the angular distribution. During the master thesis, I have analysed the data of γ-rays detected by the detectors recorded with LUNA400 establishment. For that purpose, the CERN Root data analysis software framework was extensively used [ROO23]. To realize the angular distribution measurement, the steps followed during the master thesis are the following:

Step-1: Realize the detector calibration (using radioactive source).

Step-2: Find the efficiency of the detectors using proper fitting function.

Step-3: Calibrate the runs obtained during the $^{16}O(p,\gamma)^{17}F$ reaction.

Step-4: Identification of the γ-ray peaks in the spectrum from $^{16}O(p,\gamma)^{17}F$ reaction.

Step-5: Adjustment of ROIs (Region Of Interest) to perform peak area calculation.

Step-6: Measure the number of counts in each detector as function of beam energy.

Step-7: Perform yield calculation.

Step-8: Plot yields as function of the detector angle for each runs.

Step-9: Perform fit to obtain the relevant parameters for the γ-ray angular distribution.

Step-10: Comparing plots among runs with same beam energy.

All these steps of data analysis will be detailed in the next sections. It has to be noted that, despite the efforts made in background reduction the gamma lines produced by the reaction of interest were very low in statistics in the gamma spectrum due to the beam induced background on other contaminants on the targets and setup and very close to other intense gamma lines, such as 511 keV. This limited the possibility of the analysis and the results. Despite this a clear impact on the angular distribution correction to be used in the cross section analysis has been obtained and will be implemented in a work which is beyond the scope of the present thesis.

5.1 Detector Calibration

To determine the energy calibration and efficiency of the detector setups, three radioactive sources: ^{137}Cs, ^{60}Co and ^{133}Ba were used. The main properties of the radioactive calibration sources are listed in Table 5.1. The sources were chosen to calibrate the γ-ray detector over the energy of interest for the $^{16}O(p,\gamma)^{17}F$ reaction.

Nuclide	Gamma Energy (keV)	Gamma Intensity (%)	Ref
^{137}Cs	661.657 (3)	85.10 (20)	[EB07]
^{60}Co	1173.228 (3)	99.85 (3)	[EB13]
	1332.492 (4)	99.9826 (6)	
^{133}Ba	276.3989 (12)	6.0 (6.7)	[NG68]
	302.8508 (5)	15.3 (1.7)	
	356.0129 (7)	51 (5.7)	
	383.8485 (12)	7.3 (8.2)	

Table 5.1: List of the radioactive sources and their emitted γ-rays used for the calibration measurement.

In present work three detectors were used and three different calibration curves had to be determined. Linear fits (Fig. 5.1) were performed in order to determine the relationship between γ-ray energy and spectrum channel number, and results are the following:

$$E_\gamma = m \times Channel + q \tag{5.1}$$

The obtained fit parameters are given in Tab. 5.2.

Detector	m (slope)	q (intersection)
$CeBr_3$ at 0°	0.67812	4.480495
$CeBr_3$ at 90°	0.448595	13.5577
HPGe at 55°	0.677603	-0.3647

Table 5.2: Fit parameters for calibration of the three detectors.

To test the calibration it was applied to ^{133}Ba spectra and peaks were identified within 250 keV to 400 keV.

The radioactive source data were also used to determine the detectors' efficiency, as discussed in the next section.

5.2 Detector Efficiency

The detection efficiency, crucial for both the angular distribution and the cross section calculation, of the experimental setup was determined by using the calibration sources, ^{137}Cs, ^{60}Co, ^{133}Ba, available at LNGS. As for the energy calibration these sources allows to cover the whole energy range of interest for the ^{16}O(p,γ)^{17}F. The main characteristics of each source are summarized in table 5.3. The calibrated radioactive sources were placed at the location of the target to reproduce the experimental configuration as during the ^{16}O(p,γ)^{17}F reaction measurement.

Source	**Half-life $T_{1/2}$ (y)**	**Initial Activity A_0 (kBq)**	**Ref. Date dd/mm/yy**	**Exp. Date dd/mm/yy**	**Activity A (Bq)**
^{137}Cs	$1.100(9)\times10^4$	6.46 ± 0.07 [Bun16a]	01/07/2016	07/03/2023	5539.733 ± 60.41
^{60}Co	1925.3(4)	9.01 ± 0.07 [Bun16b]	01/07/2016	07/03/2023	3743.002 ± 29.09
^{133}Ba	10.551 (11)	43.1 (3) [Gmb13]	01/07/2013	07/03/2023	34614.411 ± 1038.43

Table 5.3: List of the radioactive sources and their Half-life and Activity used for the efficiency measurement.

For the efficiency measurement two approaches are used commonly in experimental nuclear astrophysics: a multi parametric fit of the experimental data and GEANT4 simulation. In the present work the multi parametric fit of the experimental data has been adopted.

The experimental full-energy efficiency is obtained as the ratio between the measured peak area and the number of γ-rays of interest emitted in the whole solid angle:

$$\epsilon(E) = \frac{N(E)}{A \cdot t \cdot Br} \tag{5.2}$$

where $N(E)$ is the number of net counts in the γ-peak of interest at energy E, A is the activity of the source at the time of experiment, t is the acquisition time and Br is the branching ratio of the emitted γ-ray.

To derive the peak area measurement two approaches were used: the so called Gilmore approach [Gil08] and the peak fitting approach. Specifically the ^{137}Cs and ^{60}Co peaks were measured using Gilmore approach [Gil08] while the ^{133}Ba peaks required the peak fitting approach [ROO23]. Both approaches for peak area measurement are summarized below:

Gilmore Approach The measurement of a peak area can be done by summing the number of counts in each of those channels that comprises the peak and subtracting the number of counts which comes from the background beneath the peak. We can estimate the background level by using the channel contents at the upper and lower edges of the peak region. Let L and U denote the beginning and ending channel of the peak region, respectively, (marked with vertical lines in Figure 5.5

and 5.6), then the gross (or integral) area of the peak is expressed as:

$$G = \sum_{i=L}^{U} C_i \tag{5.3}$$

where C_i are the counts in the ith channel. The background beneath the peak can be estimated as:

$$B = \frac{n(C_{L-1} + C_{U+1})}{2} \tag{5.4}$$

where n is the number of channels within the peak region while C_{L-1} and C_{U+1} are the counts in the channels immediately before the lower edge channel L and after the upper edge channel U, respectively. Mathematically, this background is the area of the trapezium beneath the peak, which can be considered as the mean background count per channel beneath the peak, multiplied by the number of channels within the peak region. Then the net Peak Area is:

$$A = G - B = \sum_{i=L}^{U} C_i - \frac{n(C_{L-1} + C_{U+1})}{2} \tag{5.5}$$

To make the background estimates more precise i.e. less uncertain, instead of using only one channel on each side, m number of channels beyond each side of the peak region are used to estimate the background beneath the peak. Then the formula to measure net Peak area becomes:

$$A = \sum_{i=L}^{U} C_i - \frac{n(\sum_{i=L-m}^{L-1} C_i + \sum_{i=U+1}^{U+m} C_i)}{2m} \tag{5.6}$$

Consequently, the uncertainty in the net peak area is given by:

$$\sigma_A = \sqrt{[A + B(1 + \frac{n}{2m})]} \tag{5.7}$$

We can also choose different number of channel m and n beyond each side of the peak region for the background estimation based on the requirement of the spectra under study. Then the formula for net peak area (Eq. 5.6) as well its error calculation (Eq. 5.7) becomes:

$$A = \sum_{i=L}^{U} C_i - \frac{n(\sum_{i=L-m}^{L-1} C_i + \sum_{i=U+1}^{U+m} C_i)}{m+n} \tag{5.8}$$

and

Detectors	a_0	a_1	a_2
$CeBr_3$ at 0°	0.870 ± 0.07	-0.695 ± 0.01	-0.013 ± 0.001
$CeBr_3$ at 90°	-2.309 ± 0.08	-0.013 ± 0.02	-0.054 ± 0.001
HPGe at 55°	-2.384 ± 0.07	-0.25 ± 0.01	-0.014 ± 0.001

Table 5.4: Fitting parameters for the efficiency curve measured with radioactive sources.

$$\sigma_A = \sqrt{[A + B(1 + \frac{n}{m+n})]} \tag{5.9}$$

The method stated above assumes that the background is linear from the bottom to the top edge of the peak, which is quite reasonable as can be seen from the ^{137}Cs spectrum 5.5 and ^{60}Co spectrum 5.6. Therefore, formula 5.8 and 5.9 have been applied to measure the net Peak Area for ^{137}Cs and ^{60}Co spectra.

This method is not applicable where the peaks are not well-separated, which is clearly the case of ^{133}Ba spectrum by the $CeBr_3$ detectors (Fig. 5.7a and 5.7b). The four ^{133}Ba peaks in our energy range of interest are, indeed, overlapped. Hence the peaks were fitted with a dedicated function to calculate the peak area for the radioactive source ^{133}Ba. Specifically the peaks were fitted using gaussians on top of a linear background.

Once the net counts N for all γ-rays of interest and for each detector were derived, the efficiency was calculated using Eq.5.2. The obtained values for the efficiency as function of the γ-ray energy have been fitted with the following:

$$\epsilon(E_\gamma) = \exp\left(a_0 + a_1 log(E_\gamma) + a_2 [log(E_\gamma)]^2\right) \tag{5.10}$$

where E_γ is the γ-ray energy, ϵ the full energy peak efficiency and a_0 , a_1 and a_3 are coefficients determined by the fitting algorithm. The fitting lines are also shown in each of the Fig. 5.8, 5.9, 5.10. The fit parameters are reported in table 5.4.

The efficiency for the E_γ of the ^{16}O(p,γ)^{17}F reaction are then obtained from the formula 5.10 using the parameters shown in table 5.4.

The obtained efficiency values have been applied to perform the yield measurement in the ^{16}O(p,γ)^{17}F reaction. This is discussed in the next section 5.3.

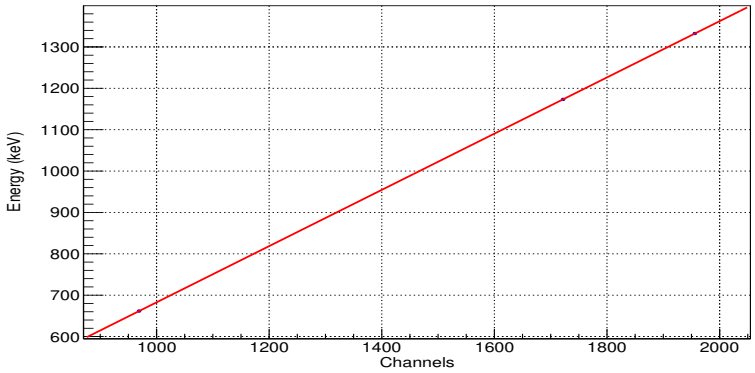

(a) Energy calibration curve of the $CeBr_3$ Detector at 0°

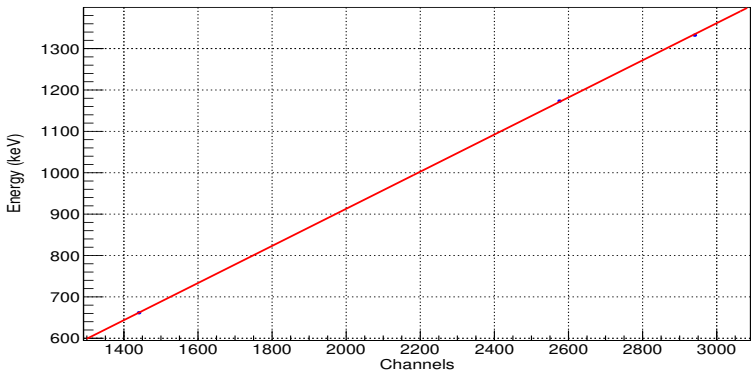

(b) Energy calibration curve of the $CeBr_3$ Detector at 90°

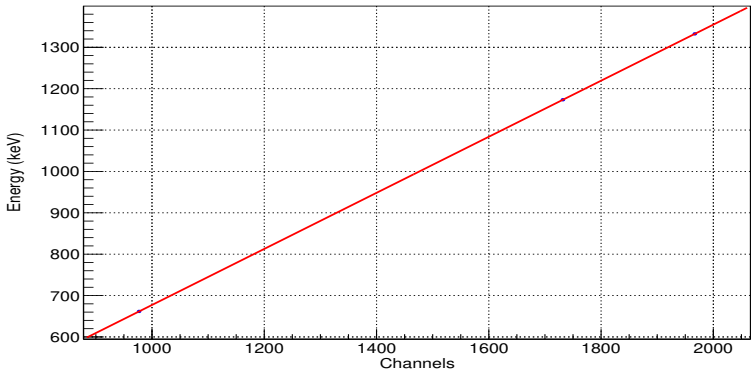

(c) Energy calibration curve of the HPGe Detector at 55°

Figure 5.1. Energy calibration curve obtained using the three reference energy transitions of the radioactive nuclei ^{137}Cs and ^{60}Co. This calibration takes into account the errors on the transition energies, which are too small to be visible in our plot scale. The error values for the different transitions has been defined using the NNDC database [EB07] [EB13]. Any error associated to the channel number is not considered at the moment.

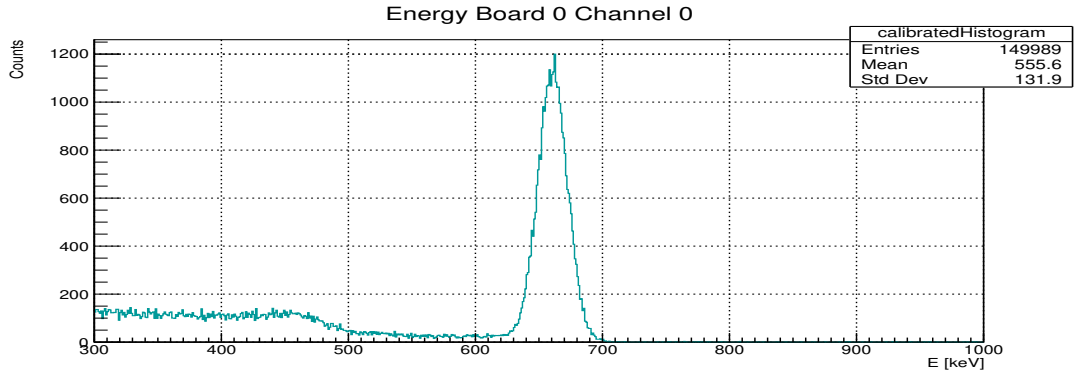

(a) Calibrated spectra, from the detector $CeBr_3$ at 0°, obtained with ^{137}Cs source

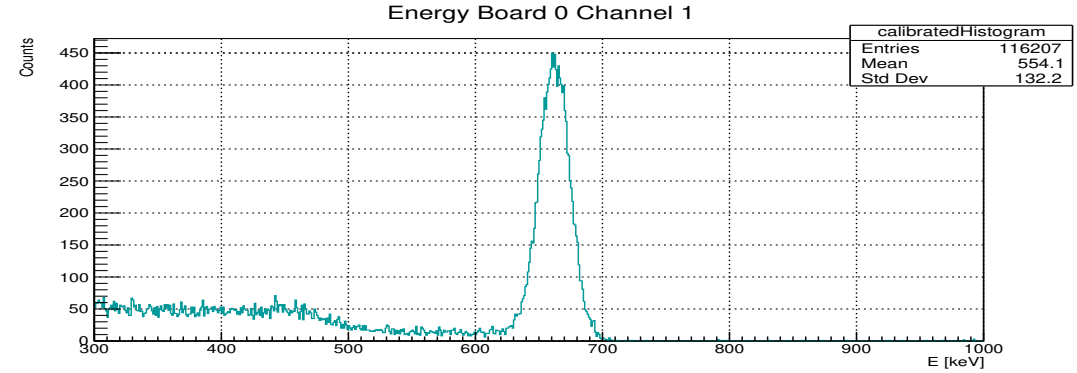

(b) Calibrated spectra, from the detector $CeBr_3$ at 90°, obtained with ^{137}Cs source

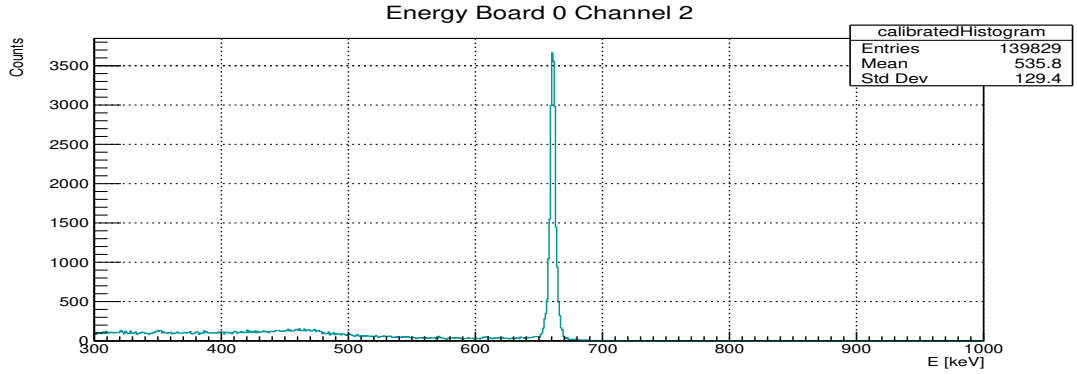

(c) Calibrated spectra, from the detector HPGe at 55°, obtained with ^{137}Cs source

Figure 5.2. Calibrated spectra of ^{137}Cs from the three detectors obtained with radioactive sources, recorded during 645.04 seconds.

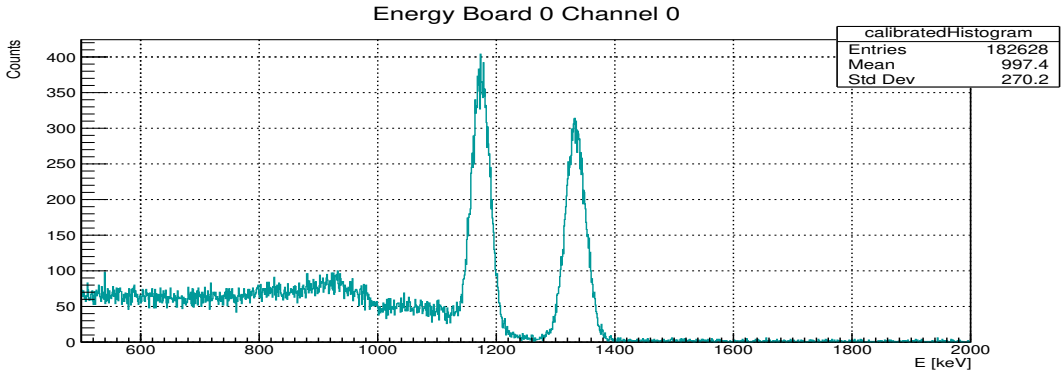

(a) Calibrated spectra, from the detector $CeBr_3$ at 0°, obtained with ^{60}Co source

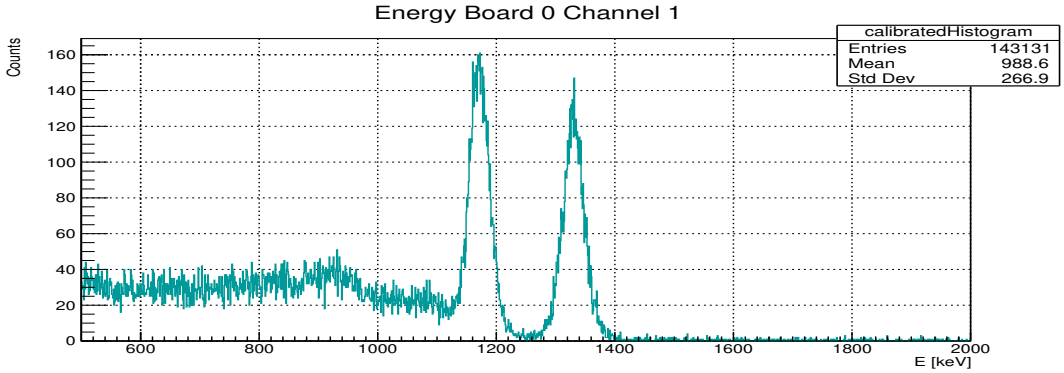

(b) Calibrated spectra, from the detector $CeBr_3$ at 90°, obtained with ^{60}Co source

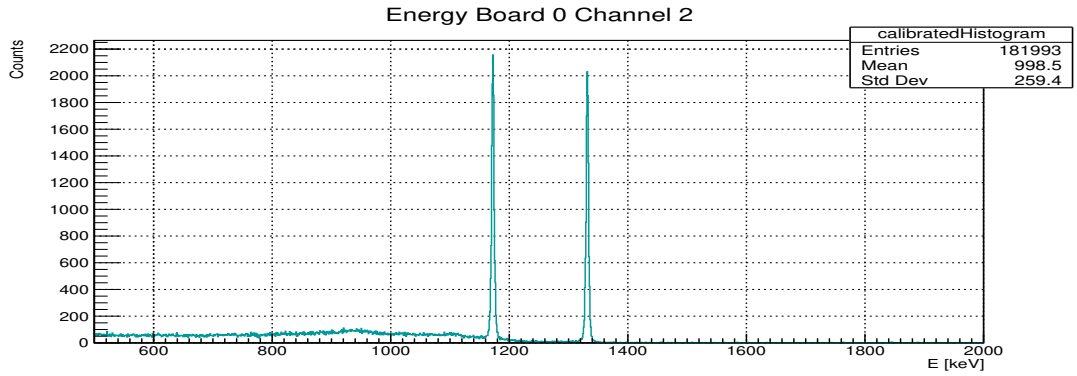

(c) Calibrated spectra, from the detector HPGe at 55°, obtained with ^{60}Co source

Figure 5.3. Calibrated spectra of ^{60}Co from the three detectors obtained with radioactive sources, recorded during 571.71 seconds.

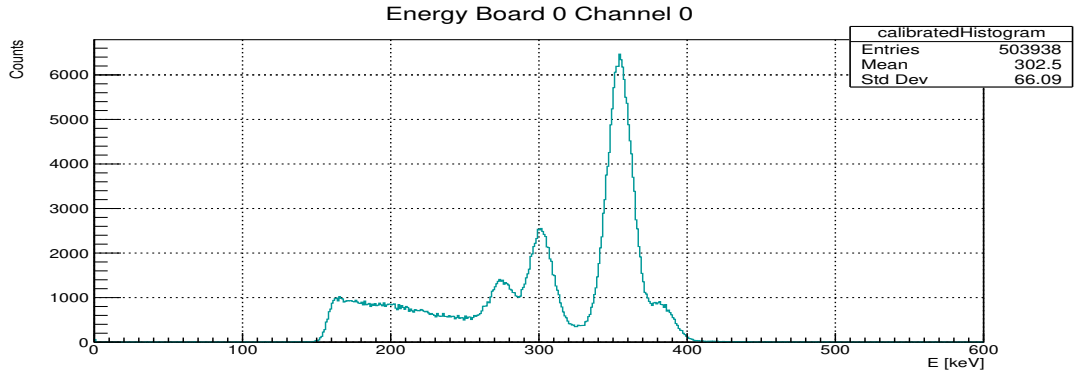

(a) Calibrated spectra, from the detector $CeBr_3$ at 0°, obtained with ^{133}Ba source

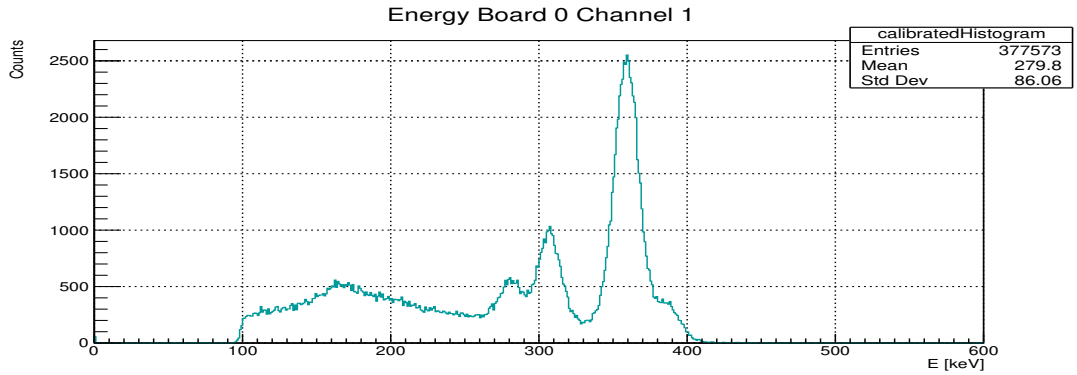

(b) Calibrated spectra, from the detector $CeBr_3$ at 90°, obtained with ^{133}Ba source

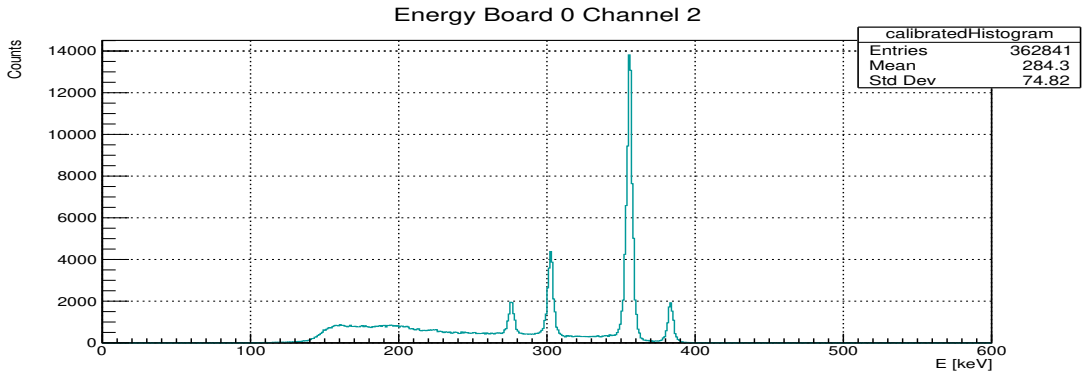

(c) Calibrated spectra, from the detector HPGe at 55°, obtained with ^{133}Ba source

Figure 5.4. Calibrated spectra of ^{133}Ba from the three detectors obtained with radioactive sources, recorded during 580.70 seconds.

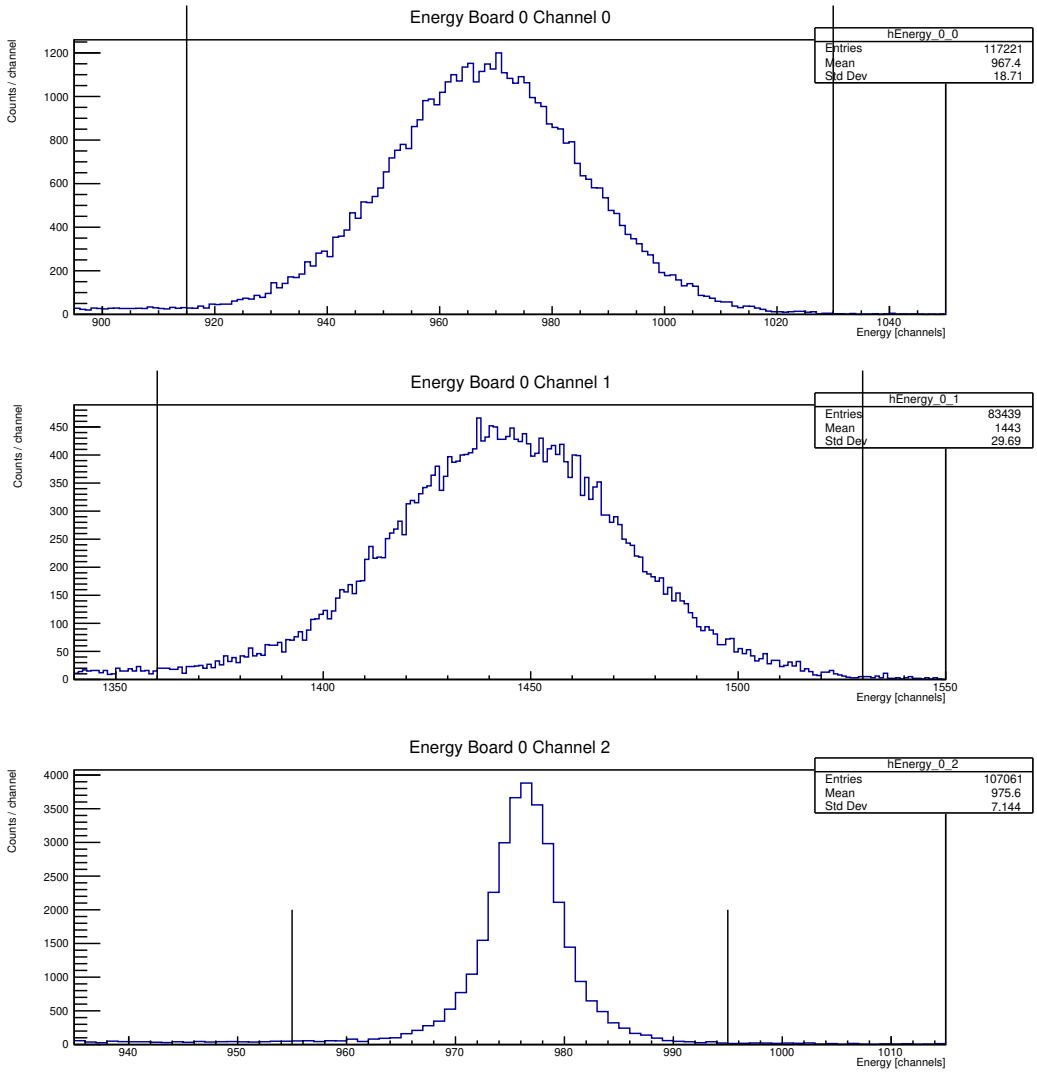

Figure 5.5. The ^{137}Cs peak obtained in three detectors. The vertical lines indicate the ROI considered for the peak area measurement.

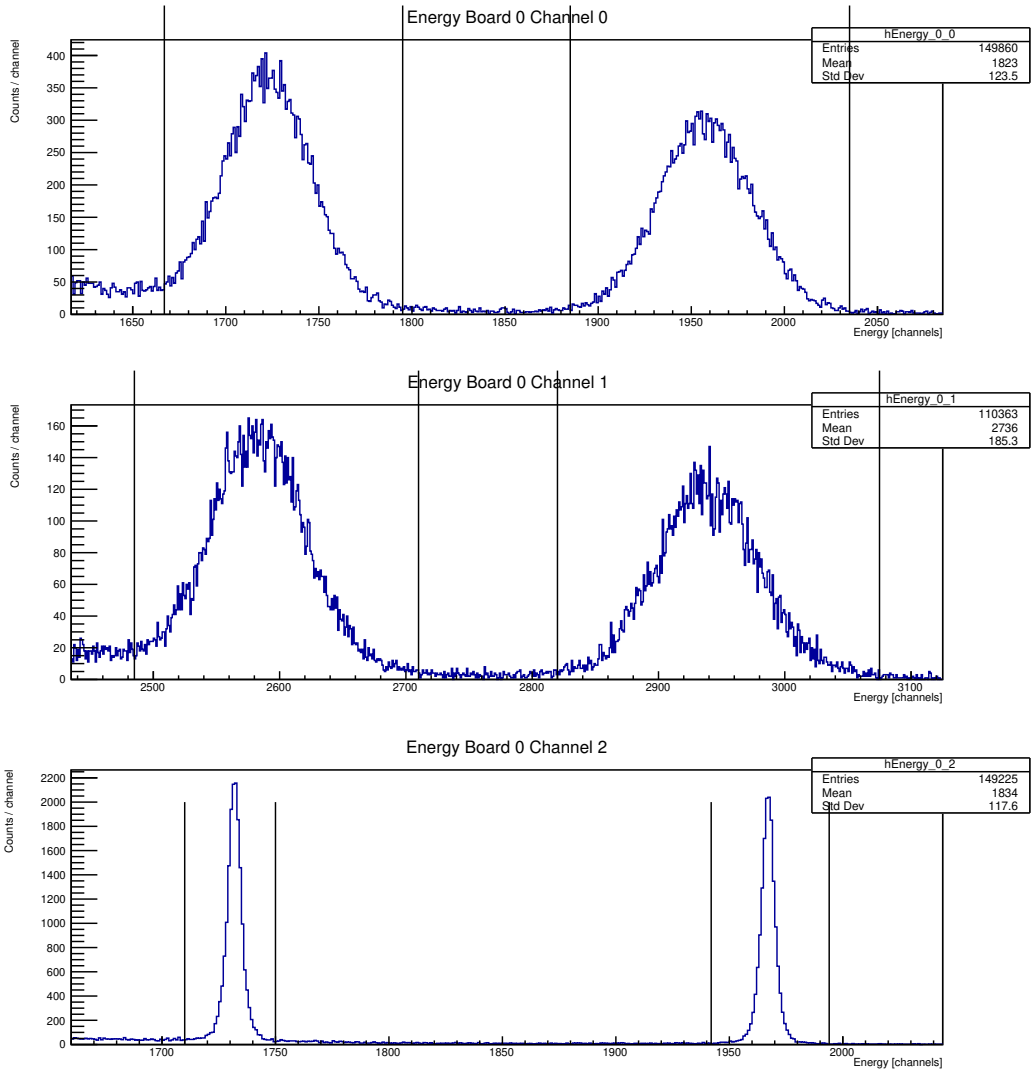

Figure 5.6. The ^{60}Co peak obtained in three detectors. The vertical lines indicate the ROI considered for the peak area measurement.

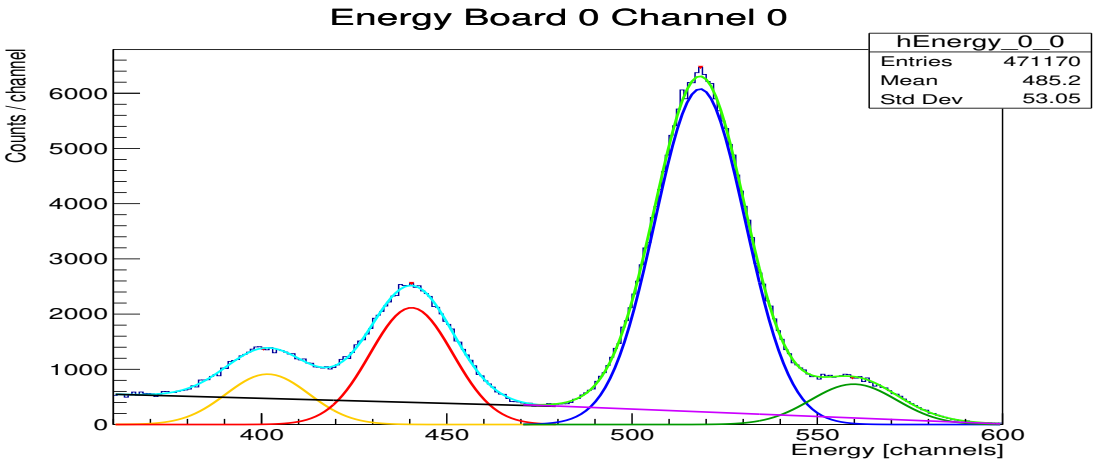

(a) Area Measurement of the ^{133}Ba peak in 1st detector using Fitting [ROO23]

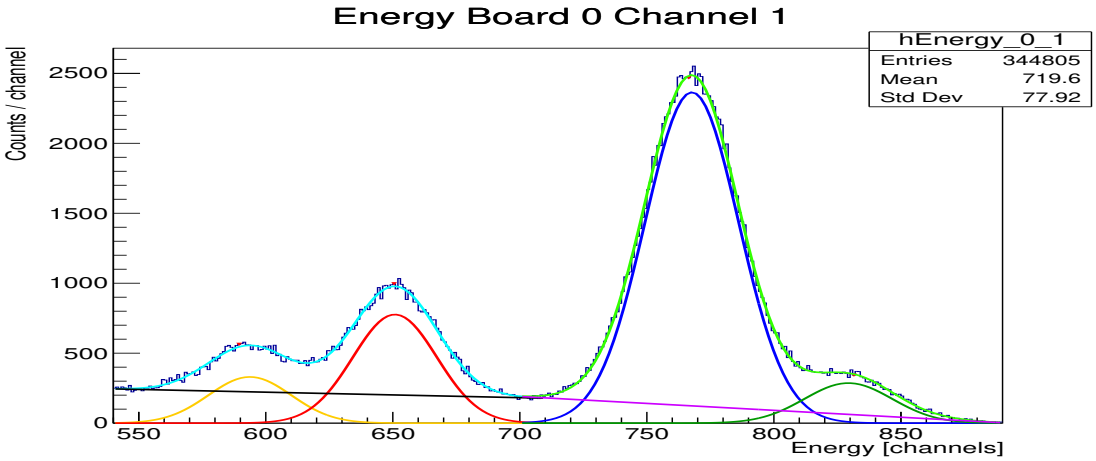

(b) Area Measurement of the ^{133}Ba peak in 2nd detector using Fitting [ROO23]

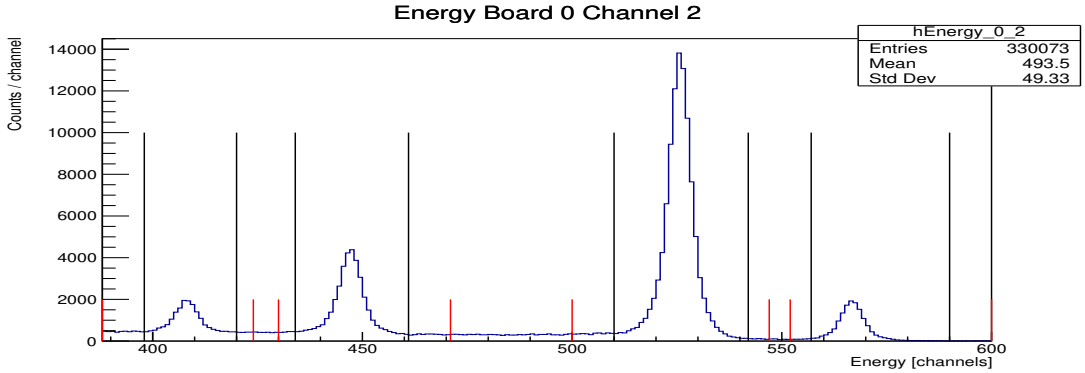

(c) Area Measurement of the ^{133}Ba peak in 3rd detector using Gilmore Approach. The tall black lines defines the peak area region while the small red lines indicate the ROIs considered for background count.

Figure 5.7. Peaks of the Calibrated ^{133}Ba Spectrum.

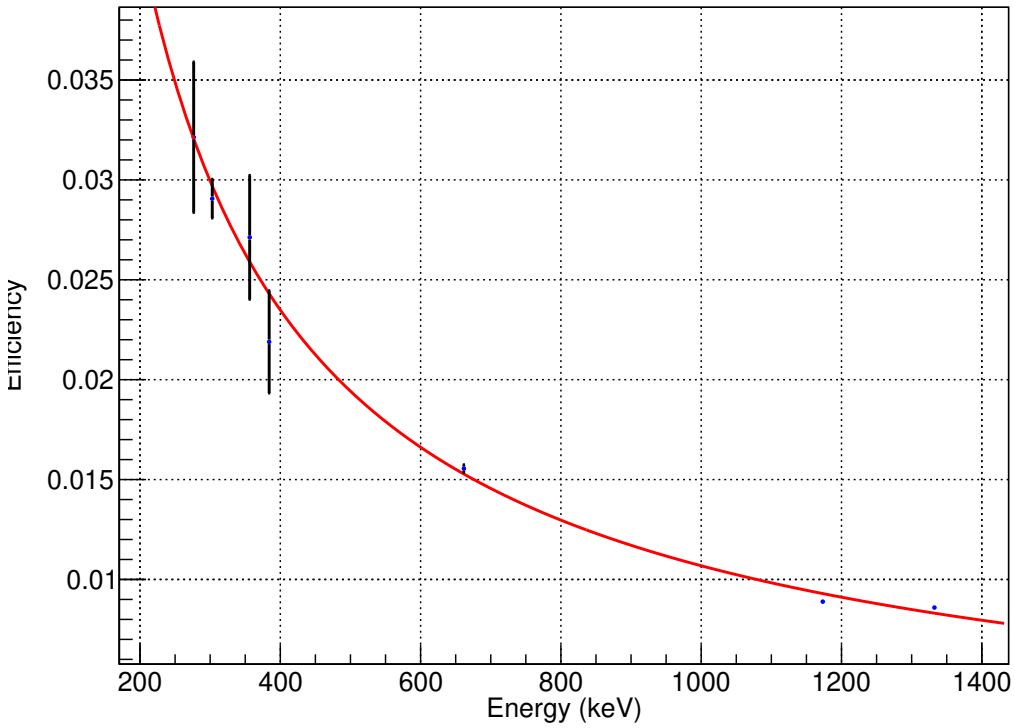

Figure 5.8. Efficiency as a function of the γ-ray energy for the $CeBr_3$ detector at 0°. The fitting function is also shown.

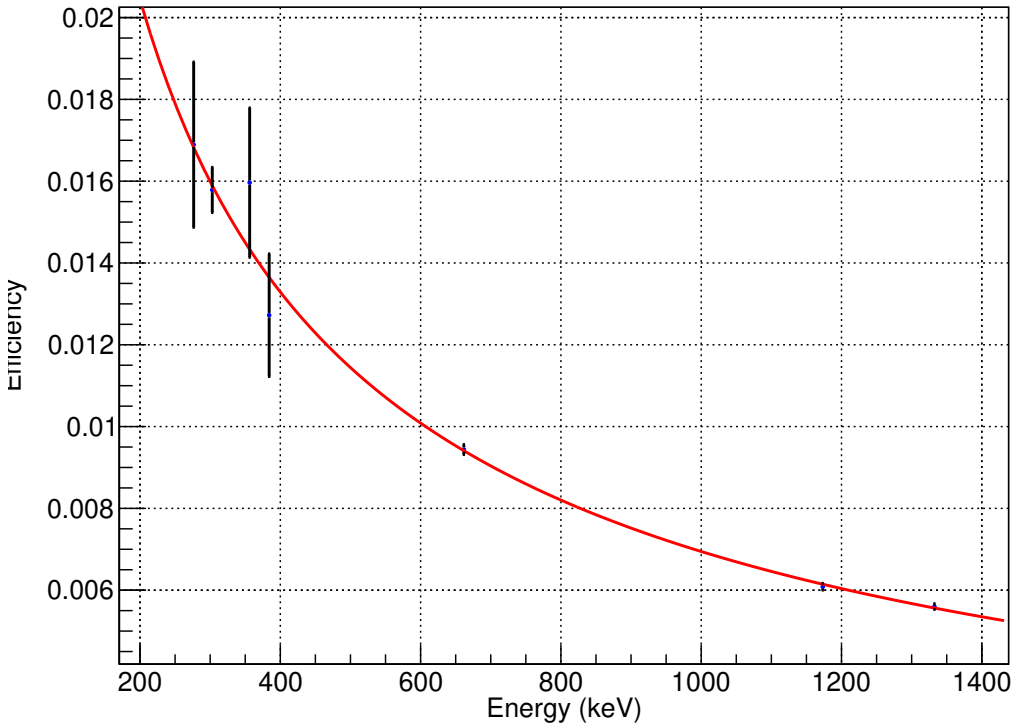

Figure 5.9. Efficiency as a function of the γ-ray energy for the $CeBr_3$ detector at 90°.

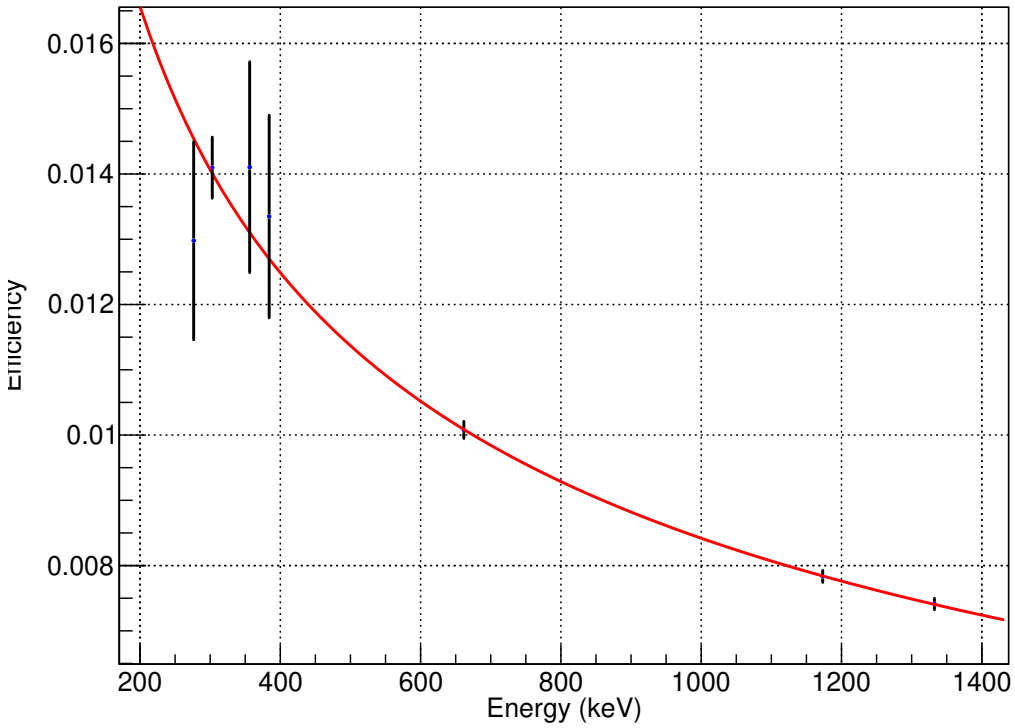

Figure 5.10. Efficiency as a function of the γ-ray energy for the HPGe detector at 55°. The fitting function is also shown.

Beam Energy (keV) (Centre-of-mass)	Transition **DC→1st**	Transition **1st→ground**	Transition **DC→ground**
348.24	453.18	495.33	948.51
375.26	480.2	495.33	975.53

Table 5.5: List of transitions in the ^{16}O(p,γ)^{17}F reaction during each run at two separate beam energy.

5.3 Angular Distribution determination

Because of the low count rate the angular distribution was investigated only at two beam energies, namely 370 keV and 398 keV. For each energy two long runs, each on different target, were acquired to cross check the reproducibility of the results and eventually sum the statistics.

The γ-rays expected for the different transition of the ^{16}O(p,γ)^{17}F reaction at the beam energies investigated are in Tab. 5.5. Particularly, the proton capture to the ground state and first excited state of ^{17}F occurs at

$$E_\gamma = E^{CM} + Q_{value} - \textit{final energy state}$$

transitions

where the incident beam energy has been converted from laboratory frame to center-of-mass frame using the formula

$$E^{CM} = E_p^{lab} \times \mu$$

with $\mu = \frac{m_T}{m_p+m_T}$, reduced mass of the reaction participants. In addition to the above γ-rays a prominent peak is visible at $E_\gamma = 511$ keV.

To obtain the angular distribution the experimental yield:

$$Yield = \frac{\textit{Net Peak Area}}{\textit{(Charge)(Detector Efficiency)(Branching probability)}}, \tag{5.11}$$

should be calculated for each γ-ray as a function of the detector angle per each proton beam. However, due to the poor resolution of the $CeBr_3$ detectors the transition to the first excited state and the de-excitation of the first excited state cannot be distinguish from the 511 keV peak at beam energy 375 keV (at center-of-mass frame). On the other hand, at beam energy 348 keV (at center-of-mass frame) the transition to direct capture to the first excited state is well separated from the other peaks. Finally for both beam energy, the 495 keV peak could not be distinguished from the 511 keV peak.

The HPGe detector has high resolution, as such all peaks were clearly visible in all the runs with both the beam energy.

For the measurement of the net peak area for the Direct Capture Transitions, entering in the yield calculation, the Gilmore approach was applied as described in the section 5.2. In Fig. 5.11, 5.12, 5.13 and 5.14 the ROIs used for the areas determination are shown for the case of proton energy of 348 keV, in the center of mass. In Fig. 5.15, 5.16, 5.17 and 5.18 the ROIs used for the areas determination are shown at center of mass energy 375 keV. The transition energy is indicated with a green vertical line, while the peak region with two red lines. The background ROIs are denoted with the vertical dark-blue lines.

For the transition by the deexcitation from the first excited state of ^{17}F, the peak area was determined by fitting the peak shape of both 495.33 keV (deexcitation) peak and 511 keV (annihilation) peak together.

The peak area of the 495.33 keV γ-ray peaks has been measured considering a Gaussian from the deexcitatoin plus an exponential tail. The function used the peak area measurement is a peak with low-energy tailing: $G(E) + T(E)$ Tail = exponential background $\otimes$ Gaussian shape (detector widening) as here below

$$\mathrm{T(E)} = \int_{-\infty}^{\mathrm{E_0}} \mathrm{A} \cdot \mathrm{T} \cdot \exp(\tau \cdot \mathrm{E}) \cdot \exp\left[\frac{-(\mathrm{E}-\mathrm{E_0})^2}{2\sigma^2}\right] \cdot \mathrm{dE}$$

$$\mathrm{T(E)} = \mathrm{A} \cdot \frac{\mathrm{T}}{2} \cdot \exp\left[(\mathrm{E}-\mathrm{E_0})\,\tau + \frac{\sigma^2\tau^2}{2}\right] \cdot \mathrm{erfc}\left[\frac{1}{\sqrt{2}}\left(\frac{(\mathrm{E}-\mathrm{E_0})}{\sigma} + \sigma\tau\right)\right]$$

$$\mathrm{erf(x)} = \frac{2}{\sqrt{\pi}} \int_{\mathrm{x}}^{\infty} \mathrm{e}^{-\mathrm{t}^2} \mathrm{dt}$$

Once the net counts were determined the yield was calculated.

As cross check the yield obtained from the analysis of different run at same energy were compared and a good agreement was found, see Fig. 5.27 for the transitions at 370 keV beam energy, and Fig. 5.28 for the transitions at 398 keV beam energy.

The angular distribution, $W_\gamma(\theta, E)$, can be described by a sum of Legendre polynomials $P_k(\theta)$:

$$W_y(\theta, E) = \Sigma_k a_k(E) P_k(\theta) \quad (k = 0, 1, 2, \ldots) \tag{5.12}$$

where $a_k(E)$ are the energy-dependent coefficients. The resulting angular distribution for the ^{16}O(p,γ)^{17}F reaction, fitting the experimental yield with Equation 5.12 at the first order, see Fig. 5.23, 5.24, 5.25, 5.26 and Tab. 5.6, 5.7.

run name	**transition**	a_1
run171	$DC \rightarrow 1st$	-0.0906 ± 0.011
	$DC \rightarrow ground$	-0.0009 ± 0.004
run221	$DC \rightarrow 1st$	-0.0718 ± 0.014
	$DC \rightarrow ground$	-0.0056 ± 0.010

Table 5.6: Fitting parameters for the Angular Distribution of the ^{16}O(p,γ)^{17}F reaction measured at 370 keV beam energy in lab frame

run name	**transition**	a_1
run233	$DC \rightarrow ground$	-0.0011 ± 0.006
run277	$DC \rightarrow ground$	-0.0086 ± 0.005

Table 5.7: Fitting parameters for the Angular Distribution of the ^{16}O(p,γ)^{17}F reaction measured at 398 keV beam energy in lab frame

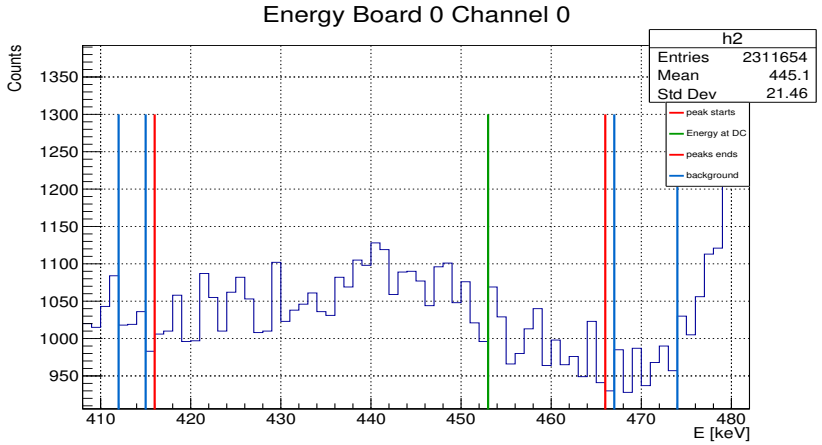

(a) γ-ray spectrum recorded in the $CeBr_3$ detector at 0°

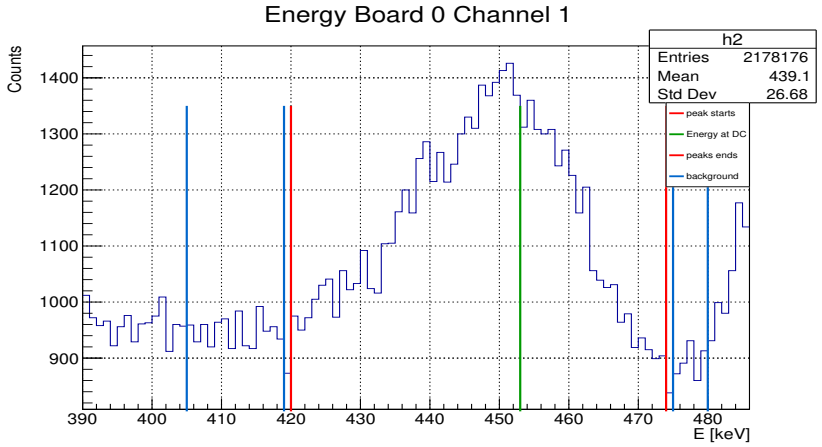

(b) γ-ray spectrum recorded in the $CeBr_3$ detector at 90°

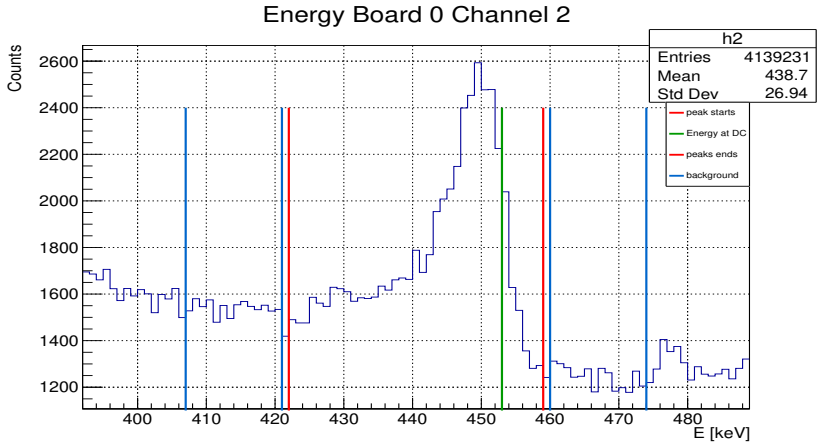

(c) γ-ray spectrum recorded in the HPGe detector at 55°

Figure 5.11. Peak for *DC → 1st excited state* of ^{17}F at beam energy 370 keV in lab frame (run171). The energy range indicated in red correspond to the area where the γ-ray following the decay of Direct Capture to the 1st excited states in ^{17}F is located. The energy range in blue corresponds to range used to correct for the background contribution in the peak area analysis.

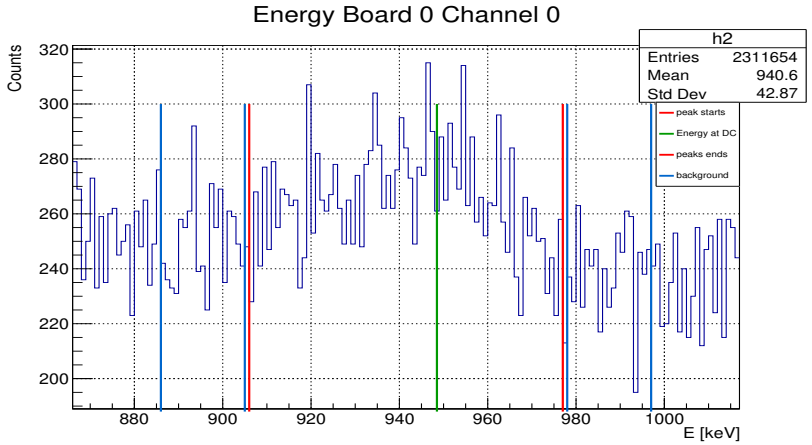

(a) γ-ray spectrum recorded in the $CeBr_3$ detector at 0°

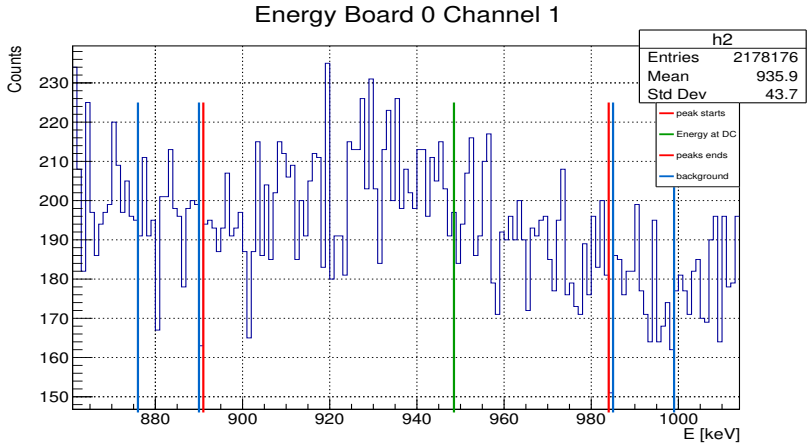

(b) γ-ray spectrum recorded in the $CeBr_3$ detector at 90°

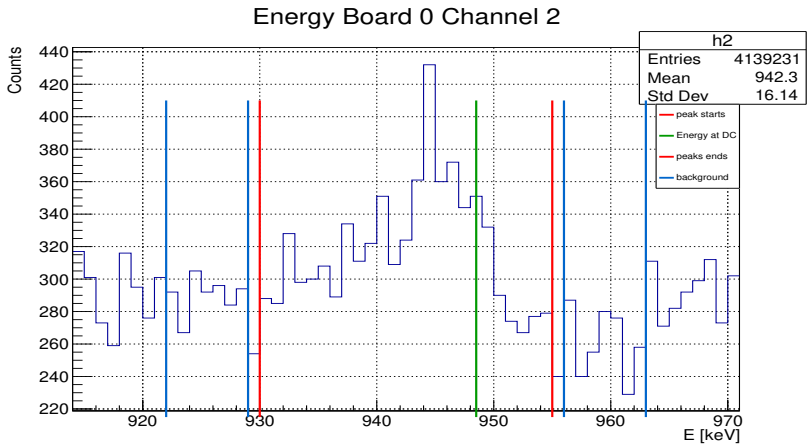

(c) γ-ray spectrum recorded in the HPGe detector at 55°

Figure 5.12. Peak for $DC \rightarrow$ *ground state* of ^{17}F at beam energy 370 keV in lab frame (run171). The energy range indicated in red correspond to the area where the γ-ray following the decay of Direct Capture to the ground states in ^{17}F is located. The energy range in blue corresponds to range used to correct for the background contribution in the peak area analysis.

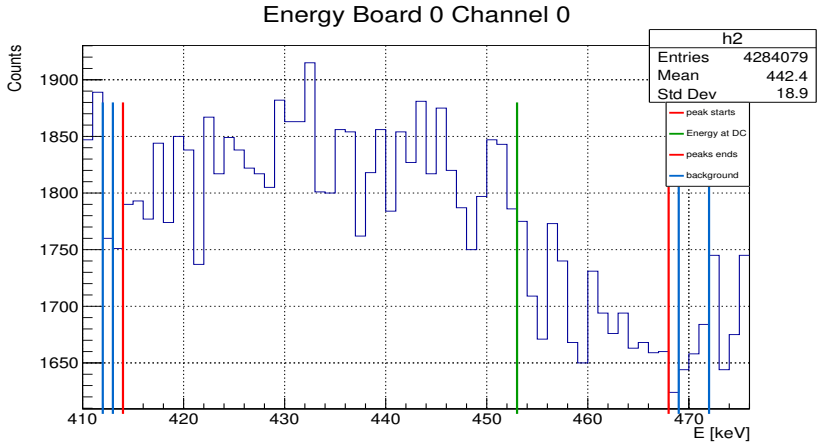

(a) γ-ray spectrum recorded in the $CeBr_3$ detector at 0°

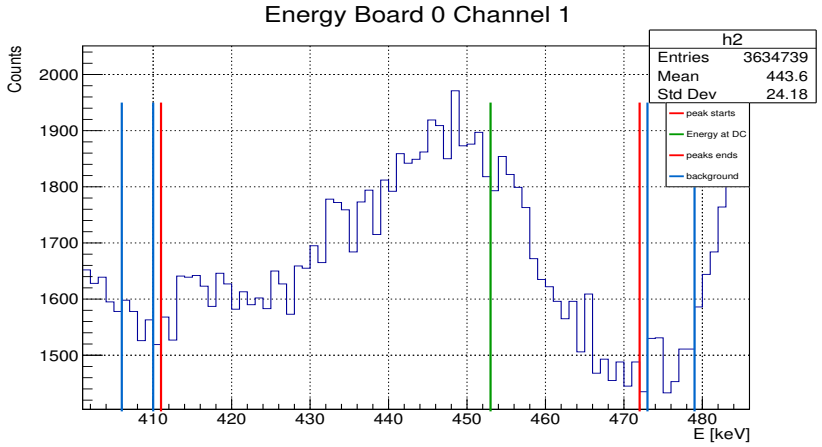

(b) γ-ray spectrum recorded in the $CeBr_3$ detector at 90°

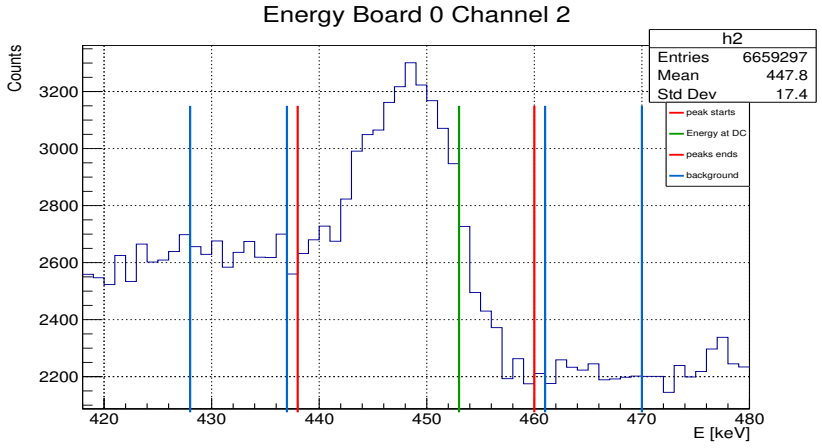

(c) γ-ray spectrum recorded in the HPGe detector at 55°

Figure 5.13. Peak for *DC → 1st excited state* of ^{17}F at beam energy 370 keV in lab frame (run221). The energy range indicated in red correspond to the area where the γ-ray following the decay of Direct Capture to the 1st excited states in ^{17}F is located. The energy range in blue corresponds to range used to correct for the background contribution in the peak area analysis.

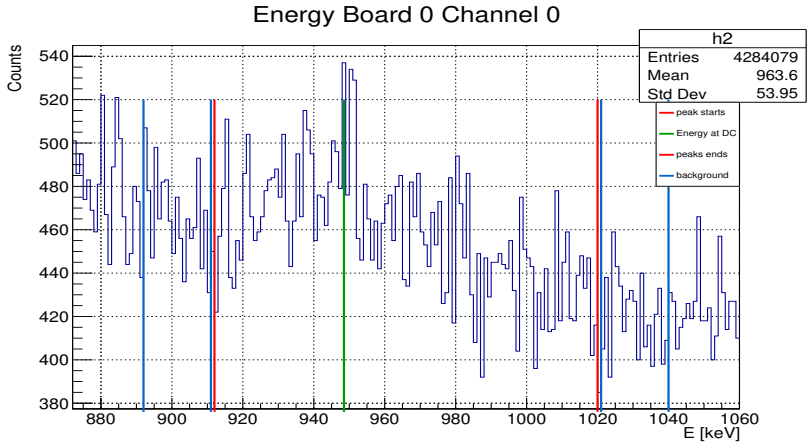

(a)

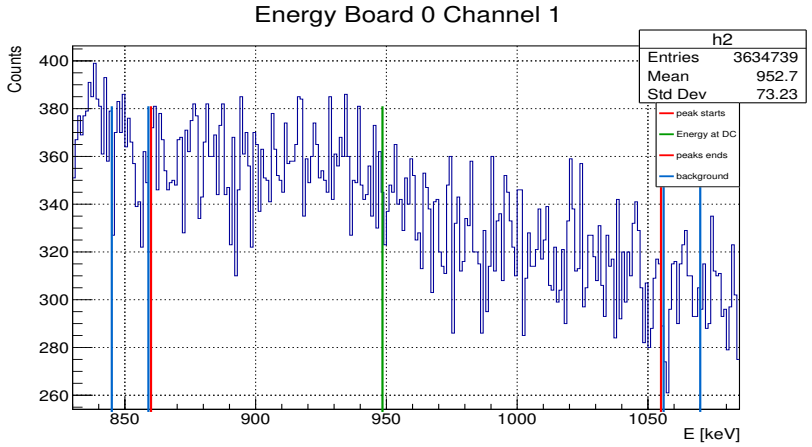

(b)

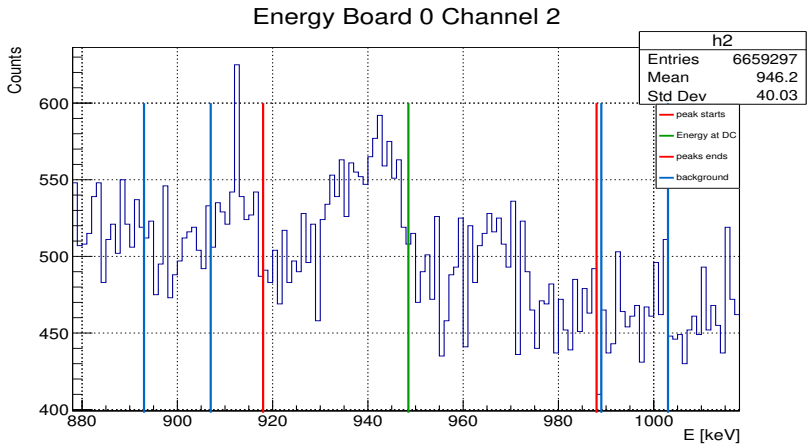

(c)

Figure 5.14. Peak for *DC* $\rightarrow$ *ground state* of ^{17}F at beam energy 370 keV in lab frame (run221). The energy range indicated in red correspond to the area where the γ-ray following the decay of Direct Capture to the ground in ^{17}F is located. The energy range in blue corresponds to range used to correct for the background contribution in the peak area analysis.

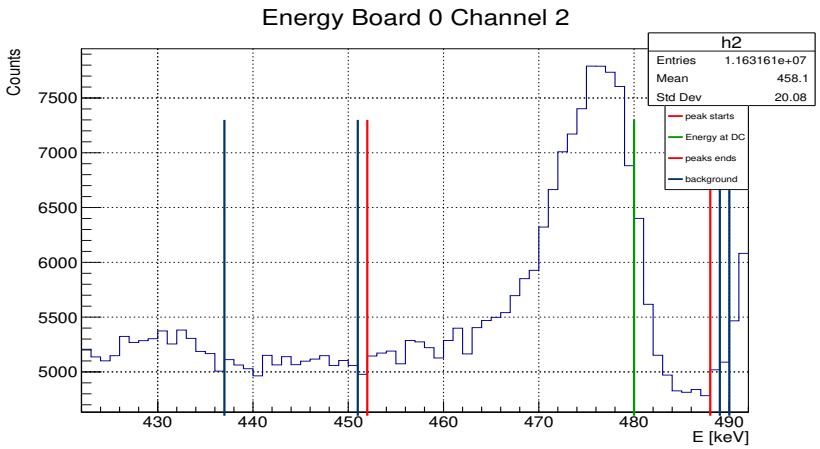

Figure 5.15. Peak for *DC → 1st excited state* of ^{17}F at beam energy 398 keV in lab frame (run233). The energy range indicated in red correspond to the area where the γ-ray following the decay of Direct Capture to the 1st excited states in ^{17}F is located. The energy range in blue corresponds to range used to correct for the background contribution in the peak area analysis. Only the Spectrum from the HPGe detector is shown.

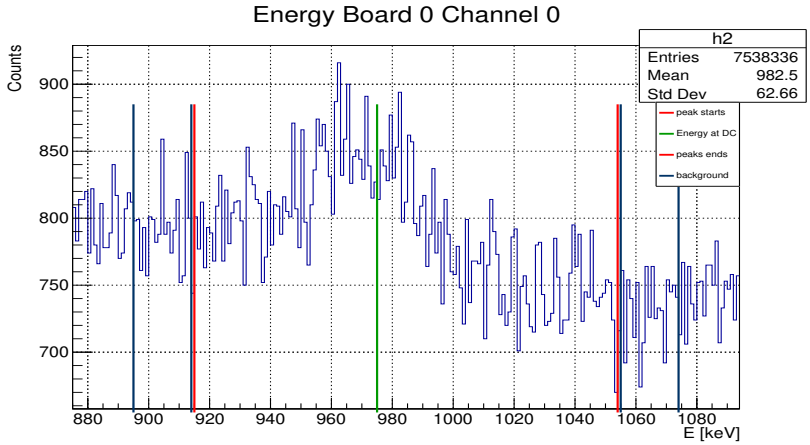

(a) γ-ray spectrum recorded in the $CeBr_3$ detector at 0°

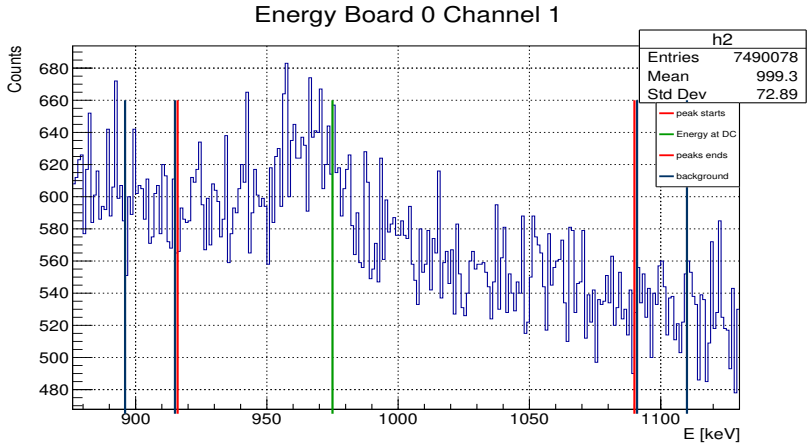

(b) γ-ray spectrum recorded in the $CeBr_3$ detector at 90°

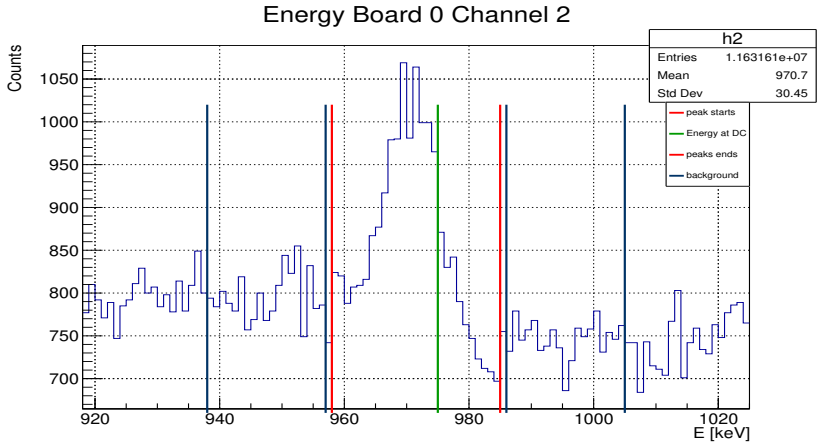

(c) γ-ray spectrum recorded in the HPGe detector at 55°

Figure 5.16. Peak for $DC \rightarrow$ *ground state* of ^{17}F at beam energy 398 keV in lab frame (run233). The energy range indicated in red correspond to the area where the γ-ray following the decay of Direct Capture to the ground states in ^{17}F is located. The energy range in blue corresponds to range used to correct for the background contribution in the peak area analysis.

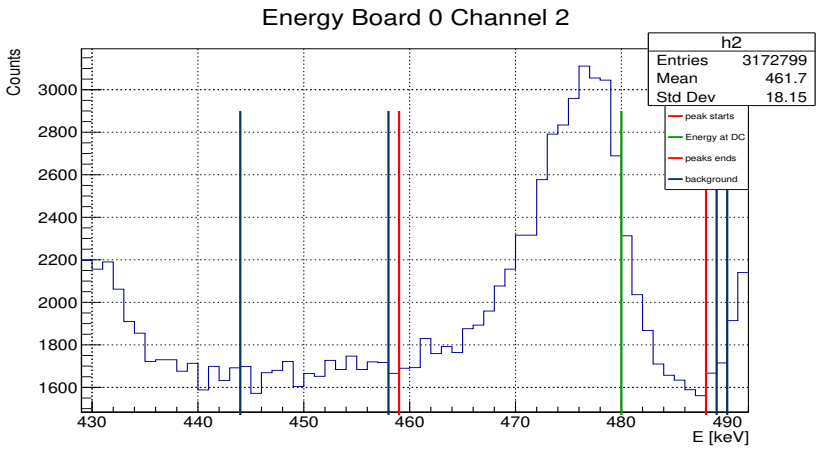

Figure 5.17. Peak for *DC → 1st excited state* of ^{17}F at beam energy 398 keV in lab frame (run277). The energy range indicated in red correspond to the area where the γ-ray following the decay of Direct Capture to the first excited states in ^{17}F is located. The energy range in blue corresponds to range used to correct for the background contribution in the peak area analysis. Only the spectrum from the HPGe detector is shown.

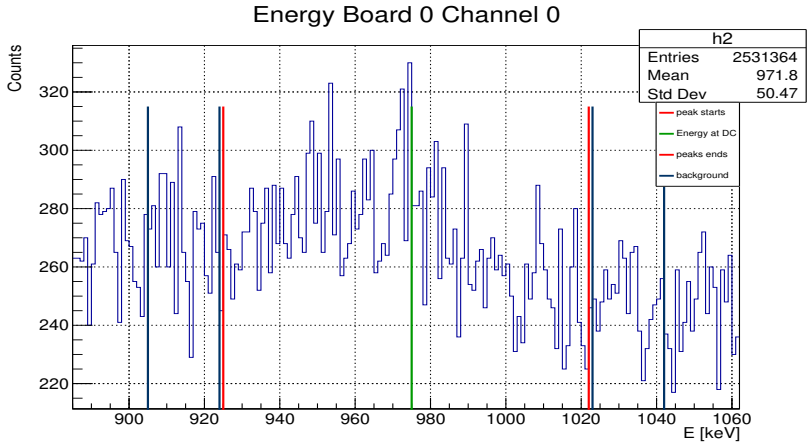

(a) γ-ray spectrum recorded in the $CeBr_3$ detector at 0°

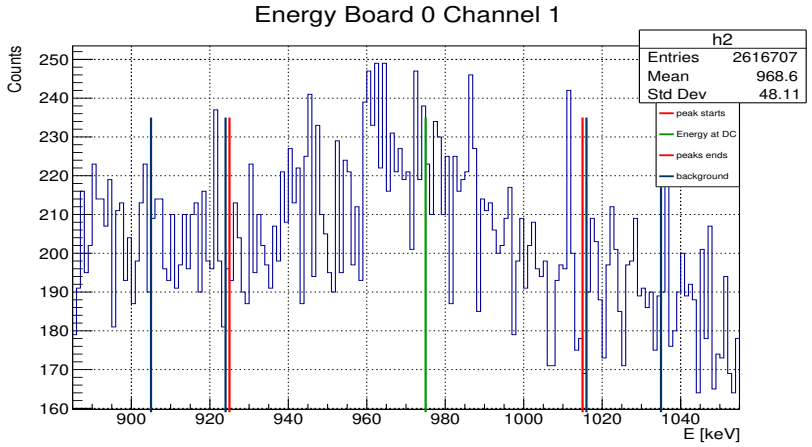

(b) γ-ray spectrum recorded in the $CeBr_3$ detector at 90°

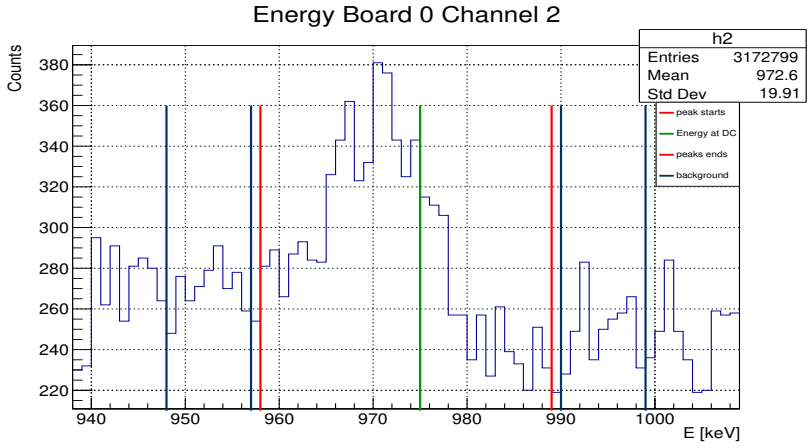

(c) γ-ray spectrum recorded in the HPGe detector at 55°

Figure 5.18. Peak for $DC \rightarrow$ *ground state* of ^{17}F at beam energy 398 keV in lab frame (run277). The energy range indicated in red correspond to the area where the γ-ray following the decay of Direct Capture to the ground states in ^{17}F is located. The energy range in blue corresponds to range used to correct for the background contribution in the peak area analysis.

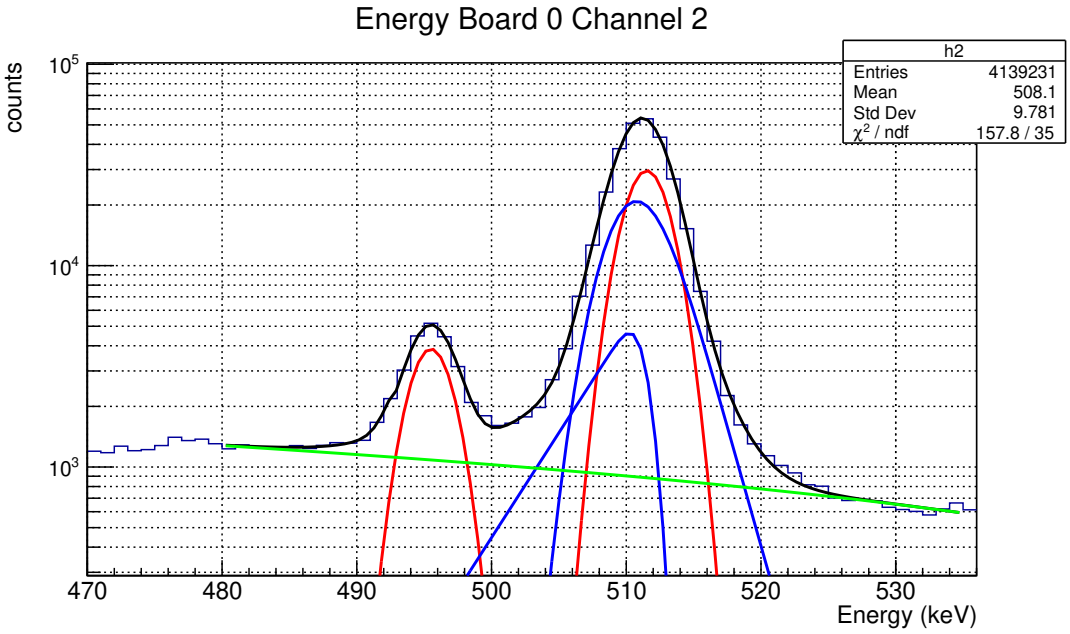

Figure 5.19. Peak from *first excited state* → *ground state* of ^{17}F, recorded in the HPGe detector at 55°, at beam energy 370 keV in lab frame (run171).

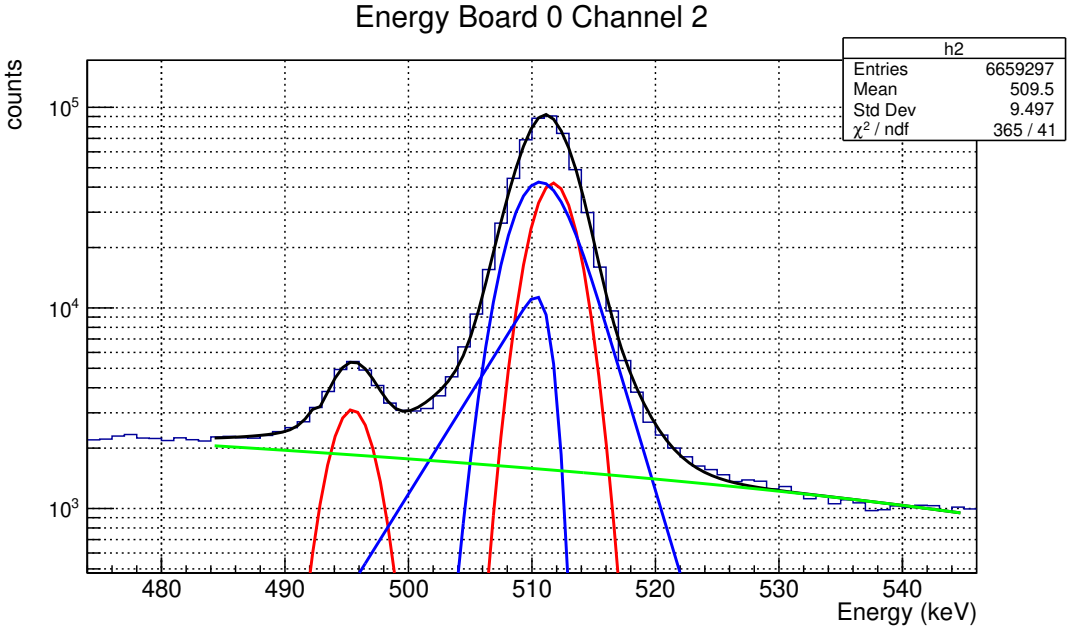

Figure 5.20. Peak from *first excited state* → *ground state* of ^{17}F, recorded in the HPGe detector at 55°, at beam energy 370 keV in lab frame (run221).

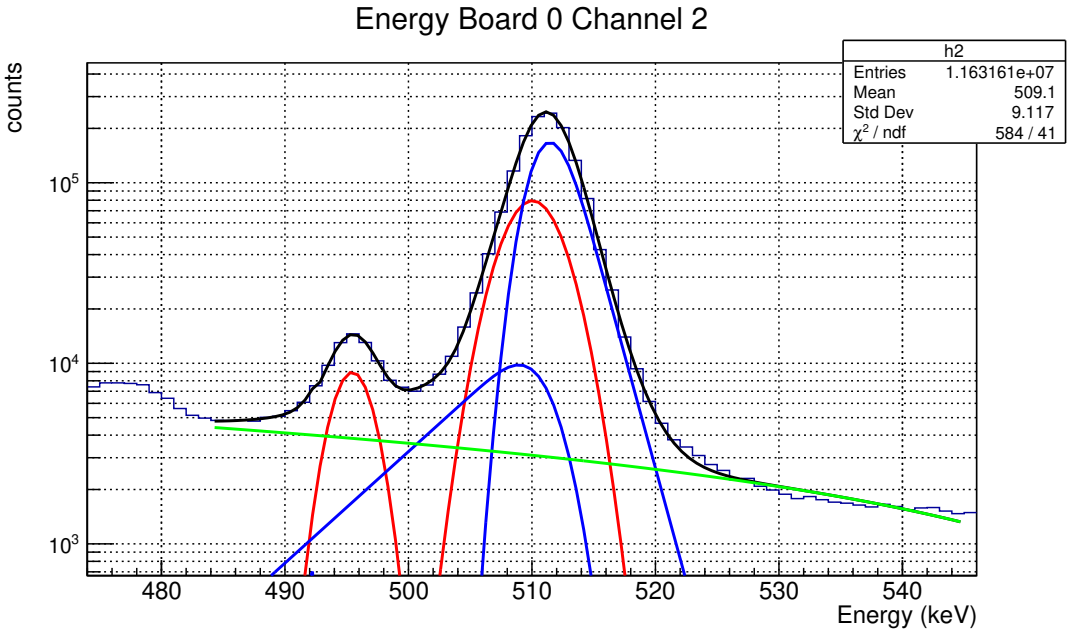

Figure 5.21. Peak from *first excited state* → *ground state* of ^{17}F, recorded in the HPGe detector at 55°, at beam energy 398 keV in lab frame (run233).

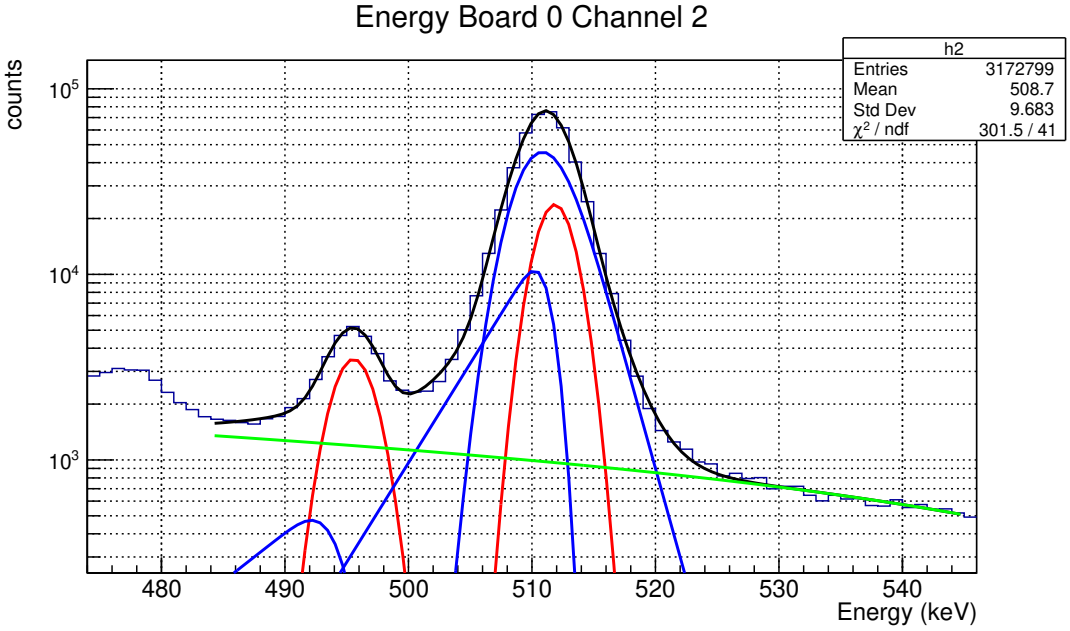

Figure 5.22. Peak from *first excited state* → *ground state* of ^{17}F, recorded in the HPGe detector at 55°, at beam energy 398 keV in lab frame (run277).

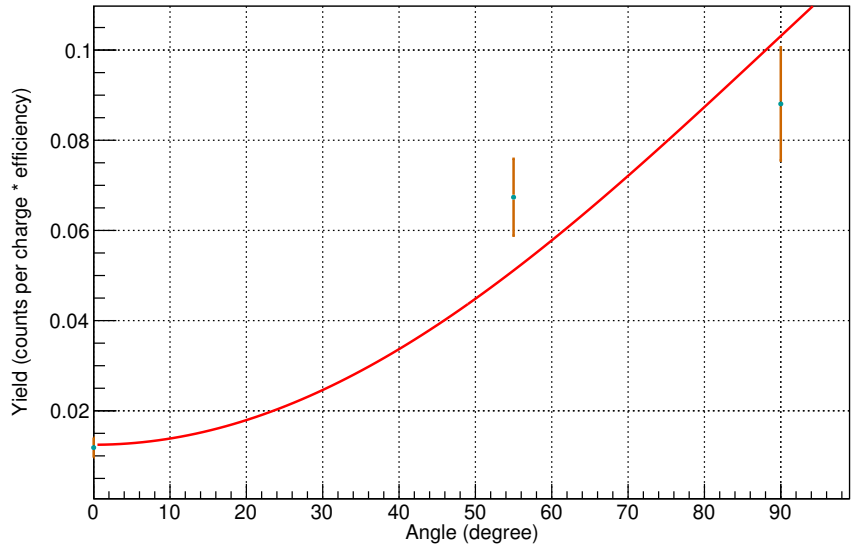

(a) Angular Distribution curve for $DC \rightarrow$ *first excited state* of ^{17}F at beam energy 370 keV in lab frame

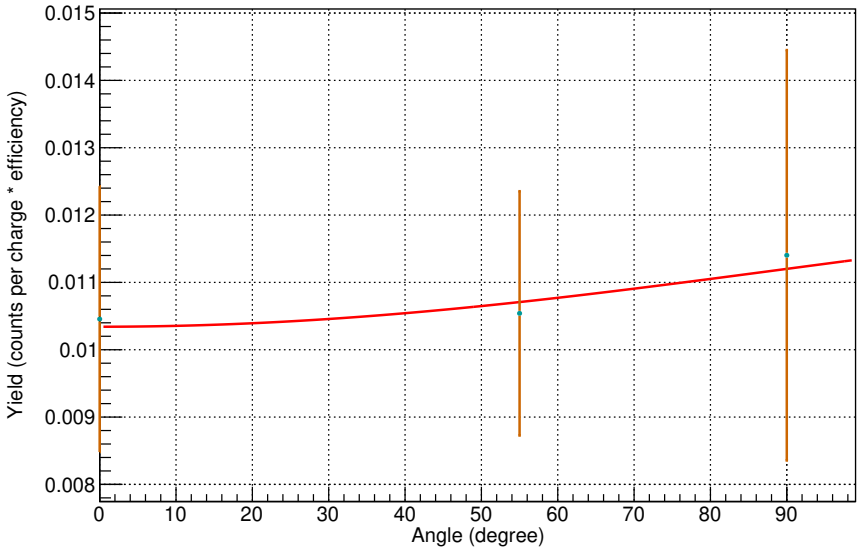

(b) Angular Distribution curve for $DC \rightarrow$ *ground state* of ^{17}F at beam energy 370 keV in lab frame

Figure 5.23. Angular Distribution curve for the ^{16}O(p,γ)^{17}F reaction at beam energy 370 keV in lab frame (from run171)

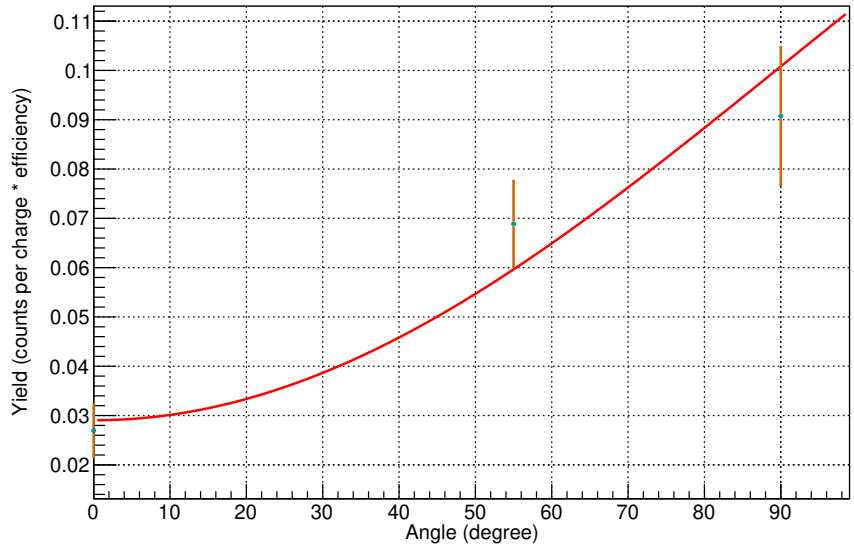

(a) Angular Distribution curve for $DC \rightarrow$ *first excited state* of ^{17}F at beam energy 370 keV in lab frame

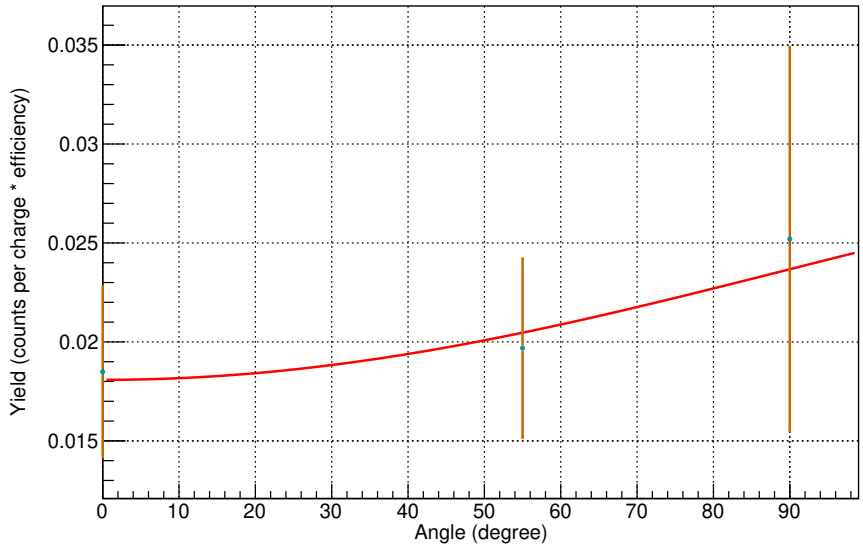

(b) Angular Distribution curve for $DC \rightarrow$ *ground state* of ^{17}F at beam energy 370 keV in lab frame

Figure 5.24. Angular Distribution curve for the ^{16}O(p,γ)^{17}F reaction at beam energy 370 keV in lab frame (from run221)

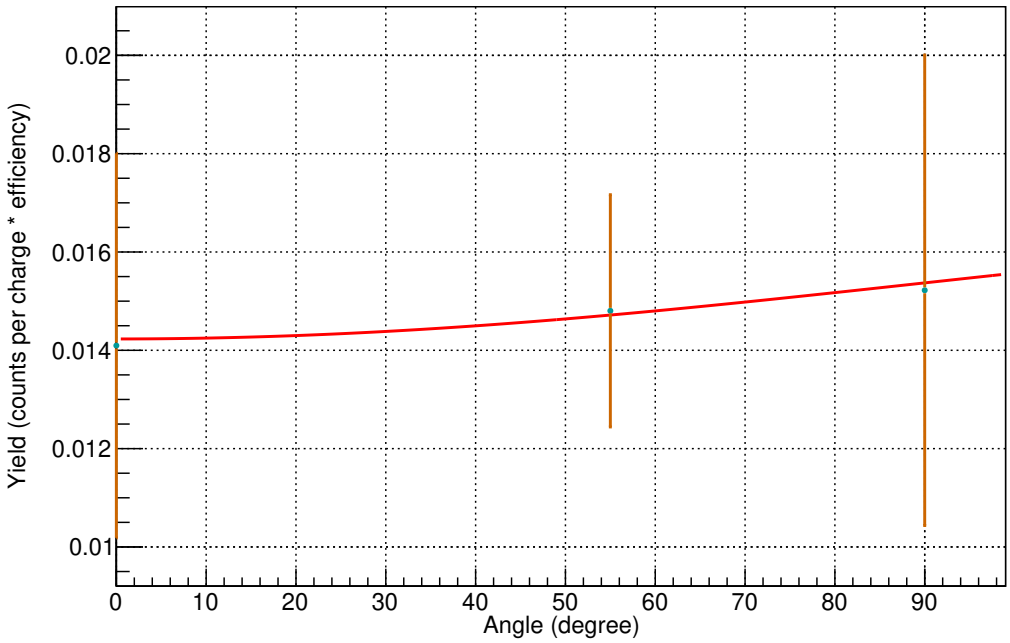

Figure 5.25. Angular Distribution curve for $DC \rightarrow$ *ground state* of ^{17}F at beam energy 398 keV in lab frame (from run233)

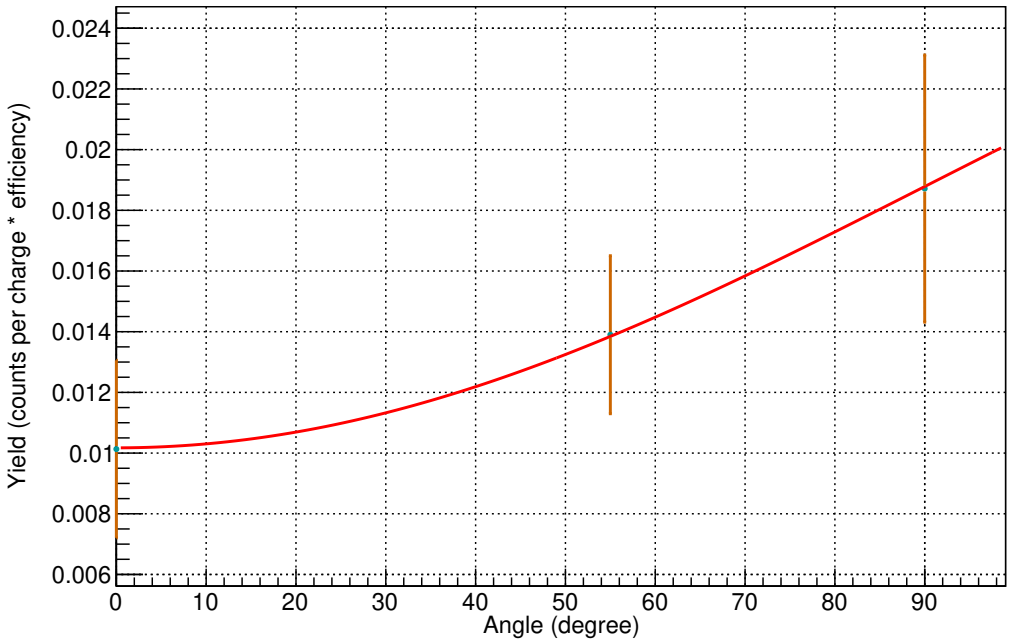

Figure 5.26. Angular Distribution curve for $DC \rightarrow$ *ground state* of ^{17}F at beam energy 398 keV in lab frame (from run277)

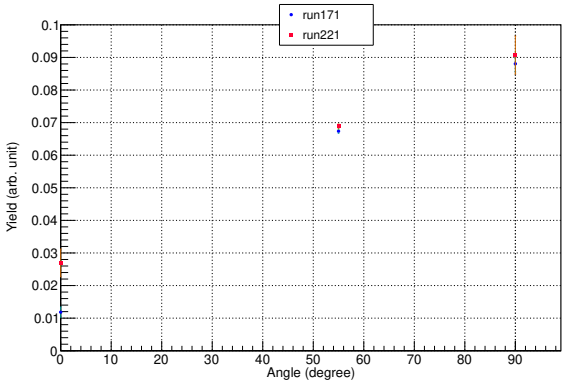

(a) Angular Distribution curve for $DC \rightarrow$ *first excited state* of ^{17}F at beam energy 370 keV in lab frame

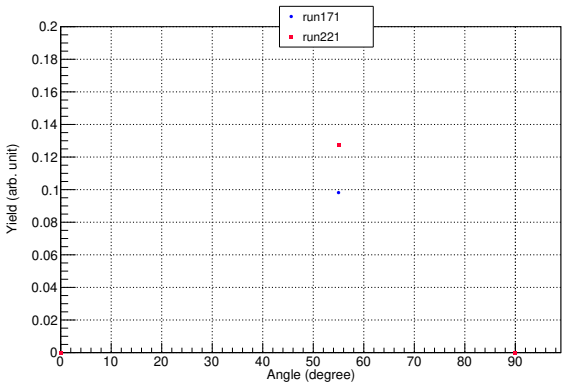

(b) Angular Distribution curve for *1st excited state* $\rightarrow$ *ground state* of ^{17}F at beam energy 370 keV in lab frame

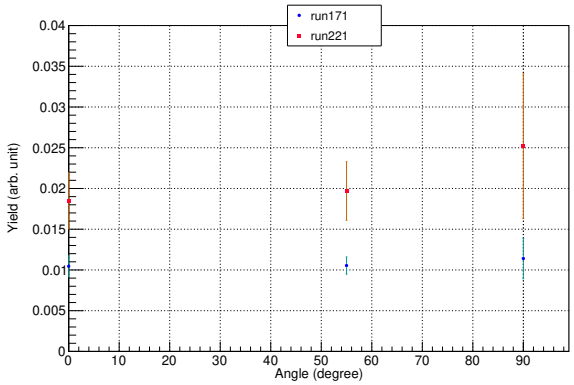

(c) Angular Distribution curve for $DC \rightarrow$ *ground state* of ^{17}F at beam energy 370 keV in lab frame

Figure 5.27. Angular Distribution curve for the ^{16}O(p,γ)^{17}F reaction at beam energy 370 keV in lab frame

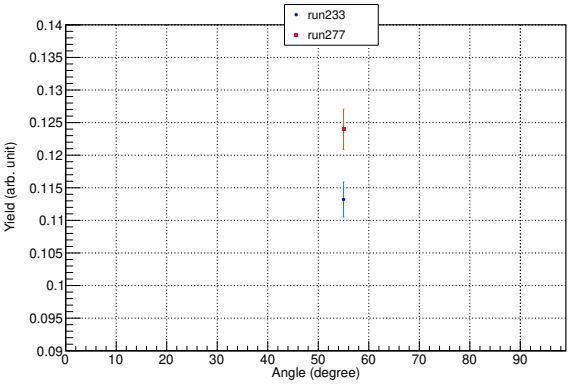

(a) Angular Distribution curve for *DC* → *first excited state* of ^{17}F at beam energy 398 keV in lab frame

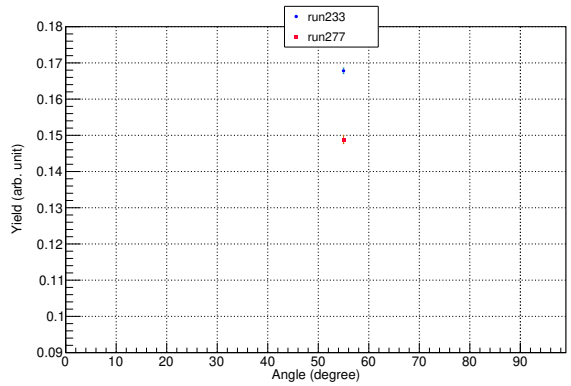

(b) Angular Distribution curve for *1st excited state* → *ground state* of ^{17}F at beam energy 398 keV in lab frame

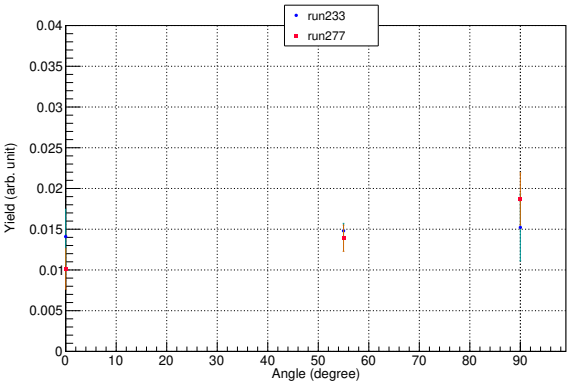

(c) Angular Distribution curve for *DC* → *ground state* of ^{17}F at beam energy 398 keV in lab frame

Figure 5.28. Angular Distribution curve for the ^{16}O(p,γ)^{17}F reaction at beam energy 398 keV in lab frame

6 Conclusion

The $^{16}O(p,\gamma)^{17}F$ reaction is a key reaction of the CNO cycle, playing a crucial role in determining the $^{16}O/^{17}O$ abundance ratio in RGB and AGB stars. This ratio is a useful tool to trace mixing processes in RGB and AGB stars as well as the Galactic Chemical Evolution. Despite its importance the $^{16}O(p,\gamma)^{17}F$ reaction cross section is poorly constrained. In particular a missing piece of information is the angular distribution, crucial parameter for the cross section determination.

In present work a recent measurement of the $^{16}O(p,\gamma)^{17}F$ reaction angular distribution performed at LUNA was described. The experimental setup consisted of three detectors, an HPGe and two $CeBr_3$, located at three different angles around the Ta_2O_5 solid targets. The low count rate limited the measurement to two beam energies. The yield for the three transitions expected from the $^{16}O(p,\gamma)^{17}F$ reaction was obtained and fitted with a proper function describing the angular distribution. Results are provided.

The present work represents a preliminary analysis and future work is foreseen to complete the angular distribution determination and also cross section calculation.

In particular, new GEANT4 simulations are expected from the simulation group of LUNA to provide necessary correction for taking into account summing correction that could affect the efficiency. The target will be characterised with ancillary experiments in order to provide the parameters for the evaluation of the final correction. The data of the present thesis show that and angular distribution effect should be taken into account for all transitions. This is a confirmation of the Rolfs et al. [Rol73] results but with a less pronounced structure with respect to the higher energies explored in their paper.

References

[A.16] Best A. *The European Physical Journal A*, 52:72, 2016.

[ABDG22] Marialuisa Aliotta, Axel Boeltzig, Rosanna Depalo, and György Gyürky. Exploring stars in underground laboratories: Challenges and solutions. *Annual Review of Nuclear and Particle Science*, 72(1):177–204, 2022.

[Axe18] Boeltzig Axel. Improved background suppression for radiative capture reactions at luna with hpge and bgo detectors. *Journal of Physics G: Nuclear and Particle Physics*, 45:025203, 2018.

[Axn22] Marvin Axness. Study of the reaction ^{16}o(p,γ)^{17}f at luna, Sep. 2022.

[BBFH57] E. Margaret Burbidge, G. R. Burbidge, William A. Fowler, and F. Hoyle. Synthesis of the Elements in Stars. *Reviews of Modern Physics*, 29(4):547–650, January 1957.

[BNC23] Berkeley Nucleonics Corporation BNC. Cerium bromide: Cebr3 high resolution / low background scintillators, 2023.

[Bru16] C. G. Bruno. Improved direct measurement of the 64.5 kev resonance strength in the ^{17}o(p,α)^{14}n reaction at luna. *Phys. Rev. Lett.*, 117:142502, Sept. 2016.

[Bru19] C. G. Bruno. Improved astrophysical rate for the ^{18}o(p,α)^{15}n reaction by underground measurements. *Physics Letters B*, 790:237–242, Mar. 2019.

[Bun16a] Physikalisch-Technische Bundesanstalt. ^{137}cs calibration certificate, 2016.

[Bun16b] Physikalisch-Technische Bundesanstalt. ^{60}co calibration certificate, 2016.

[Cac12] Antonio Caciolli. Preparation and characterisation of isotopically enriched Ta_2O_5 targets for nuclear astrophysics studies. *European Physical Journal A*, 48:144, Oct. 2012.

[Cen14] NASA Goddard Space Flight Center. Star life cycles, Nov. 2014.

[CG29] E. U. Condon and R. W. Gurney. *Phys. Rev.*, 33:127, 1929.

[CGH75] H. C. Chow, G. M. Griffiths, and T. H. Hall. The $^{16}O(p,\gamma)^{17}F$ Direct Capture Cross Section with an Extrapolation to Astrophysical Energies. *Canadian Journal of Physics*, 53.17:1672–1686, 1975.

[Coc23] Cococubed.com. Burn hydrogen, 2023. Last accessed 29 October 2023.

[COS] The SAO Encyclopedia of Astronomy COSMOS. Stellar evolution.

[Dep19] Rosanna Depalo. Nuclear astrophysics deep underground and the luna experiment. *Journal of Physics: Conference Series*, 1308(1):012009, aug 2019.

[EB07] J. K. Tuli E. Browne. ^{137}cs decay radiation information, 2007.

[EB13] J. K. Tuli E. Browne. ^{60}co decay radiation information, 2013.

[Fer65] A. J. Ferguson. Angular correlation methods in gamma-ray spectroscopy. *North-Holland, Amsterdam*, 1965.

[FIJ+03] A. Formicola, G. Imbriani, M. Junker, D. Bemmerer, R. Bonetti, C. Broggini, C. Casella, P. Corvisiero, H. Costantini, G. Gervino, C. Gustavino, A. Lemut, P. Prati, V. Roca, C. Rolfs, M. Romano, D. Schürmann, F. Strieder, F. Terrasi, H.-P. Trautvetter, and S. Zavatarelli. The LUNA II 400kV accelerator. *Nuclear Instruments and Methods in Physics Research Section A: Accelerators, Spectrometers, Detectors and Associated Equipment*, 507(3):609–616, 2003.

[Gam28] Z. Gamow, G. *Phys. Rev.*, 51:204, 1928.

[Gil08] Gordon R. Gilmore. *Practical Gamma-Ray Spectrometry*. John Wiley and Sons, Ltd, 2008.

[Gmb13] Deutsche Akkreditierungsstelle GmbH. ^{133}ba calibration certificate, 2013.

[HPL58] R. E. Hester, R. E. Pixley, and W. A. Lamb. Radiative Capture of Protons in Oxygen at 140 to 170 kev. *Physical Review*, 111.6:1604–1606, Sept. 1958.

[Ili08] C. Iliadis. New reaction rate for $^{16}O(p,\gamma)^{17}F$ and its influence on the oxygen isotopic ratios in massive AGB stars. *Physical Review C*, 77.4:045802, Apr. 2008.

[Ili15] C. Iliadis. *Nuclear Physics of Stars*. Physics textbook. Wiley, 2015.

[LSH+15] Lebzelter, T., Straniero, O., Hinkle, K. H., Nowotny, W., and Aringer, B. Oxygen isotopic ratios in intermediate-mass red giants. *A&A*, 578:A33, 2015.

[LUN10] Collaboration LUNA. *The European Physical Journal A*, 44:513–519, 2010.

[Mer52] Paul W Merrill. Spectroscopic observations of stars of class s. *The Astrophysical Journal*, 116:21, 1952.

[MI12] P. Mohr and C. Iliadis. Recommended cross-section of the ^{16}O(p,γ)^{17}F reaction below 2.5 MeV: A potential tool for quantitative analysis and depth profiling of oxygen. *Nuclear Instruments and Methods in Physics Research A*, 688:62–65, Oct. 2012.

[Mor97] R. Morlock. Halo Properties of the First $1/2^+$ State in ^{17}F from the ^{16}O(p,γ)^{17}F reaction. *Physical Review Letters*, 79.20:3837–3840, Nov. 1997.

[NG68] A. Notea and Y. Gurfinkel. Transitions in ^{133}Cs from the decay of ^{133}Ba. , 107(1):193–208, January 1968.

[Obs17] Chandra Xray Observatory. Stellar evolution - cycles of formation and destruction introduction to the h-r diagram, Apr. 2017.

[ORT02] ORTEC. Gem series hpge (high-purity germanium) coaxial detector system, Oct. 2002.

[Phi74] Dawson Phillips. Preparation of free-standing films of anodic tantalum oxide. *Nuclear Instruments and Methods*, 116(1), 3 1974.

[RB67] H. J. Rose and D. M. Brink. *Rev. Mod. Phys.*, 39:306, 1967.

[Rol73] C. Rolfs. Spectroscopic factors from radiative capture reactions. *Nuclear Physics A*, 217.1:29–70, Dec. 1973.

[ROO23] ROOT. Root: analyzing petabytes of data, scientifically., 2023.

[RR88] C.E. Rolfs and W.S. Rodney. *Cauldrons in the Cosmos: Nuclear Astrophysics*. Theoretical Astrophysics. University of Chicago Press, 1988.

[SBK+87] S. Seuthe, H.W. Becker, A. Krauss, A. Redder, C. Rolfs, U. Schröder, H.P. Trautvetter, K. Wolke, S. Wüstenbecker, R.W. Kavanagh, and

F.B. Waanders. Production and properties of implanted targets. *Nuclear Instruments and Methods in Physics Research Section A: Accelerators, Spectrometers, Detectors and Associated Equipment*, 260(1):33–42, 1987.

[SU56] H. E. Suess and H. C. Urey. *Revs. Modern Phys.*, 28:53, 1956.

[Tan59] Neil Tanner. Direct Radiative Capture of Protons by O^{16} and Ne^{20}. *Physical Review*, 114.4:1060–1064, May 1959.